PHOTONIC CRYSTAL TEXTILES

A Thesis Submitted to
the Graduate School of Engineering and Sciences of
İzmir Institute of Technology
in Partial Fulfillment of the Requirements for the Degree of

DOCTOR OF PHILOSOPHY

in Physics

by
Zebih ÇETİN

July 2022
İZMİR

Dedicated to the ones I love the most, my family

ACKNOWLEDGMENTS

I would like to thank my supervisor, Assoc. Prof. Dr. H. Sami SÖZÜER, for his support and guidance. I also thank to my friends at department of physics for their friendship. I would like to express my sincere thanks to my family.

The numerical calculations reported in this thesis were fully performed at TUBITAK ULAKBIM, High Performance and Grid Computing Center (TRUBA resources).

ABSTRACT

PHOTONIC CRYSTAL TEXTILES

Photonic crystals are man-made structures that can be used to manipulate the flow of light. They are classified as one-, two- and three-dimensional photonic crystals according to the periodic variation of the dielectric profile in space. Apart from artificial photonic crystals there are numerous examples of naturally occurring photonic crystals which have evolved mostly for structural coloration, such as wings of butterflies, natural opal gem stone, peacock feathers to name a few. Using photonic crystal structures the propagation of electromagnetic waves can entirely be prohibited by means of photonic band gap. Considering the fact that approximately two thirds of the heat loss of the human body occurs through electromagnetic radiation with a wavelength around 10 microns, it becomes important to consider photonic crystals for the purpose of reducing heat loss in textiles. We observe that the textile, by virtue of the fact that it has been produced by weaving, already has a periodic structure, and thus is a potential candidate for a photonic crystal. With the right fiber that the textile is woven and the right weave pattern, the textile itself would be a photonic crystal. The most common weave patterns used in the textile industry are plain weave, basket weave, dutch weave and twill weave. In this thesis, we used the finite-difference time-domain method to search for the optimum weave pattern to minimize heat loss by the human body.

ÖZET

FOTONİK KRİSTAL TEKSTİLLER

Fotonik kristaller, elektromanyetik dalgaları (ışığı) manipüle etmek için kullanılabilen insan yapımı yapılardır. Uzayda dielektrik profilin periyodik değişimine göre bir, iki ve üç boyutlu fotonik kristaller olarak sınıflandırılırlar. Yapay fotonik kristallerin yanı sıra, kelebek kanadı, doğal opal değerli taşlar, tavus kuşu tüyü gibi çoğunlukla yapısal renklenme için evrimleşmiş doğal olarak oluşan fotonik kristallerin sayısız örneği vardır. Fotonik kristal yapılar kullanılarak elektromanyetik dalgaların yayılması fotonik bant aralığı vasıtasıyla tamamen engellenebilir. İnsan vücudundaki ısı kaybının yaklaşık üçte ikisinin dalga boyu 10 mikron civarında olan elektromanyetik radyasyon yoluyla gerçekleştiği göz önüne alındığında, tekstillerde ısı kaybını azaltmak amacıyla fotonik kristallerin dikkate alınması önem kazanmaktadır. Dokuma yoluyla üretilmiş olması nedeniyle kumas zaten periyodik bir yapıya sahiptir ve bu nedenle potansiyel bir fotonik kristaldir. Eğer kumaşın imal edildiği iplik gerekli elektriksel, optik ve geometrik özelliklere sahipse, kumaşın kendisi bir fotonik kristal gibi davranacaktır. Tekstil sektöründe en çok kullanılan örgü modelleri düz örgü, sepet örgü, hollanda örgü ve dimi örgüdür. Bu tezde, insan vücudunun ısı kaybını azaltmak için en uygun örgü modelini sonlu farklar (FDTD) yöntemini kullanrak arastırdık.

TABLE OF CONTENTS

LIST OF FIGURES vii

LIST OF TABLES xiv

CHAPTER 1. INTRODUCTION 1

CHAPTER 2. THEORY AND COMPUTATIONAL METHODS 6

2.1. Maxwell's Equations 6

2.1.1. Plane Wave Expansion Method 8

2.1.2. Finite-Difference Time-Domain Method 14

2.1.3. Blackbody Radiation 17

CHAPTER 3. PHOTONIC CRYSTAL TEXTILES 21

3.1. One-Dimensional Photonic Crystals (Distributed Bragg Reflector) 23

3.2. Woodpile Photonic Crystals 31

3.3. Three-Dimensional Woven Photonic Crystals 41

3.3.1. Plain Weave 43

3.3.2. Basket Weave 53

3.3.3. Twill Weave 61

3.3.4. Dutch Weave 69

CHAPTER 4. CONCLUSION AND FUTURE WORK 86

4.1. Conclusion 86

4.2. Future Work 87

REFERENCES 89

LIST OF FIGURES

Figure		Page
Figure 2.1	Spectral radiance as a function of wavelength of an ideal blackbody for five different temperature, $T = 300K$, $T = 500K$, $T = 1000K$, $T = 1500K$, and $T = 5777K$.	18
Figure 2.2	Spectral radiance as a function of wavelength of an ideal blackbody at temperature $T = 310$K.	19
Figure 2.3	Spectral radiance as a function of frequency of an ideal blackbody at temperature $T = 310$K.	20
Figure 3.1	(a) One-dimensional, (b) two-dimensional (Joannopoulos et al., 2008), and (c) three- dimensional (Lin et al., 1998), (Vlasov et al., 2001) (Johnson and Joannopoulos, 2000) photonic crystals examples.	21
Figure 3.2	One-dimensional multi-layer structure, or one-dimensional photonic crystal. (a) 3D view. (b) 2D view.	23
Figure 3.3	One-dimensional multi-layer structure, or one-dimensional photonic crystal. (a) One unit cell. (b) Three unit cell. (c) Five unit cell.	25
Figure 3.4	Transmission (green curves) and reflection (red curves) spectrum for single-layer, three- and five-layers, with thickness of $d_a = 0.30a$ and dielectric constant $\epsilon_a = 5.38$ immersed in air background, $\epsilon_b = 1.0$.	26
Figure 3.5	FDTD Simulation setup of a single homogeneous plate immersed in air background for transmission calculation.	27
Figure 3.6	FDTD simulation setup of a single (a), three (b), and five (c) unit cells of a homogeneous plate immersed in air for transmission calculation.	28
Figure 3.7	Left colum: Transmission spectrum for single layer, three, and five layers (solid red curves are for analytical solutions and solid blue curves are for numerical solutions). Right column: Blackbody radiation spectrum (dashed red curves) and transmission values multiplied by blackbody radiation (solid blue curves).	29
Figure 3.8	Woodpile photonic crystal structure. (a) 3D view, (b) top view and (c) side view.	31

Figure **Page**

Figure 3.9 FDTD simulation setup for single unit cell of woodpile photonic crystal structure. (a) 3D view. (b)-(c) 2D view. 32

Figure 3.10 Transmission spectrum (top graph), blackbody radiation curve (bottom red curve) and the transmission spectrum multiplied by blackbody radiation curve(bottom green curve). 33

Figure 3.11 Transmission spectrum for single unit cell of woodpile structure (red curve), transmission spectrum of homogeneous plate (blue curve). Blackbody radiation spectrum (green curve) and transmission values multiplied by blackbody radiation (purple and orange curves). 34

Figure 3.12 The FDTD simulation setup of bare woodpile structure with three unit cell along stacking direction ($z-$direction). (a) 3D view. (b) 2D view from $x-z$ plane. (c) 2D view from $y-z$ plane. 35

Figure 3.13 Transmission spectrum for connected woodpile structure (blue curve). Blackbody radiation spectrum (red curve) and transmission values multiplied by blackbody radiation (green curve) 36

Figure 3.14 The FDTD simulation setup of connected woodpile structure with three unit cell along stacking direction ($z-$direction). (a) 3D view. (b) 2D view from $x-z$ plane. (c) 2D view from $y-z$ plane. 37

Figure 3.15 Transmission spectrum for connected woodpile structure (blue curve). Blackbody radiation spectrum (red curve) and transmission values multiplied by blackbody radiation (green curve) 38

Figure 3.16 Transmission spectrum for connected woodpile structure (blue curve). Blackbody radiation spectrum (red curve) and transmission values multiplied by blackbody radiation (green curve). 39

Figure 3.17 Transmitted power versus yarn radius for bare and connected woodpile structure. 40

Figure 3.18 The most common weave patterns. (a) Plain Weve. (b) Basket Weave. (c) Dutch Weave. (d) Twill weave. 41

Figure 3.19 Modified weave patterns. Modified plain weave, Modified basket weave. Modified twill weave and two variation for Dutch Weave (Modified dutch weave-I and Modified dutch weave-II). 42

Figure **Page**

Figure 3.20 Plain weave structure, 3D view (a), top view (b) and side view (c). FDTD simulation setup, single unit cell (d), three unit cells (e), and five unit cells (f) in $z-$direction. 43

Figure 3.21 Transmission spectrum of plain weave pattern for 1-unit cell, 3-, and 5-unit cells (left column). Blackbody radiation spectrum (red dashed curve on the right column) and blackbody spectrum multiplied by transmission values of plane weave pattern (blue curve on the right column). 45

Figure 3.22 Transmission spectrum of plain weave structure for single-, three-, and five-unit cell (left column). Blackbody radiation spectrum (red dashed curve on the right column) and blackbody spectrum multiplied by transmission values of plane weave pattern (blue curve on the right column). 46

Figure 3.23 Transmitted power percentage versus yarn radius for single unit cell (left graph), three unit cell (middle graph) and five unit cells (right graph). 47

Figure 3.24 (a). 3D view, (b) Top view, (c). Side view of modified plane weave pattern. Simulation setup for modified plane weave pattern. (d). Single unit cell. (e). Three unit cells. (f). Five unit cells. 48

Figure 3.25 Transmission values (blue curve on the left column) and the blackbody radiation (red dashed curve on the right column) multiplied by transmission values of plane weave pattern (blue curve on the right column) for single unit cell, three and five unit cells. 50

Figure 3.26 Transmission spectrum (blue curve on the left column) and the blackbody radiation (red dashed curve on the right column) multiplied by transmission values (blue curve on the right column) of modified plain weave pattern for single unit cell, three and five unit cells. 51

Figure 3.27 Transmitted power percentage versus yarn radius for single unit cell (left graph), three unit cell (middle graph) and five unit cells (right graph). 52

Figure **Page**

Figure 3.28 Structure of basket weave pattern: (a) 3D view, (b) Top view and (c) Side view. FDTD simulation setup of basket weave pattern for single (d), three (e) and five layers (f). 53

Figure 3.29 The transmission spectrum for the basket weave pattern for single unit cell, three, and five unit cells with dielectric constant of $\epsilon_a = 5.38$ and radius of yarns $r = 0.05a$. (left column). Blackbody radiation spectrum (red dashed curves) and the transmission spectrum of the structure (blue curves on the right column). 55

Figure 3.30 The transmission spectrum for the basket weave pattern for single unit cell, three, and five unit cells with dielectric constant of $\epsilon_a = 5.38$ and radius of yarns $r = 0.06a$. (left column). Blackbody radiation spectrum (red dashed curves) and the transmission spectrum of the structure (blue curves on the right column). 56

Figure 3.31 Structure of modified basket weave pattern. (a) 3D view, (b) Top view and (c) side view. Simulation setup for basket weave pattern for one unit cell (d), three unit cell (e) and five unit cell (f) in $z-$direction. 57

Figure 3.32 The transmission spectrum for modified basket weave with radius $r = 0.05a$(left column). Blackbody radiation spectrum (red dashed curve on the right column), and transmission values multiplied bu blackbody radiation spectrum (blue curve on the right column) 59

Figure 3.33 The transmission spectrum for modified basket weave with radius $r = 0.06a$ (left column). Blackbody radiation spectrum (red dashed curve on the right column), and transmission values multiplied bu blackbody radiation spectrum (blue curve on the right column) 60

Figure 3.34 Structure of twill weave pattern. (a) 3D view, (b) Top view and (c) Side view. Simulationsetup for twill weave pattern: (d) Single unit cell, (e) Three unit cells and (f) Five unit cells along $z-$direction. 61

Figure 3.35 The transmission values for twill weave pattern. Single unit cell, three and five unit cell (left column). Blackbody radiation spectrum (red dashed curves on the right column) and transmission values multiplied by blackbody radiation (blue curves on the right column). 63

Figure **Page**

Figure 3.36 The transmission values for twill weave pattern. Single unit cell, three and five unit cell (left column). Blackbody radiation spectrum (red dashed curves) and transmission values multiplied by blackbody radiation (blue curves on the right column). 64

Figure 3.37 Structure of modified twill weave pattern. (a.) 3D view, (b.) Top view and (c.) Side view. Simulation setup: (d) Single unit cell, (e) Three and (f) Five unit cells. 65

Figure 3.38 The transmission spectrum for modified twill weave pattern with radius of $r = 0.05a$ (blue curves on the left column). Blackbody radiation (red dashed) and transmission spectrum multiplied by blackbody spectrum for single unit cell, three and five unit cells. 67

Figure 3.39 The transmission spectrum for the modified twill weave pattern (blue curves on the left column) for a single unit cell, three and five unit cells. Blackbody radiation (red dashed curves on the right column) and transmission spectrum multiplied by blackbody radiation (blue curves on the right column). 68

Figure 3.40 Structure of dutch weave pattern. (a) 3D view, (b) Top view and (c) Side view. Simulation setup for single unit cell (d), three (e) and five (f) unit cells. 69

Figure 3.41 Left column: Transmission spectrum for single unit cell, three and five unit cell. Right column: Blackbody radiation spectrum (dashed red curve). Transmission spectrum of the dutch weave pattern multiplied by blackbody radiation (blue curve). 71

Figure 3.42 Left column: Transmission spectrum for single unit cell, three and five unit cell. Right column: Blackbody radiation spectrum (dashed red curve). Transmission spectrum of the dutch weave pattern multiplied by blackbody radiation (blue curve). 72

Figure 3.43 Transmitted power percentage versus yarn radius for the dutch weave. Single (left graph) unit cell, three (middle graph) unit cells and five (right graph) unit cells. 73

Figure **Page**

Figure 3.44 The structure of the modified dutch weave-I pattern. (a) 3D view, (b) Top view and (c) Side view. Simulation setup of the modified dutch weave-I pattern for single unit cell (d), three (e) and five (f) unit cells. . 74

Figure 3.45 Transmission spectrum for single, three and five unit cell for modified dutch weave (left column). Blackbody radiation spectrum (right column red dashed curve). Transmission values multiplied by blackbody radiation spectrum (blue curve on the right column). 76

Figure 3.46 Transmission spectrum for single, three and five unit cell for modified dutch weave (left column). Blackbody radiation spectrum (right column red dashed curve). Transmission values multiplied by blackbody radiation spectrum (blue curve on the right column). 77

Figure 3.47 Transmitted power percentage versus yarn radius for the dutch weave-I. Single (left graph) unit cell, three (middle graph) unit cells and five (right graph) unit cells. 78

Figure 3.48 3D view (a), top view (b) and side view (c) of modified dutch weave-II pattern. Simulation setup for modified dutch weave-II pattern for single (d), three (e) and five (f) unit cell. 79

Figure 3.49 The transmission spectrum of the modified dutch weave-II for one, three, and five unit cells (left column). Blackbody radiation spectrum (red dashed curves) and transmission spectrum of the structure multiplied by blackbody radiation for one unit cell, three, and five unit cells (blue curves on the right column). 81

Figure 3.50 The transmission spectrum of the modified dutch weave pattern for one unit cell, three, and five unit cells (left column). Blackbody radiation spectrum (red dashed curve) and transmission spectrum of the structure multiplied by blackbody radiation for one unit cell, three, and five unit cells (blue curves on the right column). 82

Figure **Page**

Figure 3.51 The transmission spectrum of modified dutch weave-II for one unit cell, three, and five unit cells (left column). Blackbody radiation spectrum (red dashed curve) and the transmission spectrum of the structure multiplied by blackbody radiation for one unit cell, three, and five unit cells (blue curves on the right column). 83

Figure 3.52 Transmitted power percentage versus yarn radius for the modified dutch weave-II. Single (left graph) unit cell, three (middle graph) unit cells, and five (right graph) unit cells. 84

Figure 3.53 Percentage of transmitted power versus yarn radius for five different weave patterns. Plain weave, modified plain weave, dutch weave, modified dutch weave-I, and modified dutch weave-II for single unit cell (left graph), three unit cells (middle graph), and five unit cells (right graph). 85

LIST OF TABLES

Table **Page**

Table 3.1 Transmitted power for woodpile photonic crystal with changing yarn radius. 40
Table 3.2 Transmitted power percentage for plain weave pattern. 47
Table 3.3 Percentage of transmitted power for modified plain weave. 52
Table 3.4 Percentage of transmitted power for dutch weave. 73
Table 3.5 Percentage of transmitted power for modified dutch weave-I. 78
Table 3.6 Percentage of transmitted power for modified dutch weave-II. 84

CHAPTER 1

INTRODUCTION

Heat loss of the human body basically occurs in 3 different ways, convection and conduction, evaporation of moisture, and radiation (Hardy et al. (1934a), Hardy et al. (1934b), Hardy et al. (1934c), Hardy et al. (1934), Winslow et al. (1939)). Depending on the environmental conditions such as wind, ambient temperature, relative humidity in the air and the person's clothing, which of these 3 different channels has a share in the heat loss varies. For example, convection becomes the most important heat loss channel in windy weather. Or for someone lying on cold snow, heat loss by physical contact may be more important. However, under normal conditions, about two-thirds of the heat loss from the human body is through radiation (Hardy and DuBois, 1937).

The intensity of the electromagnetic waves emitted by an ideal blackbody at temperature T, depending on the frequency, that is, the energy emitted from the unit area of the blackbody in unit time, in unit frequency range, is given by the Planck distribution (Planck, 2013), $u(\nu, T) = (8\pi h/c^3)\nu^3/(e^{h\nu/kT} - 1)$. where h is Planck's constant, c is the speed of light, k is Boltzmann's constant, and ν is the frequency. Integrating over the frequency and multiplying by the area of the object gives the energy emitted from the object per unit time, $P_{emitted} = \varepsilon A\sigma T^4$, where A is the surface area of the object, σ is the Stephan-Boltzmann constant, and ε (emissivity) is a measure of how close the object's surface is to the ideal blackbody surface. If $\varepsilon = 1$, the surface emits radiation (and absorbs the radiation falling on it) like an ideal blackbody. For human skin, this value has been measured as approximately $\epsilon = 0.98$ (Hardy et al., 1934; Sanchez-Marin et al., 2009; Steketee, 1973). In other words, the human skin radiates energy almost like an ideal blackbody. Every blackbody emits energy itself, as well as absorbs the energy emitted by the objects around it. If we take the ambient temperature as T_0, the energy taken from the environment is $P_{absorbed} = \varepsilon A\sigma T_0^4$. Since the energy given and received is from the same surface, the net loss of energy per unit time from the human body to the surroundings by radiation is $P_{net} = P_{emitted} - P_{absorbed} = \varepsilon A\sigma(T^4 - T_0^4)$. As the difference between the ambient temperature and the temperature of the human body increases, the heat loss by

radiation also increases rapidly. Suppressing this radiation can reduce the energy loss by radiation thereby reducing the demand on energy for heating space around human body to maintain thermal comfort. It has been shown that using a one-dimensional photonic crystal one can reduce electromagnetic radiation (blackbody radiation) (Cornelius and Dowling, 1999).

Photonic crystals (PCs) are artificially formed structures by periodically alternating arrangement of high and low dielectric constant materials (John, 1987; Yablonovitch, 1987; Yablonovitch and Gmitter, 1989). When the waves reflect from this periodic structure, depending on the geometry of the periodic structure and the wavelength, waves scattered from different points of the structure causes interference, and depending on whether this interference is damping or strengthening gives rise to the formation of a photonic band gap (PBG). Electromagnetic waves with frequencies falling into this gap are forbidden to propagate in the crystal. While the principle is so simple, the complexity of the geometry of the structure makes it difficult to determine, without any prior calculations, exactly what a given wave will do. While rough estimates are possible for some specific cases, in general it is nearly impossible to predict the result with reasonable accuracy without doing some fairly intensive numerical calculations. Many calculations made in the late 1980s, when the interest in PCs first emerged, contained serious errors in this regard (Sözüer et al., 1992).

Using the vector nature of electromagnetic fields, photonic band structure of dielectric spheres arranged in face-centered-cubic (fcc) lattice symmetry is calculated for the first time (Ho et al., 1990). Another three-dimensional structure that possesses a complete PBG is a called "Yablonovite" and can be fabricated by chemical-beam-assisted ion etching (Yablonovitch et al., 1991). The first three-dimensional photonic crystal with a complete band gap, dubbed "woodpile," is studied theoretically (Sözüer and Dowling, 1994; Ho et al., 1994) and fabricated using a "layer-by-layer" technique and experimentally studied in the microwave and far-infrared frequency regime (Özbay et al., 1994; Özbay, 1996). Microwave transmittance values and band structures of a 4 unit cell thick photonic crystal formed from periodically stacked alumina rods were calculated (Özbay et al., 1994). Even with only 4 unit cell thickness, the transmittance for frequencies in the photonic band gap decreased by -40 to -70 dB. In another pioneering study, the transmittance measurements of the fcc tetragonal photonic crystal, which consists of four period-

ically stacked layers, at frequencies between microwave and far infrared were examined (Özbay, 1996), and it was observed that the transmittance of the photonic crystal with a 4 unit cell thickness decreased to around -50 dB in the band gap. These results, especially the demonstration by Özbay that the microwave transmittance of a photonic crystal even with a thickness of only 4 unit cells can be reduced so much, gives us hope that photonic crystal thermal fabrics can be implemented practically.

Three-dimensional PC structures mentioned above were hard to fabricate, and the fabrication methods were time consuming and expensive while the gaps obtained were in the microwave regime. For the human body at a temperature of $37°C$ $(310K)$, the wavelength at which the radiation emitted has a maximum intensity around $10\mu m$, with a very wide distribution and it is in the infrared regime of electromagnetic spectrum. So it is desirable to find an easy fabrication method for large scale production with a fairly low cost.

Photonic band gap properties of dielectric fibers woven into a three-dimensional structure, similar to the weaving patterns used in textiles, that can behave as photonic crystals is calculated (Tsai et al., 1998). To obtain a wide band gap, the dielectric constants of the fibers immersed in air background need to be 40 (or greater). In a similar study, it is reported that an absolute photonic band gap can be achieved with fairly lower dielectric constant ($\epsilon \sim 16$) (Tsai et al., 1999). Topologically similar to previous two works, large and robust photonic band gaps were achieved using square spiral posts in a tetragonal lattice (Toader and John, 2001; L. Chern et al., 2004).

Using textile technology, a straight woodpile like fabric, a multilayered woven fabric, and three-dimensional woven fabric was fabricated. It was shown that those structure posses photonic band gaps in the 6 to 15 GHz range (Watanabe et al., 2004). But those structures are rigid and not suitable to change shape. Fibers formed from alumina balls into teflon tube in a certain period as in photonic crystals (Watanabe et al., 2010) was fabricated. It was shown that flexible woven photonic crystals can be fabricated. Besides flexibility, high dielectric contrast is also required for the formation of a photonic band gap. It was shown that cotton-yarn coated by TiO_2 can have high dielectric contrast (Furukawa et al., 2012). For high temperature applications, the use of photonic crystal structures to control the electromagnetic wave propagation of objects at temperatures around 1000°C (and above) (Shklover et al., 2009) is proposed. However, since the

wavelength will be 3 microns and below at these temperatures, the required fibers must be much finer.

Regulating thermal energy in close vicinity of the human body without any input power like traditional heating and cooling systems has attracted great interest in the scientific community. For cooling it is required that materials used to make clothes need to be infrared-transparent visible-opaque to have a cooling effect. It was shown that synthetic polymer fibers (Tong et al., 2015), nanoporous polyethylene (nanoPE (Hsu et al., 2016; Cai et al., 2019), boron nitride composite fibers (a-BN/PVA) (Gao et al., 2017), nanofiber membrane (NFM) (Xiao et al., 2019), microstructures with randomly stacked silk fibers (Yang and Zhang, 2021) and nanoporous polymer matrix composites (PMCs) (Zhou et al., 2021) are permeable to human body radiation in the mid-infrared spectrum but opaque to visible light. In another work it was shown that using photonic crystals properties, woven, knitted or nonwoven textiles (Catrysse et al., 2016; Chen et al., 2021) or polyethylene oxide films composed of random nanofibres as daytime radiative coolers (Li et al., 2021) can be used to make effective cooling wearable clothes. It was shown that a high reflectance in the sunlight region because of its ordered or disordered photonic structure a selective emittance in the mid-infrared region can be achieved. A tri-layered structure (nylon (PA), polyvinylidene fluoride (PVDF) and polyethylene (PE)) (Song et al., 2020) and a hybrid membrane exfoliated BN nanosheets (BNNS) with layered double hydroxide (LDH) nanosheets covering the surface of the inorganic-organic hybrid cellulose membrane (ICM) (Gu et al., 2021) was studied for personal thermal management.

For heating purposes, a personal thermal management system based on metallic nanowire-embedded fabric (Hsu et al., 2015), a fabricated MXene/nanoPE textile with a low IR emissivity at 7-14 μm (Shi et al., 2021) were proposed to reflect human body thermal radiation. Besides thermal insulation, these fabrics can be supplied by power to have additional active heating functionality. Using nanoporous metallized polyethylene (Cai et al., 2017), silk fibroin/graphene oxide aerogel fibers (SF/GO) (Wang et al., 2020), fibers composed of a polyurethane (PU)-ATO composite (Jeong et al., 2020) and carbon nanotubes (CNTs) (Yu et al., 2021) it was shown that the created nanophotonic structure textiles with tailored infrared (IR) properties can be used for passive personal heating. In another study, CNT/cellulose aerogel layers, cotton textiles, and copper nanowire (CuNW)-based conductive network (CNN) layers were used to create a laminated fabric

with improved photothermal conversion, mid-infrared reflectance, thermal insulation, and electrical heating performance (Guo et al., 2021).

Building energy efficiency and personal thermal management have both benefited from the development of dual-mode thermal management materials capable of both cooling and heating. For example a bilayer emitter inserted inside an infrared-transparent nanoporous polyethylene (nanoPE) layer in the dual-mode textile can be used to perform both radiative cooling and heating (Hsu et al., 2017). By using engineered fabric building blocks, a metafabric was created and analyzed for applications such as personal thermal cooling, thermal insulation, and thermoregualation (Jafar-Zanjani et al., 2017). Inspired from nature, a composite material inspired by squid skin's dynamic color-changing capability with tunable thermoregulatory capabilities was designed (Leung et al., 2019). A polymer photonic membrane (Assaf et al., 2020), nanostructured material (Luo et al., 2021) that captures solar energy and a dual-mode thermal management materials using just organic polymers (Xiang et al., 2022) are studied in order to thermoregulate the human body microclimate.

However, solutions proposed so far involve production of photonic crystals and somehow embedding them into or fixing them onto textiles. We observe that the textiles, by virtue of the fact that they have been produced by weaving, already have a periodic structure, and thus are potential candidates for a photonic crystal. Thus it's not necessary to manufacture a separate photonic crystal and somehow "mount" it on the textile. If the fiber that the textile is woven from has the necessary electrical, optical and geometrical properties (Tao et al., 2018), and is woven with the right geometrical structure, then the textile itself would be a thin layer of photonic crystal.

CHAPTER 2

THEORY AND COMPUTATIONAL METHODS

2.1. Maxwell's Equations

To understand propagation of light in dielectric medium we start with microscopic Maxwell's equations,

$$\begin{aligned} \nabla \cdot \mathbf{E} &= \rho/\epsilon_o \\ \nabla \cdot \mathbf{B} &= 0 \\ \nabla \times \mathbf{B} &= \mu_0 \mathbf{J} + \epsilon_o \frac{\partial \mathbf{E}}{\partial t} \\ \nabla \times \mathbf{E} &= -\frac{\partial \mathbf{B}}{\partial t} \end{aligned} \tag{2.1}$$

where ρ and $\mathbf{J}$ represent charge density and current density, and ϵ_0 and μ_0 are the permittivity and the permeability of free space, respectively. In a material medium $\mathbf{D}$ and $\mathbf{H}$ are defined as $\mathbf{D} \equiv \epsilon_0 \mathbf{E} + \mathbf{P}$ and $\mathbf{H} \equiv \frac{1}{\mu_0}\mathbf{B} - \mathbf{M}$, where $\mathbf{P}$ is the electric polarization of the medium and $\mathbf{M}$ is the magnetization of the medium. Using these definitions, Maxwell's equations for macroscopic fields take the form

$$\begin{aligned} \nabla \cdot \mathbf{D} &= \rho_f \\ \nabla \cdot \mathbf{B} &= 0 \\ \nabla \times \mathbf{H} &= \mathbf{J}_f + \frac{\partial \mathbf{D}}{\partial t} \\ \nabla \times \mathbf{E} &= -\frac{\partial \mathbf{B}}{\partial t} \end{aligned} \tag{2.2}$$

which are called Maxwell's equation for macroscopic fields and ρ_f and $\mathbf{J}_f$ are the free charge and current densities respectively. In a medium with no free charges and current,

$\rho_f = 0$, $\mathbf{J}_f = 0$, Maxwell's equations become

$$\begin{aligned} \nabla \cdot \mathbf{D} &= 0, \qquad \nabla \times \mathbf{H} = \frac{\partial \mathbf{D}}{\partial t} \\ \nabla \cdot \mathbf{B} &= 0, \qquad \nabla \times \mathbf{E} = -\frac{\partial \mathbf{B}}{\partial t} \end{aligned} \tag{2.3}$$

For isotropic, non-dispersive and non-lossy materials $\mathbf{D}$ and $\mathbf{B}$ are defined as, $\mathbf{D} = \epsilon_0 \epsilon(\mathbf{r})\mathbf{E}$ and $\mathbf{B} = \mu_0 \mu(\mathbf{r})\mathbf{H}$ where $\epsilon(\mathbf{r})$ and $\mu(\mathbf{r})$ are the relative permittivity and permeability of the medium that are functions of position. Substituting these two definitions into Maxwell's curl Equations for $\mathbf{D}$ and $\mathbf{B}$,

$$\nabla \times \mathbf{H} = \frac{\partial \mathbf{D}}{\partial t} = \frac{\partial}{\partial t}\left[\epsilon_0 \epsilon(\mathbf{r})\mathbf{E}\right] = \epsilon_0 \epsilon(\mathbf{r}) \frac{\partial \mathbf{E}}{\partial t} \tag{2.4}$$

$$\nabla \times \mathbf{E} = -\frac{\partial \mathbf{B}}{\partial t} = -\frac{\partial}{\partial t}\left[\mu_0 \mu(\mathbf{r})\mathbf{H}\right] = -\mu_0 \mu(\mathbf{r}) \frac{\partial \mathbf{H}}{\partial t} \tag{2.5}$$

and dividing by $\epsilon(\mathbf{r})$ and $\mu(\mathbf{r})$,

$$\frac{1}{\epsilon(\mathbf{r})} \nabla \times \mathbf{H} = \epsilon_0 \frac{\partial \mathbf{E}}{\partial t} \tag{2.6}$$

$$\frac{1}{\mu(\mathbf{r})} \nabla \times \mathbf{E} = -\mu_0 \frac{\partial \mathbf{H}}{\partial t} \tag{2.7}$$

Now taking curl of both sides of Equation 2.6 and Equation 2.7 we have,

$$\nabla \times \left[\frac{1}{\epsilon(\mathbf{r})} \nabla \times \mathbf{H}\right] = \epsilon_0 \frac{\partial}{\partial t}\left[\nabla \times \mathbf{E}\right] \tag{2.8}$$

$$\nabla \times \left[\frac{1}{\mu(\mathbf{r})} \nabla \times \mathbf{E}\right] = -\mu_0 \frac{\partial}{\partial t}\left[\nabla \times \mathbf{H}\right] \tag{2.9}$$

substituting Equation 2.5 and Equation 2.4 for the expressions $\nabla \times \mathbf{E}$ and $\nabla \times \mathbf{H}$ on the right-side of Equation 2.8 and Equation 2.9 then we have,

$$\nabla \times \left[\frac{1}{\epsilon(\mathbf{r})}\nabla \times \mathbf{H}\right] = -\epsilon_0\mu_0\mu(\mathbf{r})\frac{\partial^2\mathbf{H}}{\partial t^2} \quad (2.10)$$

$$\nabla \times \left[\frac{1}{\mu(\mathbf{r})}\nabla \times \mathbf{E}\right] = -\epsilon_0\mu_0\epsilon(\mathbf{r})\frac{\partial^2\mathbf{E}}{\partial t^2} \quad (2.11)$$

and using $\mu_0\epsilon_0 = 1/c^2$, where c is speed of light in free space, then we finally have written Maxwell's equations for magnetic field, $\mathbf{H}$, and electric field, $\mathbf{E}$, which are,

$$\nabla \times \left[\frac{1}{\epsilon(\mathbf{r})}\nabla \times \mathbf{H}\right] + \frac{1}{c^2}\mu(\mathbf{r})\frac{\partial^2\mathbf{H}}{\partial t^2} = 0 \quad (2.12)$$

$$\nabla \times \left[\frac{1}{\mu(\mathbf{r})}\nabla \times \mathbf{E}\right] + \frac{1}{c^2}\epsilon(\mathbf{r})\frac{\partial^2\mathbf{E}}{\partial t^2} = 0 \quad (2.13)$$

These two equations (Eq. 2.12 and Eq. 2.13) are the starting point of solving the problems in this thesis. Together with the divergence equation, for a given periodic dielectric medium it tells us everything we need to know about the magnetic field, $\mathbf{H}$, and the electric field $\mathbf{E}$ and the corresponding frequencies.

2.1.1. Plane Wave Expansion Method

Both $\mathbf{H}$ and $\mathbf{E}$ fields are functions of position and time, $\mathbf{H}(\mathbf{r}, t)$ and $\mathbf{E}(\mathbf{r}, t)$. To deal with the time dependence we first take Fourier Transform with respect to time. In 3-dimensions, the electric and magnetic properties of materials are defined as $\epsilon(\mathbf{r})$ and $\mu(\mathbf{r})$ where $\mathbf{r} = x\mathbf{i} + y\mathbf{j} + z\mathbf{k}$. The electric and magnetic fields are defined as,

$$\mathbf{H}(\boldsymbol{r}, t) = \int_{-\infty}^{\infty} \mathbf{H}(\boldsymbol{r}, \omega)e^{-i\omega t}d\omega \quad (2.14)$$

$$\mathbf{E}(\boldsymbol{r}, t) = \int_{-\infty}^{\infty} \mathbf{E}(\boldsymbol{r}, \omega)e^{-i\omega t}d\omega \quad (2.15)$$

Putting these two equations into Equation 2.12 and Equation 2.13 then we have,

$$\begin{aligned}\int_{-\infty}^{\infty} e^{-i\omega t} d\omega \left\{ \nabla \times \left[\frac{1}{\epsilon(\boldsymbol{r})} \nabla \times \mathbf{H} \right] - \frac{\omega^2}{c^2} \mu(\boldsymbol{r}) \mathbf{H} \right\} &= 0 \\ \int_{-\infty}^{\infty} e^{-i\omega t} d\omega \left\{ \nabla \times \left[\frac{1}{\mu(\boldsymbol{r})} \nabla \times \mathbf{E} \right] - \frac{\omega^2}{c^2} \epsilon(\boldsymbol{r}) \mathbf{E} \right\} &= 0 \end{aligned} \tag{2.16}$$

Since the Fourier Transform of each term in curly braces vanishes, the terms in each curly brace must vanish, then we have

$$\nabla \times [\eta(\mathbf{r}) \nabla \times \mathbf{H}] - \frac{\omega^2}{c^2} \mu(\boldsymbol{r}) \mathbf{H} = 0 \tag{2.17}$$

$$\nabla \times [\zeta(\mathbf{r}) \nabla \times \mathbf{E}] - \frac{\omega^2}{c^2} \epsilon(\boldsymbol{r}) \mathbf{E} = 0 \tag{2.18}$$

where $\zeta(\mathbf{r}) = 1/\mu(\mathbf{r})$ and $\eta(\mathbf{r}) = 1/\epsilon(\mathbf{r})$. After we eliminated time dependence, now we write $\mathbf{E}(\boldsymbol{r})$ and $\mathbf{H}(\boldsymbol{r})$ as,

$$\mathbf{H}(\boldsymbol{r}) = \int_{all\,\mathbf{q}} \mathbf{H}(\mathbf{q}) e^{i\mathbf{q}\cdot\boldsymbol{r}} d^3\mathbf{q} \tag{2.19}$$

$$\mathbf{E}(\boldsymbol{r}) = \int_{all\,\mathbf{q}} \mathbf{E}(\mathbf{q}) e^{i\mathbf{q}\cdot\boldsymbol{r}} d^3\mathbf{q} \tag{2.20}$$

and plugging them into Equation 2.17 and 2.18

$$\nabla \times \left[\eta(\mathbf{r}) \nabla \times \int_{all\,\mathbf{q}} \mathbf{H}(\mathbf{q}) e^{i\mathbf{q}\cdot\boldsymbol{r}} d^3\mathbf{q} \right] - \frac{\omega^2}{c^2} \mu(\boldsymbol{r}) \int_{all\,\mathbf{q}} \mathbf{H}(\mathbf{q}) e^{i\mathbf{q}\cdot\boldsymbol{r}} d^3\mathbf{q} = 0 \tag{2.21}$$

$$\nabla \times \left[\zeta(\mathbf{r}) \nabla \times \int_{all\,\mathbf{q}} \mathbf{E}(\mathbf{q}) e^{i\mathbf{q}\cdot\boldsymbol{r}} d^3\mathbf{q} \right] - \frac{\omega^2}{c^2} \epsilon(\boldsymbol{r}) \int_{all\,\mathbf{q}} \mathbf{E}(\mathbf{q}) e^{i\mathbf{q}\cdot\boldsymbol{r}} d^3\mathbf{q} = 0 \tag{2.22}$$

Note that these two equations are similar, which means we can get one from another by substituting $\mathbf{E} \to \mathbf{H}$, $\epsilon \to \mu$, and $\zeta \to \eta$. From here we can continue with one of these, say Eq. 2.22. To evaluate the curl of the integral containing $\mathbf{E}(\mathbf{q})$, we use the vector

identity $\nabla \times (f\mathbf{A}) = f(\nabla \times \mathbf{A}) - \mathbf{A} \times (\nabla f)$ and recalling that ∇ operates only on $\mathbf{r}$,

$$\begin{aligned}
\nabla \times \int_{all\,\mathbf{q}} d^3\mathbf{q}\mathbf{E}(\mathbf{q})e^{i\mathbf{q}\cdot\boldsymbol{r}} &= \int_{all\,\mathbf{q}} d^3\mathbf{q}\nabla \times \left[e^{i\mathbf{q}\cdot\boldsymbol{r}}\mathbf{E}(\mathbf{q})\right] \\
&= \int_{all\,\mathbf{q}} d^3\mathbf{q}\left[e^{i\mathbf{q}\cdot\boldsymbol{r}}(\nabla \times \mathbf{E}(\mathbf{q})) - \mathbf{E}(\mathbf{q}) \times (\nabla e^{i\mathbf{q}\cdot\boldsymbol{r}})\right] \\
&= \int_{all\,\mathbf{q}} d^3\mathbf{q}\left[0 - \mathbf{E}(\mathbf{q}) \times (i\mathbf{q}e^{i\mathbf{q}\cdot\boldsymbol{r}})\right] \\
&= \int_{all\,\mathbf{q}} d^3\mathbf{q}\, i\mathbf{q} \times \mathbf{E}(\mathbf{q})e^{i\mathbf{q}\cdot\boldsymbol{r}} \qquad (2.23)
\end{aligned}$$

and we write periodic functions, $\epsilon(\boldsymbol{r})$, $\mu(\boldsymbol{r})$, $\eta(\boldsymbol{r})$, and $\zeta(\boldsymbol{r})$ as,

$$\begin{aligned}
\epsilon(\boldsymbol{r}) &= \sum_{\mathbf{G}} \epsilon(\mathbf{G})e^{i\mathbf{G}\cdot\boldsymbol{r}} \qquad \mu(\boldsymbol{r}) = \sum_{\mathbf{G}} \mu(\mathbf{G})e^{i\mathbf{G}\cdot\boldsymbol{r}} \\
\eta(\boldsymbol{r}) &= \sum_{\mathbf{G}} \eta(\mathbf{G})e^{i\mathbf{G}\cdot\boldsymbol{r}} \qquad \zeta(\boldsymbol{r}) = \sum_{\mathbf{G}} \zeta(\mathbf{G})e^{i\mathbf{G}\cdot\boldsymbol{r}} \qquad (2.24)
\end{aligned}$$

where $\eta(\boldsymbol{r}) = 1/\epsilon(\boldsymbol{r})$ and $\zeta(\boldsymbol{r}) = 1/\mu(\boldsymbol{r})$. Now we put Equation 2.19, Equation 2.20 and Equation 2.24 into Equation 2.17 and Equation 2.18. The integral over $\mathbf{q}$ is over the entire reciprocal space. This space can be broken up into "cells" defined by the basis vectors b_i, so that

$$\int_{all\,\mathbf{q}} d\mathbf{q} f(\mathbf{q}) \longrightarrow \int_{cell} d\mathbf{k} \sum_{\mathbf{G}} f(\mathbf{k} + \mathbf{G}) \qquad (2.25)$$

Eq. 2.22 becomes

$$\begin{aligned}
\nabla \times \left[\left(\sum_{\mathbf{G}''} \zeta(\mathbf{G}'')e^{i\mathbf{G}''\cdot\mathbf{r}}\right)\left(\int_{all\,\mathbf{q}} d^3\mathbf{q}\, i\mathbf{q} \times \mathbf{E}(\mathbf{q})e^{i\mathbf{q}\cdot\boldsymbol{r}}\right)\right] \\
- \frac{\omega^2}{c^2}\left(\sum_{\mathbf{G}} \epsilon(\mathbf{G})e^{i\mathbf{G}\cdot\mathbf{r}}\right)\left(\int_{all\,\mathbf{q}} d^3\mathbf{q}\,\mathbf{E}(\mathbf{q})e^{i\mathbf{q}\cdot\boldsymbol{r}}\right) = 0
\end{aligned}$$

$$\nabla \times \left[\left(\sum_{\mathbf{G}''} \zeta(\mathbf{G}'') e^{i\mathbf{G}''\cdot\mathbf{r}} \right) \left(\int_{cell} d^3\mathbf{k} \sum_{\mathbf{G}'} i(\mathbf{k}+\mathbf{G}') \times \mathbf{E}(\mathbf{q}+\mathbf{G}') e^{i\mathbf{q}\cdot\boldsymbol{r}} \right) \right] - \frac{\omega^2}{c^2} \left(\sum_{\mathbf{G}''} \epsilon(\mathbf{G}'') e^{i\mathbf{G}''\cdot\mathbf{r}} \right) \left(\int_{cell} d^3\mathbf{k} \sum_{\mathbf{G}'} \mathbf{E}(\mathbf{k}+\mathbf{G}') e^{i(\mathbf{k}+\mathbf{G}')\cdot\boldsymbol{r}} \right) = 0$$

$$\int_{cell} d^3\mathbf{k} \sum_{\mathbf{G}''} \sum_{\mathbf{G}'} \zeta(\mathbf{G}'') \nabla \times \left[i(\mathbf{k}+\mathbf{G}') \times \mathbf{E}(\mathbf{k}+\mathbf{G}') e^{i(\mathbf{k}+\mathbf{G}'+\mathbf{G}'')\cdot\mathbf{r}} \right] - \frac{\omega^2}{c^2} \int_{cell} d^3\mathbf{k} \sum_{\mathbf{G}''} \sum_{\mathbf{G}'} \epsilon(\mathbf{G}'') \mathbf{E}(\mathbf{k}+\mathbf{G}') e^{i(\mathbf{k}+\mathbf{G}'+\mathbf{G}'')\cdot\mathbf{r}} = 0$$

$$\int_{cell} d^3\mathbf{k} \sum_{\mathbf{G}''} \sum_{\mathbf{G}'} e^{i(\mathbf{k}+\mathbf{G}'+\mathbf{G}'')\cdot\mathbf{r}} \left\{ \zeta(\mathbf{G}'') i(\mathbf{k}+\mathbf{G}'+\mathbf{G}'') \times \left[i(\mathbf{k}+\mathbf{G}') \times \mathbf{E}(\mathbf{k}+\mathbf{G}') \right] - \frac{\omega^2}{c^2} \epsilon(\mathbf{G}'') \mathbf{E}(\mathbf{k}+\mathbf{G}') \right\} = 0$$

Letting $\mathbf{G} = \mathbf{G}' + \mathbf{G}''$

$$\int_{cell} d^3\mathbf{k} \sum_{\mathbf{G}} e^{i(\mathbf{k}+\mathbf{G})\cdot\mathbf{r}} \left\{ \sum_{\mathbf{G}'} \zeta(\mathbf{G}-\mathbf{G}')(\mathbf{k}+\mathbf{G}) \times \left[(\mathbf{k}+\mathbf{G}') \times \mathbf{E}(\mathbf{k}+\mathbf{G}') \right] + \frac{\omega^2}{c^2} \sum_{\mathbf{G}'} \epsilon(\mathbf{G}-\mathbf{G}') \mathbf{E}(\mathbf{k}+\mathbf{G}') \right\} = 0$$

Applying Eq. 2.25

$$\int_{all\,\mathbf{q}} d^3\mathbf{q} e^{i\mathbf{q})\cdot\mathbf{r}} \left\{ \sum_{\mathbf{G}'} \zeta(\mathbf{G}-\mathbf{G}')(\mathbf{k}+\mathbf{G}) \times \left[(\mathbf{k}+\mathbf{G}') \times \mathbf{E}(\mathbf{k}+\mathbf{G}') \right] + \frac{\omega^2}{c^2} \sum_{\mathbf{G}'} \epsilon(\mathbf{G}-\mathbf{G}') \mathbf{E}(\mathbf{k}+\mathbf{G}') \right\} = 0$$

The Fourier Transform of the term in curly braces vanishes, which implies that the term itself must vanish

$$\sum_{\mathbf{G}'} \zeta(\mathbf{G}-\mathbf{G}')(\mathbf{k}+\mathbf{G}) \times \left[(\mathbf{k}+\mathbf{G}') \times \mathbf{E}(\mathbf{k}+\mathbf{G}')\right] + \frac{\omega^2}{c^2} \sum_{\mathbf{G}'} \epsilon(\mathbf{G}-\mathbf{G}')\mathbf{E}(\mathbf{k}+\mathbf{G}') = 0 \tag{2.26}$$

A similar equation for magnetic field, $\mathbf{H}$, is obtained by the substitution $\mathbf{E} \to \mathbf{H}$, $\epsilon \to \mu$, and $\zeta \to \eta$.

$$\sum_{\mathbf{G}'} \eta(\mathbf{G}-\mathbf{G}')(\mathbf{k}+\mathbf{G}) \times \left[(\mathbf{k}+\mathbf{G}') \times \mathbf{H}(\mathbf{k}+\mathbf{G}')\right] + \frac{\omega^2}{c^2} \sum_{\mathbf{G}'} \mu(\mathbf{G}-\mathbf{G}')\mathbf{H}(\mathbf{k}+\mathbf{G}') = 0 \tag{2.27}$$

Equations 2.26 and 2.27 are quite general and are valid for any medium that consists of linear, lossless, and locally isotropic materials. They are infinite-dimensional generalized eigenvalue problems of the form $Ax = \lambda Bx$. Of course, they must be truncated to be solved. Choosing a finite basis consisting of N points in the reciprocal lattice, $\mathbf{G}_1, \ldots, \mathbf{G}_N$, the eigenvector $\mathbf{E}(\mathbf{k}+\mathbf{G})$ is a column vector of $3N$ elements and A and B are $3N \times 3N$ matrices. It is best to think of A and B as $N \times N$ matrices of 3×3 blocks. Thus, with IJ denoting the row, column index of each block, and ij denoting the row, column index within each 3×3 block. A and B in Eq. 2.26 can be written as

$$\begin{aligned}
A_{IJ,ij} &= \zeta(\mathbf{G}_I - \mathbf{G}_J)\left\{(\mathbf{k}+\mathbf{G}_I)\cdot(\mathbf{k}+\mathbf{G}_J)\delta_{ij} - \left[(\mathbf{k}+\mathbf{G}_I)\cdot\hat{e}_j\right]\left[(\mathbf{k}+\mathbf{G}_J)\cdot\hat{e}_i\right]\right\} \\
B_{IJ,ij} &= \epsilon(\mathbf{G}_I - \mathbf{G}_J)\delta_{ij} \\
x_{I,i} &= \mathbf{E}(\mathbf{k}+\mathbf{G}_I)\cdot\hat{e}_i \\
\lambda &= \frac{\omega^2}{c^2}
\end{aligned} \tag{2.28}$$

where $\hat{e}_1$, $\hat{e}_2$, and $\hat{e}_3$ denotes the unit vectors in the $x-$, $y-$, and $z-$axis. Matrix-matrix and matrix-vector multiplications are written as

$$[Ax]_{I,i} = \sum_{J=1}^{N}\sum_{j=1}^{3} A_{IJ,ij}x_{J,j} \quad and \quad [AB]_{I,i} = \sum_{K=1}^{N}\sum_{k=1}^{3} A_{IK,ik}B_{KJ,kj} \tag{2.29}$$

The matrix A and B and the vector x can be written explicitly as

$$A = \left[\begin{array}{c|c|c|c} a_{11} & a_{12} & \cdots & a_{1N} \\ \hline a_{21} & a_{22} & \cdots & a_{2N} \\ \hline \vdots & \vdots & \ddots & \vdots \\ \hline a_{N1} & a_{N2} & \cdots & a_{NN} \end{array}\right] \quad B = \left[\begin{array}{c|c|c|c} b_{11} & b_{12} & \cdots & b_{1N} \\ \hline b_{21} & b_{22} & \cdots & b_{2N} \\ \hline \vdots & \vdots & \ddots & \vdots \\ \hline b_{N1} & b_{N2} & \cdots & b_{NN} \end{array}\right] \quad x = \left[\begin{array}{c} E_x(\mathbf{k}+\mathbf{G}_1) \\ E_y(\mathbf{k}+\mathbf{G}_1) \\ E_z(\mathbf{k}+\mathbf{G}_1) \\ \hline E_x(\mathbf{k}+\mathbf{G}_2) \\ E_y(\mathbf{k}+\mathbf{G}_2) \\ E_z(\mathbf{k}+\mathbf{G}_2) \\ \hline \vdots \\ \hline E_x(\mathbf{k}+\mathbf{G}_N) \\ E_y(\mathbf{k}+\mathbf{G}_N) \\ E_z(\mathbf{k}+\mathbf{G}_N) \end{array}\right]$$

with a_{IJ} itself a 3×3 matrix given by

$$a_{IJ} = \zeta(\mathbf{G}_I - \mathbf{G}_J) \begin{bmatrix} (\mathbf{q}_I \cdot \mathbf{q}_J - q_{Ix}q_{Jx}) & -q_{Iy}q_{Jx} & -q_{Iz}q_{Jx} \\ -q_{Ix}q_{Jy} & (\mathbf{q}_I \cdot \mathbf{q}_J - q_{Iy}q_{Jy}) & -q_{Iz}q_{Jy} \\ -q_{Ix}q_{Jz} & -q_{Iy}q_{Jz} & (\mathbf{q}_I \cdot \mathbf{q}_J - q_{Iz}q_{Jz}) \end{bmatrix}$$

where $\mathbf{q}_I = (\mathbf{k} + \mathbf{G}_I)$, and $\mathbf{q}_J = (\mathbf{k} + \mathbf{G}_J)$, and

$$b_{IJ} = \epsilon(\mathbf{G}_I - \mathbf{G}_J) \begin{bmatrix} 1 & 0 & 0 \\ 0 & 1 & 0 \\ 0 & 0 & 1 \end{bmatrix}$$

2.1.2. Finite-Difference Time-Domain Method

In this thesis we used the finite-difference time-domain (FDTD) method (Taflove et al., 2005) to simulate the propagation of electromagnetic field in a dielectric medium using a freely available software package MEEP (Oskooi et al., 2010). So we will give a short introduction of FDTD method. Finite-difference time-domain method is a numerical method that is used to solve Maxwell's curl equations by dividing space and time into small grid. The solution method introduced by (Yee, 1966) is based on discretizing Maxwell's curl equation in time and space. And the discretized differential equations are solved by evolving both time and space.

We start with two Maxwell's curl equations for electric field and magnetic fields,

$$\frac{\partial \mathbf{H}}{\partial t} = -\frac{1}{\mu_0 \mu} \nabla \times \mathbf{E} \tag{2.30}$$

$$\frac{\partial \mathbf{E}}{\partial t} = \frac{1}{\epsilon_0 \epsilon} \{\nabla \times \mathbf{H} - \mathbf{J}_{source}\} \tag{2.31}$$

where $\mathbf{J}_{source}$ is current source. After taking the curl of both field then we will have six scalar equation for each component,

$$\frac{\partial H_x}{\partial t} = \frac{1}{\mu_0 \mu} \left\{ \frac{\partial E_y}{\partial z} - \frac{\partial E_z}{\partial y} \right\} \tag{2.32}$$

$$\frac{\partial H_y}{\partial t} = \frac{1}{\mu_0 \mu} \left\{ \frac{\partial E_z}{\partial x} - \frac{\partial E_x}{\partial z} \right\} \tag{2.33}$$

$$\frac{\partial H_z}{\partial t} = \frac{1}{\mu_0 \mu} \left\{ \frac{\partial E_x}{\partial y} - \frac{\partial E_y}{\partial x} \right\} \tag{2.34}$$

$$\frac{\partial E_x}{\partial t} = \frac{1}{\epsilon_0 \epsilon} \left\{ \frac{\partial H_z}{\partial y} - \frac{\partial H_y}{\partial z} - J_{x,source} \right\} \tag{2.35}$$

$$\frac{\partial E_y}{\partial t} = \frac{1}{\epsilon_0 \epsilon} \left\{ \frac{\partial H_x}{\partial z} - \frac{\partial H_z}{\partial x} - J_{y,source} \right\} \tag{2.36}$$

$$\frac{\partial E_z}{\partial t} = \frac{1}{\epsilon_0 \epsilon} \left\{ \frac{\partial H_y}{\partial x} - \frac{\partial H_x}{\partial y} - J_{z,source} \right\} \tag{2.37}$$

and for one-dimension, lets consider the electromagnetic filed is travelling in the x-

direction and we set electric field in the z-direction and we set magnetic field in the y-direction. So the partial derivative of field component with respect to y- and z-direction vanishes leaving only two equations,

$$\frac{\partial H_y}{\partial t} = \frac{1}{\mu_0 \mu} \frac{\partial E_z}{\partial x} \tag{2.38}$$

$$\frac{\partial E_z}{\partial t} = \frac{1}{\epsilon_0 \epsilon} \left\{ \frac{\partial H_y}{\partial x} - J_{z,source} \right\} \tag{2.39}$$

now we need to understand notation that is used by Yee. A point in discretized space is represented by $(i, j, k) = (i\Delta x, j\Delta y, k\Delta z)$ where i, j, k are integers, $\Delta x, \Delta y, \Delta z$ are increments in coordinates x, y, z. Keeping time step constant, the finite-difference expression for space derivative in the x-direction of electric field and magnetic field can be written as,

$$\frac{\partial E_z}{\partial x}(i\Delta x, j\Delta y, k\Delta z, n\Delta t) = \frac{E_z|^n_{i+1/2,j,k} - E_z|^n_{i-1/2,j,k}}{\Delta x} \tag{2.40}$$

$$\frac{\partial H_y}{\partial x}(i\Delta x, j\Delta y, k\Delta z, n\Delta t) = \frac{H_y|^n_{i+1/2,j,k} - H_y|^n_{i-1/2,j,k}}{\Delta x} \tag{2.41}$$

where n is integer and Δt is increment in time t. This time keeping space constant, partial derivative with respect to time of electric field and magnetic field are defined as,

$$\frac{\partial E_z}{\partial t}(i\Delta x, j\Delta y, k\Delta z, n\Delta t) = \frac{E_z|^{n+1/2}_{i,j,k} - E_z|^{n-1/2}_{i,j,k}}{\Delta t} \tag{2.42}$$

$$\frac{\partial H_y}{\partial t}(i\Delta x, j\Delta y, k\Delta z, n\Delta t) = \frac{H_y|^{n+1/2}_{i,j,k} - H_y|^{n-1/2}_{i,j,k}}{\Delta t} \tag{2.43}$$

now putting Equation 2.40 and Equation 2.43 into Equation 2.38 and putting Equation 2.41

and Equation 2.42 into Equation 2.39 then we will have,

$$\frac{H_y|_{i,j,k}^{n+1/2} - H_y|_{i,j,k}^{n-1/2}}{\Delta t} = \frac{1}{\mu_0 \mu_{i+1/2,j,k}} \frac{E_z|_{i+1/2,j,k}^{n} - E_z|_{i-1/2,j,k}^{n}}{\Delta x} \tag{2.44}$$

$$\frac{E_z|_{i,j,k}^{n+1/2} - E_z|_{i,j,k}^{n-1/2}}{\Delta t} = \frac{1}{\epsilon_0 \epsilon_{i+1/2,j,k}} \left\{ \frac{H_y|_{i+1/2,j,k}^{n} - H_y|_{i-1/2,j,k}^{n}}{\Delta x} - J_z|_{i+1/2,j,k} \right\} \tag{2.45}$$

or more clearly,

$$H_y|_{i,j,k}^{n+1/2} = H_y|_{i,j,k}^{n-1/2} + \frac{\Delta t}{\mu_0 \mu_{i+1/2,j,k} \Delta x} \left\{ E_z|_{i+1/2,j,k}^{n} - E_z|_{i-1/2,j,k}^{n} \right\} \tag{2.46}$$

$$E_z|_{i,j,k}^{n+1/2} = E_z|_{i,j,k}^{n-1/2} + \frac{\Delta t}{\epsilon_0 \epsilon_{i+1/2,j,k} \Delta x} \left\{ H_y|_{i+1/2,j,k}^{n} - H_y|_{i-1/2,j,k}^{n} - J_z|_{i+1/2,j,k} \right\} \tag{2.47}$$

Where J_z is the current source in the z-direction. As can be seen from Equation 2.46 to find magnetic field at time step $n + 1/2$ and space point i, j, k we need to know electric field at space point $i + 1/2, j, k$ and $i - 1/2, j, k$ and time step n, in addition we need to know magnetic field at time step $n - 1/2$ and space point i, j, k. In similar way, as can be seen from Equation 2.47 to find the electric field at time step $n + 1/2$ and space point i, j, k we need to know magnetic field at space point $i+1/2, j, k$ and $i-1/2, j, k$ and time step n, in addition we need to know electric field at time step $n - 1/2$ and space point i, j, k.

2.1.3. Blackbody Radiation

A black body is one that completely adsorbs any electromagnetic (EM) radiation that it is exposed to. A black body radiates well because it must emit radiation at the same rate that it absorbs to maintain thermal equilibrium. The spectral radiance, which defines the radiation emitted from a blackbody at a particular frequency and temperature and the mathematical expression for blackbody is

$$B(\nu, T) = \frac{4\pi h}{c^2} \frac{\nu^3}{e^{h\nu/kT} - 1} \tag{2.48}$$

The frequency for which the spectral radiance is maximum can be found by solving $\frac{d}{d\nu}[B(\nu)] = 0$ for $\nu = \nu_{max}$. After solving for ν_{max} we obtain

$$\nu_{max} = 5.879 \times 10^{10} \times T \ (Hz/K) \tag{2.49}$$

In the same way, the wavelength for which the spectral radiance is maximum can be calculated by first expressing Eq. 2.48 in terms of wavelength

$$B(\lambda, T) = \frac{4\pi hc^2}{\lambda^5} \frac{1}{e^{hc/\lambda kT} - 1} \tag{2.50}$$

and solve $\frac{d}{d\lambda}[B(\lambda)] = 0$ for $\lambda = \lambda_{max}$, and solving for λ_{max} we obtain

$$\lambda_{max} = 2.898 \times 10^{-3}/T \ (m.K) \tag{2.51}$$

which is known as Wien's displacement law.

The graph of Eq. 2.48 is plotted for five different temperature, $T = 300K$, $T = 500K$, $T = 1000K$, $T = 1500K$, and $T = 5777K$. As is clear from the Fig. 2.1, objects that are at room temperature radiate primarily in the infrared regime of EM spectrum. We describe an object as red hot when it reaches a temperature of $1000K$ and starts to glow with a red color. When the temperature is increased further, to a temperature of $5777K$,

which is the surface temperature of the sun, it radiates the entire visible spectrum and referred as being white hot.

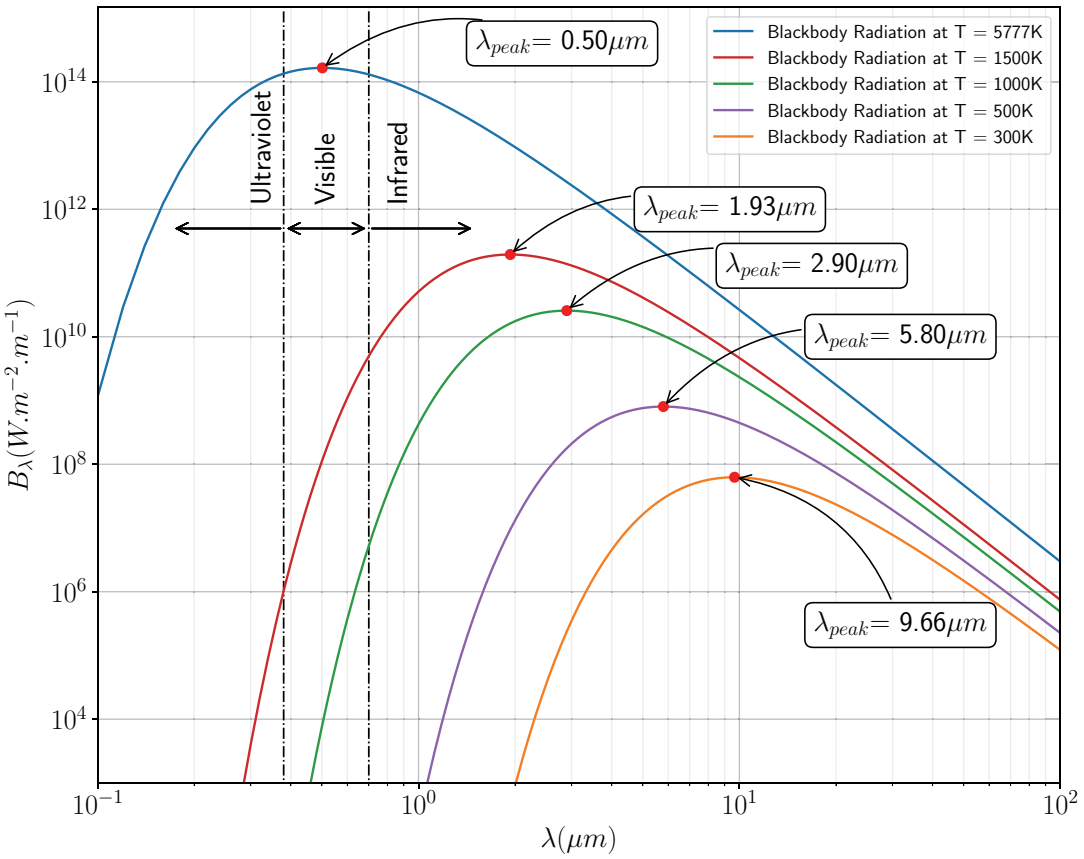


Figure 2.1. Spectral radiance as a function of wavelength of an ideal blackbody for five different temperature, $T=300K$, $T=500K$, $T=1000K$, $T=1500K$, and $T=5777K$.

Integrating Eq. 2.48 over all frequencies we obtain the total energy, which is simply total area under curve described by Eq. 2.48

$$P = \int_0^\infty B(\nu)d\nu = \frac{8\pi^5 k^4}{15c^3h^3}T^4 \tag{2.52}$$

which states that the total energy is proportional to the forth power of temperature. We therefore expect that the energy radiated by an object per second per unit area is also proportional to fourth power of temperature. This statement is described by Stefan-Boltzmann law:

$$R = \varepsilon\sigma T^4 \tag{2.53}$$

where σ is the Stefan's constant and ε is the emissivity and is a measure of how close the object's surface is to blackbody surface. Numerical value of emisivity ranges from 0 (no radiation) to 1 (blackbody).

For human body skin at temperature of $37°C$ $(310K)$, spectral radiance is shown in Fig. 2.2.

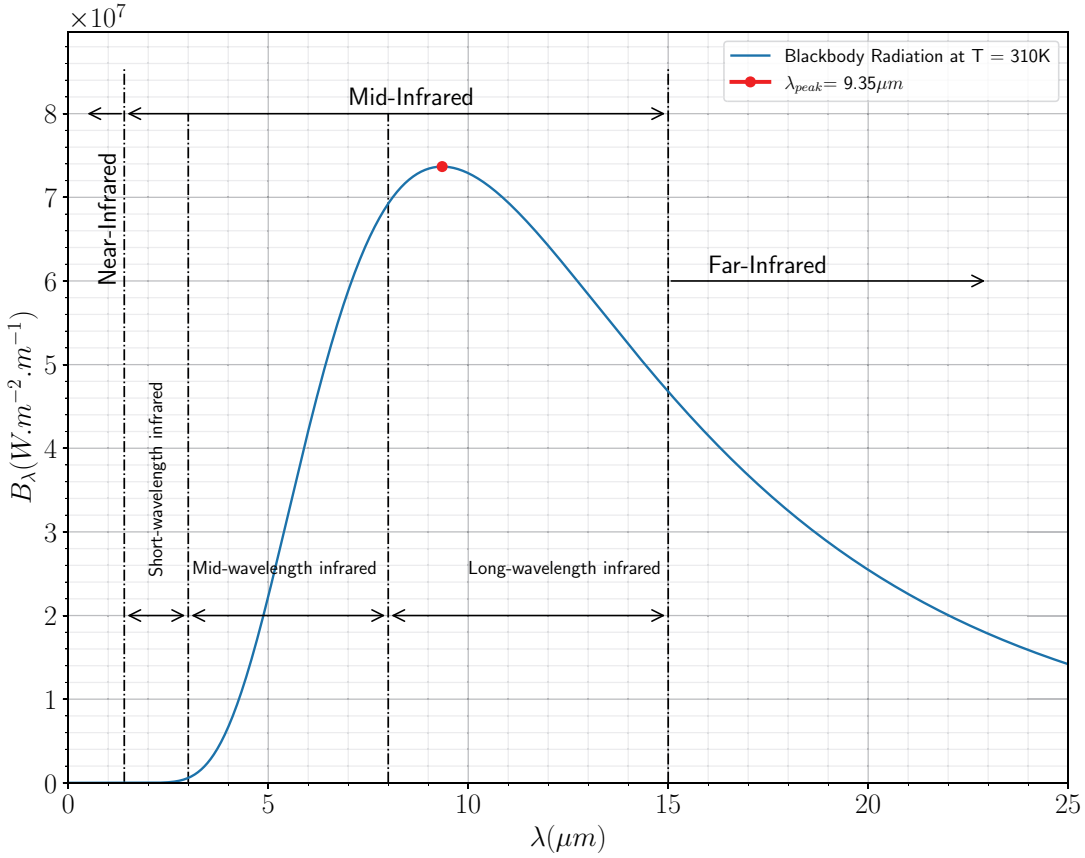


Figure 2.2. Spectral radiance as a function of wavelength of an ideal blackbody at temperature $T = 310$K.

As it is seen the radiation is in the infrared portion of the electromagnetic spectrum. This portion of spectrum is further divided in three region, which are Near-, Mid-, and Far-infrared. Mid-infrared is also divided into Short-wavelength, Mid-wavelength, and Long-wavelength regions. At this temperature $(310K)$ the wavelength at which the energy density is maximum is found using Eq. 2.51, $\lambda_{max} = 9.35\mu m$. The most of power radiated by human body is around this value. That is why infrared detectors are designed to be sensitive to wavelength ranging from $7\mu m$ to $14\mu m$.

Starting from this point, we will use frequency dependent spectral radiation for-

mula which is more practical since the frequency is conserved when entering into a different medium. The graph shown in Fig. 2.3 is plotted for skin temperature of $T = 310K$. The frequency for which the maximum energy is radiated can be found by using Eq. 2.49, $\nu_{max} = 18.225THz$. The graph clearly shows that maximum radiation occurs around this value.

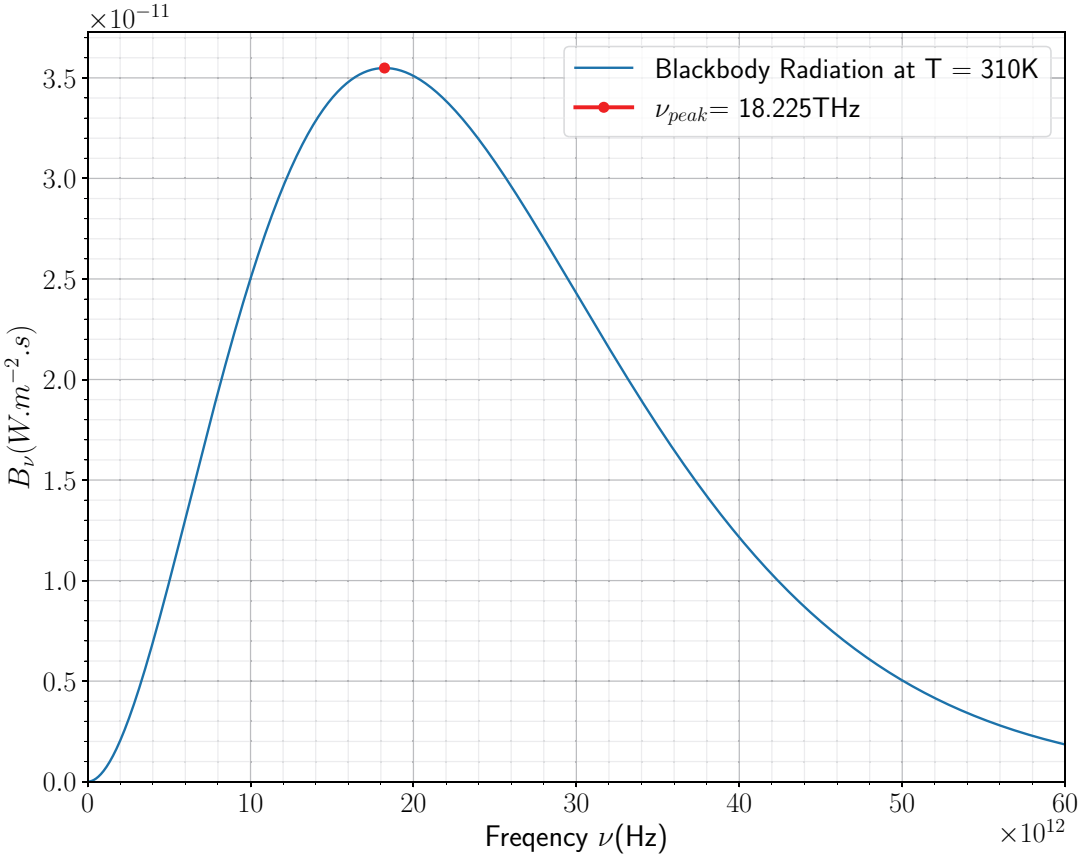


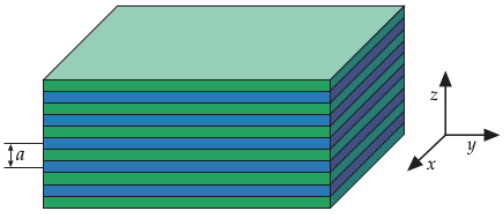
Figure 2.3. Spectral radiance as a function of frequency of an ideal blackbody at temperature $T = 310$K.

Another practical quantity that can be derived is the total power radiated by a blackbody which is calculated by multiplying Eq. 2.53 with its surface area, which is $P_{radiated} = \varepsilon\sigma AT^4$. In an environment with temperature T_0 the overall radiated power is $P_{tot} = P_{radiated} - P_{absorbed} = \varepsilon\sigma A(T^4 - T_0^4)$.

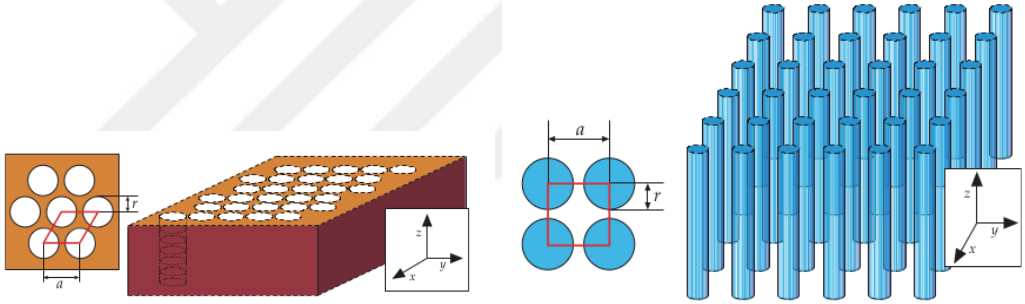
CHAPTER 3

PHOTONIC CRYSTAL TEXTILES

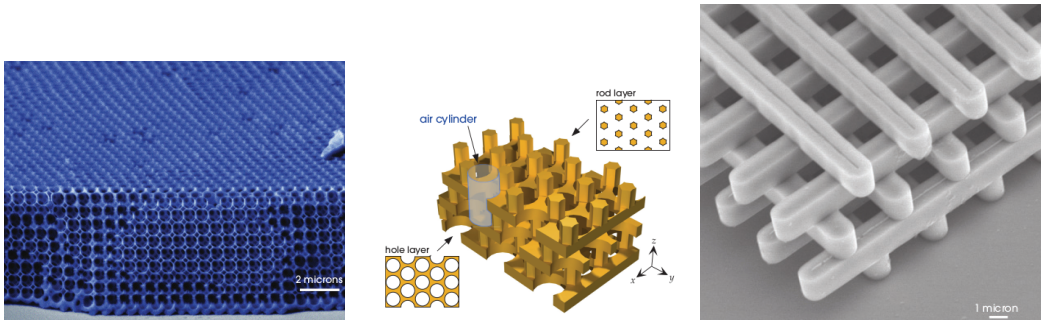
Considering the fact that approximately two-thirds of the heat loss of the human body occurs through electromagnetic radiation, it becomes important to consider photonic crystals for the purpose of reducing heat loss.



(a) 1D Photonic Crystal (Multi-layer structure)



(b) 2D Photonic Crystals.



(c) 3D Photonic Crystals.

Figure 3.1. (a) One-dimensional, (b) two-dimensional (Joannopoulos et al., 2008), and (c) three- dimensional (Lin et al., 1998), (Vlasov et al., 2001) (Johnson and Joannopoulos, 2000) photonic crystals examples.

Photonic crystals are structures whose optical properties such as dielectric constant and/or geometric parameters vary periodically in space. They can be classified as one-dimensional, two-dimensional, and three-dimensional. Some examples are shown in Fig. 3.1. Those structures possess photonic band gap (PBG) and propagation of electromagnetic waves with a frequency falling into this gap can be entirely prohibited.

The idea to produce woven photonic crystals to reduce heat loss by radiation was originally proposed by John Pendry (Tsai et al., 1998), (Tsai et al., 1999). Solutions proposed so far involve the production of photonic crystals and somehow embedding them into or fixing them onto textiles. We observe that the textile, by virtue of the fact that it has been produced by weaving, already has a periodic structure, and thus is a potential candidate for a photonic crystal. So it's not necessary to manufacture a separate photonic crystal and somehow "mount" it on the textile. If the fiber that the textile is woven from has the necessary optical and geometrical properties, and is woven with the right weave pattern, then the textile itself would be a thin layer of a photonic crystal. To this end, synthetic fibers with a high refractive index appear as viable solutions. We suspect multilayer and three-dimensional weaving patterns would most likely yield optimal results. In this thesis we will scan two main parameters for a fixed dielectric constant: (1) Thickness of the fibers. (2) Weave pattern.

These parameters will be scanned to determine the best structure that maximizes the reflection of the blackbody radiation from the human body with a skin temperature of $37°$C. Even though we aim to find the woven structure that maximizes the reflection of radiation from an object around the human body's skin temperature, the same approach can, in principle, be used to find structures that reflect radiation from objects at higher temperatures.

3.1. One-Dimensional Photonic Crystals (Distributed Bragg Reflector)

The most basic photonic crystals are one-dimensional photonic crystals (1D-PhCs) also known as one-dimensional multilayer structures. These structures are formed by stacking slabs of dielectric constant ϵ_i along a single direction and in the plane that is perpendicular to stacking direction the dielectric function does not vary. Starting from this structure, first we will study transmission and reflection properties of electromagnetic radiation analytically.

A multilayer structure (1D-PhC) consists of alternating layers with thickness d_i, dielectric constant ϵ_i and magnetic permeability μ_i is shown in Fig 3.2. The layers stacked along $z-$direction satisfying $d_i + d_{i+1} = a$ where a is the lattice constant. To calculate

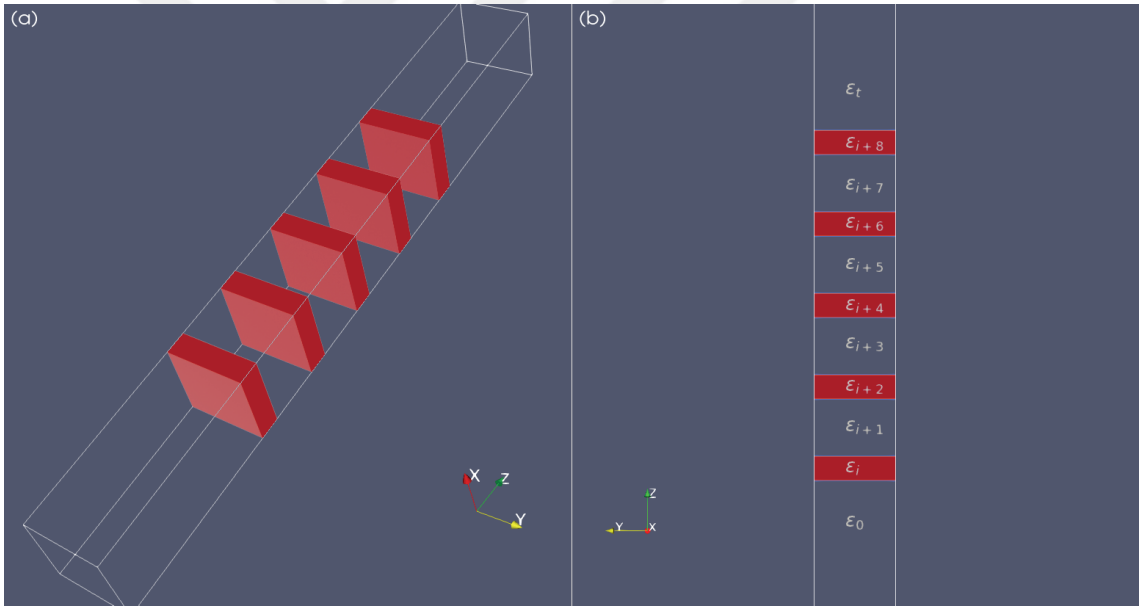


Figure 3.2. One-dimensional multi-layer structure, or one-dimensional photonic crystal. (a) 3D view. (b) 2D view.

transmission and reflection values, we start with transfer matrix which is defined as

$$M_i = \begin{bmatrix} \cos(q_i d_i) & \frac{i}{\sqrt{\frac{\epsilon_i}{\mu_i}\left(1-\frac{\beta^2 c^2}{\epsilon_i \mu_i \omega^2}\right)}} \sin(q_i d_i) \\ i\sqrt{\frac{\epsilon_i}{\mu_i}\left(1-\frac{\beta^2 c^2}{\epsilon_i \mu_i \omega^2}\right)} \sin(q_i d_i) & \cos(q_i d_i) \end{bmatrix} \tag{3.1}$$

where $q_i = \sqrt{\epsilon_i \mu_i}\frac{\omega}{c}\sqrt{1-\frac{\beta^2 c^2}{\epsilon_i \mu_i \omega^2}}$, $\beta = K_i \sin(\theta_i)$, and $K_i^2 = \beta^2 + q_i^2$. For an electromagnetic wave incident at normal incidence , $\theta_i = 0$ than $\beta = 0$ and $q_i = \sqrt{\epsilon_i \mu_i}\omega/c$. Plugging these into Eq. 3.1 than the transfer matrix becomes

$$M_i = \begin{bmatrix} \cos(\sqrt{\epsilon_i \mu_i}\omega d_i/c) & \frac{i}{\sqrt{\frac{\epsilon_i}{\mu_i}}} \sin(\sqrt{\epsilon_i \mu_i}\omega d_i/c) \\ i\sqrt{\frac{\epsilon_i}{\mu_i}} \sin(\sqrt{\epsilon_i \mu_i}\omega d_i/c) & \cos(\sqrt{\epsilon_i \mu_i}\omega d_i/c) \end{bmatrix} \tag{3.2}$$

For a structure consisting of N-pairs, the transfer matrix takes the form of

$$M = M_1 M_2 M_3 \cdots M_N = \begin{bmatrix} M_{11} & M_{12} \\ M_{21} & M_{22} \end{bmatrix} \tag{3.3}$$

then for a multi-layer structure immersed in air background, transmission coefficient is defined as

$$T = \left| \frac{2n_0}{n_0 M_{11} + n_0 n_t M_{12} + M_{21} + n_t M_{22}} \right|^2 \tag{3.4}$$

where $n_0 = \sqrt{\epsilon_0}$ is the refractive index of the incident medium that electromagnetic field is coming from and $n_t = \sqrt{\epsilon_t}$ is the refractive index of the transmitted medium. Reflection coefficient is defined as

$$R = \left| \frac{n_0 M_{11} + n_0 n_t M_{12} - M_{21} - n_t M_{22}}{n_0 M_{11} + n_0 n_t M_{12} + M_{21} + n_t M_{22}} \right|^2 \tag{3.5}$$

Now consider a non-magnetic ($\mu_a = 1.0$, $\mu_b = 1.0$) structure with alternating dielectric mediums, ϵ_a and ϵ_b with thicknesses d_a and d_b satisfying relation $d_a + d_b = a$ so that these two mediums makes a unit cell with lattice constant a, which we refer it as a pair. The multi-layer structure is immersed in air background where the incident and transmitted field medium are also taken to be air, ϵ_0 and ϵ_t.

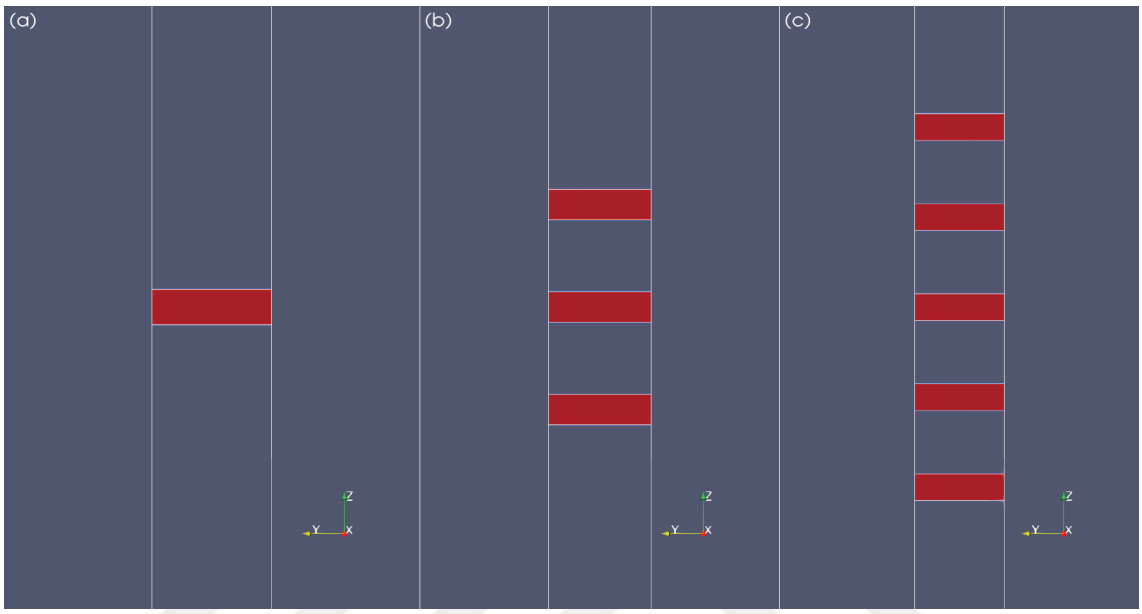


Figure 3.3. One-dimensional multi-layer structure, or one-dimensional photonic crystal. (a) One unit cell. (b) Three unit cell. (c) Five unit cell.

For minimum transmission (or maximum reflection), the thickness of layers must meet the quarter-wave stack condition, $d_a = a\sqrt{\epsilon_b}/(\sqrt{\epsilon_a} + \sqrt{\epsilon_b})$. The photonic band gap (PBG) for normal incidence is maximized for this value.

Using the transfer matrix (TM) method, the transmission and reflection spectrum for single-pair, three-, and five-pairs are calculated. The results are shown in Fig. 3.4. The calculations are performed with a dielectric constant $\epsilon_a = 5.38$ and the structure is immersed in an air background ($\epsilon_b = 1.0$). A homogeneous plate with a thickness that satisfies the quarter-wave condition $d_a = 0.30a$ is used.

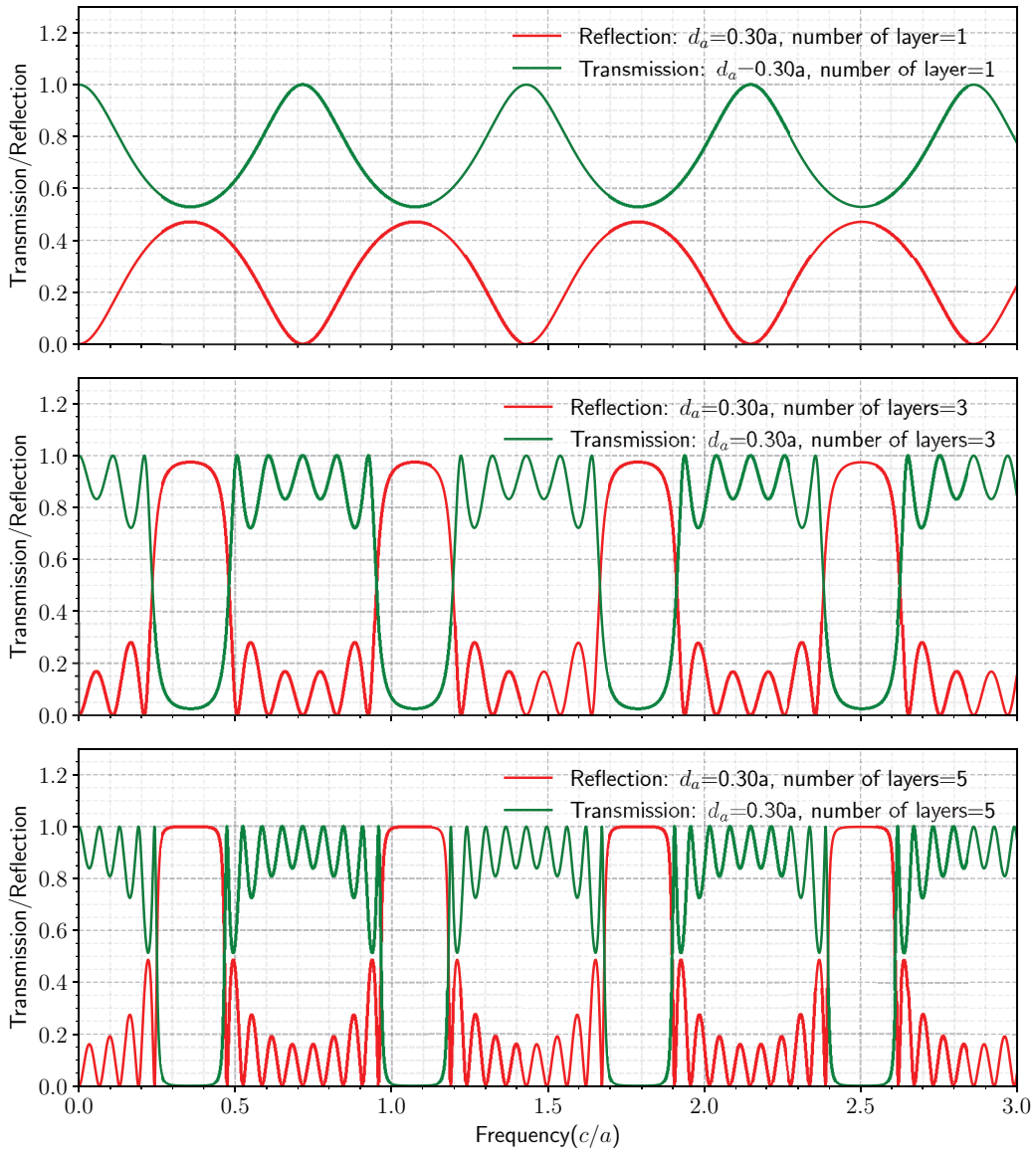


Figure 3.4. Transmission (green curves) and reflection (red curves) spectrum for single-layer, three- and five-layers, with thickness of $d_a = 0.30a$ and dielectric constant $\epsilon_a = 5.38$ immersed in air background, $\epsilon_b = 1.0$.

Our goal is to develop a structure that can be used to reduce the transmission of blackbody radiation, so the most basic structure is a good place to start. It has been shown that by using one-dimensional photonic crystal, we can suppress electromagnetic radiation (blackbody radiation) (Cornelius and Dowling, 1999). Although an analytical solution exists for those simple structures, we will use the finite-difference time-domain (FDTD) method by using a program called MEEP to calculate the transmission spectrum.

The structure we use for FDTD calculation is shown in Fig. 3.5. A homogeneous plate of thickness d_a and dielectric constant $\epsilon_a = 5.38$ is immersed in air background of thickness $d_b = a - d_a$ and dielectric constant $\epsilon_b = 1.0$. In $x - y$ direction we used periodic boundary conditions (PBC) while in $z-$direction we used perfectly matched layer (PML) to create illusion of infinite extent. To excite the electromagnetic field, we used a two-dimensional Gaussian-profiled plane wave source, which is placed at one side of the structure. Then, for calculation of transmitted flux, we placed a monitor to capture transmitted flux.

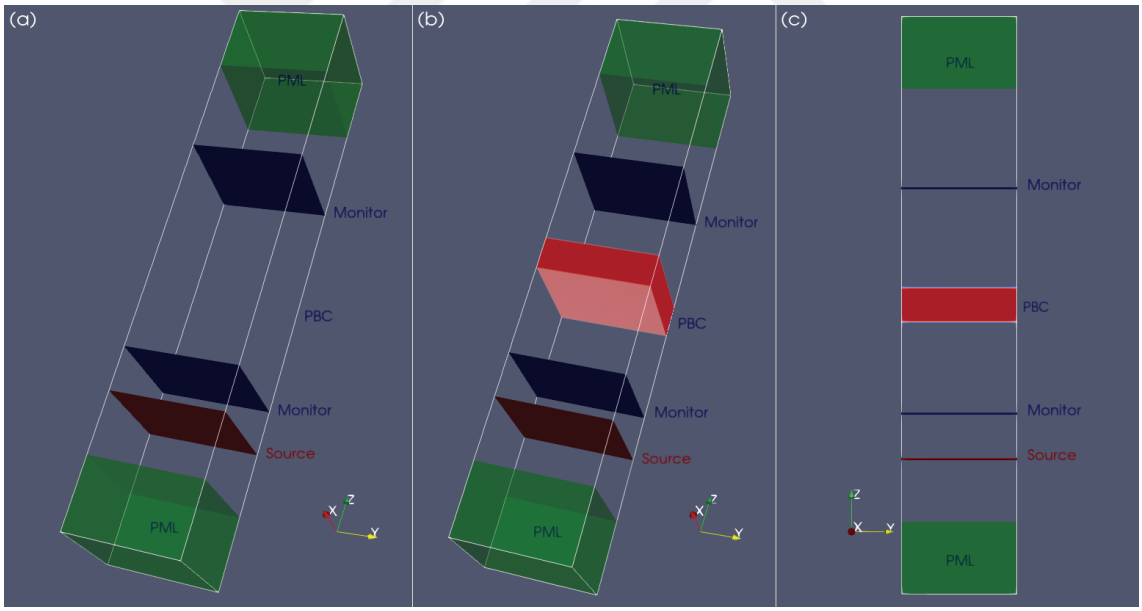


Figure 3.5. FDTD Simulation setup of a single homogeneous plate immersed in air background for transmission calculation.

The calculation involves monitoring the fields' Fourier transforms at the location where we set up monitor and computing the flux of electromagnetic energy as a function of frequency. For convergence of Fourier transform the simulation time must be long enough.

By Fourier transforming the response to a short pulse we can get an entire spectrum of the transmission in a single run. But we still must perform two runs, one with and one without the structure in order to normalize the transmitted flux by the input power.

The unit cell of the structure is $V_{cell} = a_x a_y a_z$ where $a_x = a_y = a_z = a$ and the computational volume is defined as $V_{comp} = S_x \times S_y \times S_z$, where S_x, S_y and S_z are defined as $S_x = a_x$, $S_y = a_y$ and $S_z = 2dpml + 2dpad + n_z a_z$. Here $dpml$ is the thickness of the PML region $dpad$ is distance between PML region and the structure and n_z is the number of unit cell along $z-$direction and a is lattice constant.

This simulation setup will be used in this and in all subsequent sections for the calculation of transmission. The only difference will be the structure we put in the computational volume.

The first FDTD simulation setup for single, three and five unit cell along $z-$direction is shown in Fig.3.6

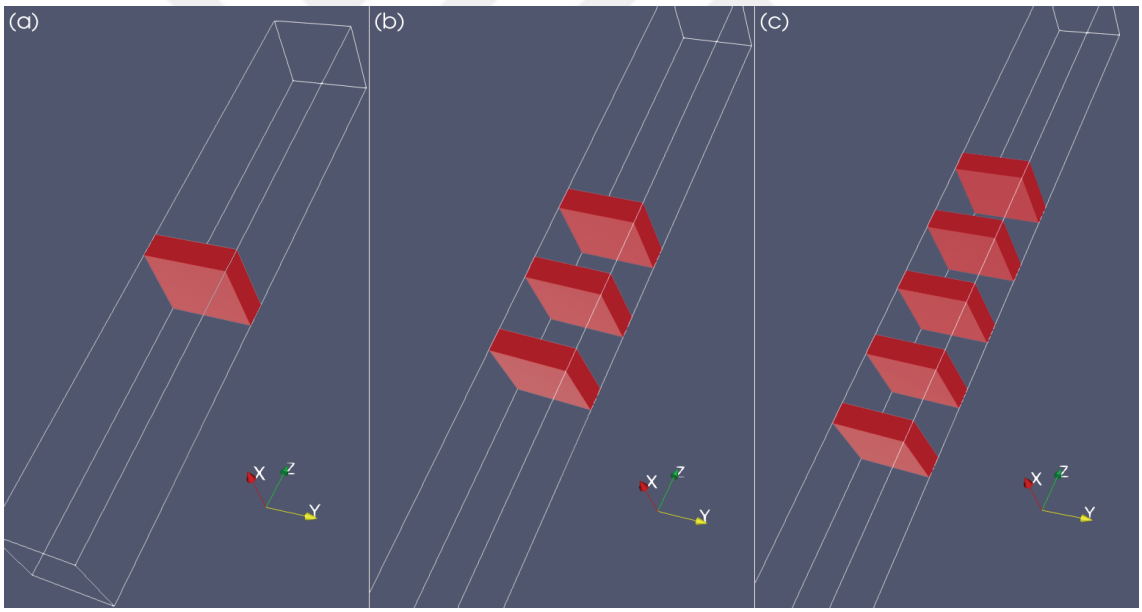


Figure 3.6. FDTD simulation setup of a single (a), three (b), and five (c) unit cells of a homogeneous plate immersed in air for transmission calculation.

A Gaussian profiled plain wave source with center frequency of $\tilde{\omega} = 1.60$ having bandwidth $\Delta\tilde{\omega} = 3.0$ where $\tilde{\omega}$ is in units of $\omega a/2\pi c$ is use to excite $x-$component of the electric field. The transmission spectrum of a plate with thickness of $d_a = 0.30a$ which is calculated using the quarter-wave stack condition to get minimum transmission, is shown in Fig. 3.7.

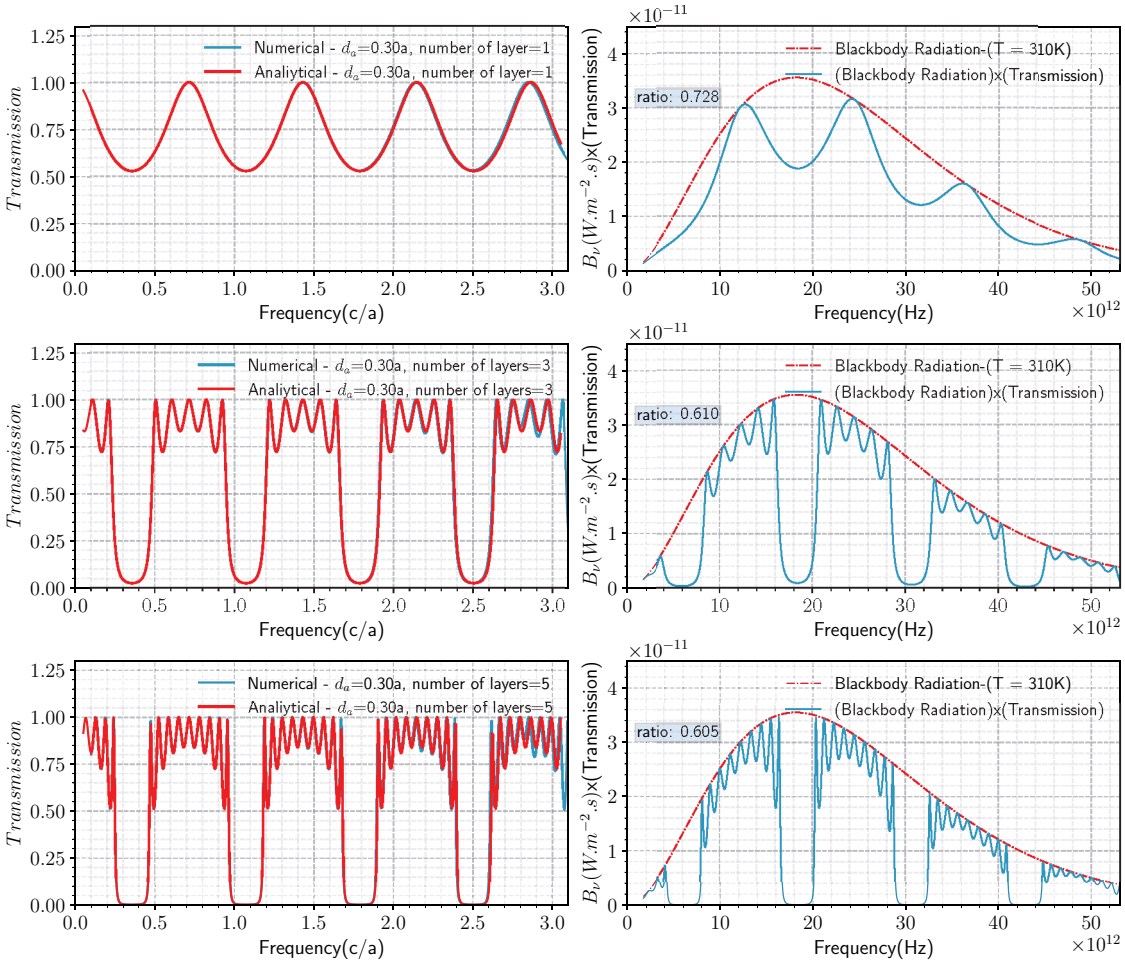


Figure 3.7. Left colum: Transmission spectrum for single layer, three, and five layers (solid red curves are for analytical solutions and solid blue curves are for numerical solutions).
Right column: Blackbody radiation spectrum (dashed red curves) and transmission values multiplied by blackbody radiation (solid blue curves).

In this graph we have plotted transmission spectrum for single layer, three, and five layers computed numerically by using MEEP (blue curve on the left column of the figure) and analytically by using the TM method (red curve on the left column of the figure), and as it is seen, the results are in excellent agreement, which validates the numerical

method we use. We also plotted blackbody radiation spectrum for an object at temperature $T = 310K$ which has peak frequency of $\nu_{peak} = 18.2THz$ (red dashed curve on the right column). Since the most of the blackbody radiation is around ν_{peak} we scale the results so that the peak frequency of blackbody falls in to center frequency of the gap and multiply the scaled values of the blackbody radiation spectrum with the transmission values (the blue curve on the right column).

By adding the areas under the spectrum curves of the structure and the blackbody radiation curve, we can determine the amount of transmitted power, which comes out to 72% for a single layer, 61% for three layers, and 60% for five layers. The results converged even with five layers because the transmitted power is logarithmically dependent on the number of layers.

3.2. Woodpile Photonic Crystals

Among the 3D-PhCs that are known in literature, topologically, the woodpile structure is the most similar to woven fabrics. The woodpile structure is made by stacking logs of dielectric materials. Along a chosen stacking direction with each period containing four layer. The logs in the first layer are placed parallel to each other and separated by a lattice constant. The second layer is placed on the first layer and is aligned perpendicularly with respect the the first layer. The logs in the third layer are placed parallel to the first layer but are shifted by half of lattice constant in $x-$ and $y-$direction. Finally the logs in the last layer are placed parallel to the second layer and are similarly shifted by half of lattice constant in the $x-$ and $y-$direction. The woodpile structure is shown

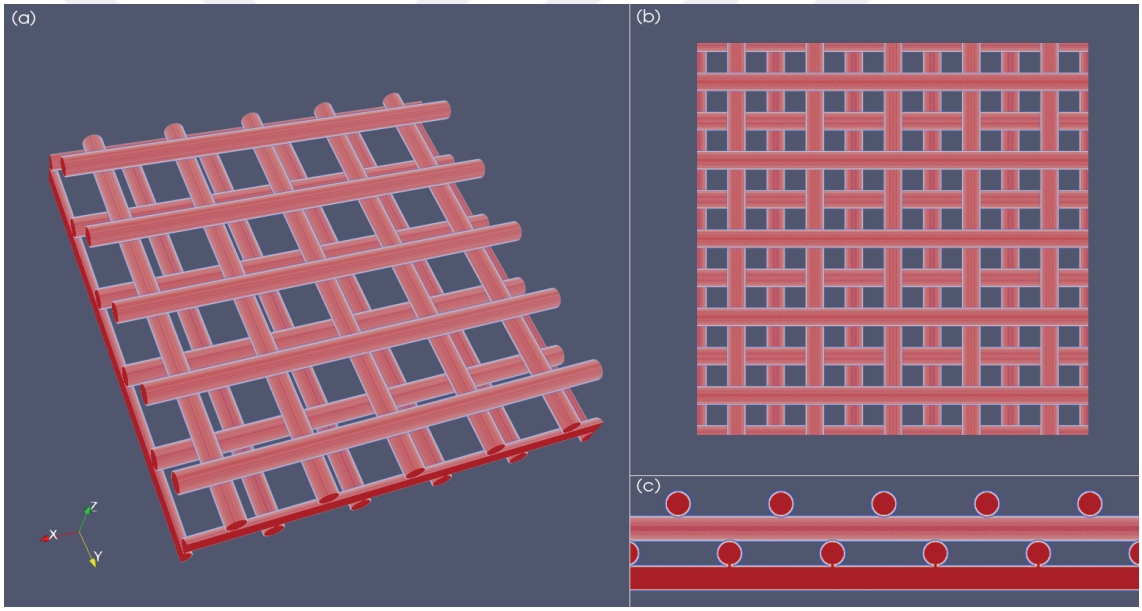


Figure 3.8. Woodpile photonic crystal structure. (a) 3D view, (b) top view and (c) side view.

in Fig. 3.8. Theoretically it was shown that woodpile structure posses full photonic band gap (Ho et al., 1994) and (Sözüer and Dowling, 1994). Experimentally, a study showed that even with a few number of periods the band gap can be observed (Lin et al., 1998).

To start with, by using finite-difference time-domain (FDTD), we calculated transmission spectrum of a woodpile structure made by cylindrical rods. The FDTD simulation setup for a single unit cell along all three dimension is shown in Fig.3.9.

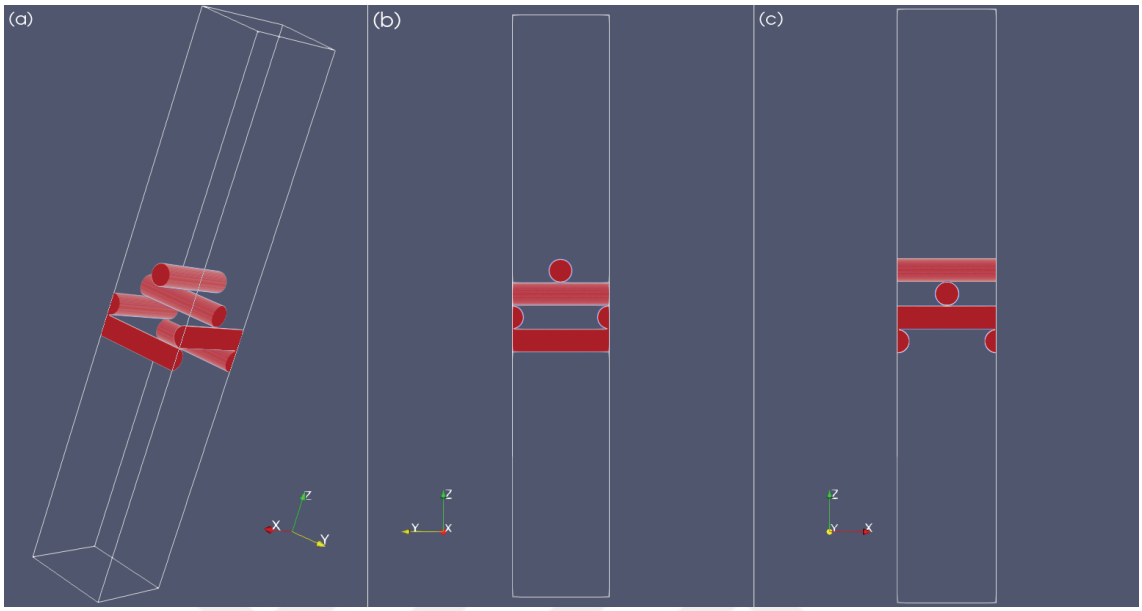


Figure 3.9. FDTD simulation setup for single unit cell of woodpile photonic crystal structure. (a) 3D view. (b)-(c) 2D view.

Cylindrical rods with dielectric constant of $\epsilon_a = 5.38$ and radius $r = 0.12a$ immersed in air background and a single period in the stacking direction is used. The simulation is done for one unit cell where the volume of a unit cell for woodpile structure is defined by $V_{cell} = a_x \times a_y \times a_z$. The lattice constants are $a_x = a_y = a$ and $a_z = 8r$. The computational volume is defined as $V_{comp} = S_x S_y S_z$ where $S_x = a_x$, $S_y = a_y$, and $S_z = 2dpml + 2dpad + a_z$. Here, $dpml$ is the thickness of the PML region, and $dpad$ is the distance between the PML region and the structure. As boundary conditions, PBC in the $x - y$ direction and PML in the $z-$direction are used.

A short Gaussian profiled plane wave source with center frequency $\tilde{\omega} = 1.60$ and bandwidth $\Delta\tilde{\omega} = 3.0$ is used to excite x-component of electric field. On the opposite side of the structure we placed a flux monitor that captures transmitted flux. For normalization we run simulation twice, one without and one with structure in the computational region.

The transmission spectrum (blue curve) of the woodpile structure is shown in Fig. 3.10. The center frequency of the band gap for this structure is around $\tilde{\omega} = 0.72$. In the bottom graph, we plotted the blackbady radiation spectrum (red curve) at temperature of $T = 310K$ with a peak frequency $\nu_{peak} = 18.2THz$. The green curve is the transmission values multiplied by the blackbody spectrum.

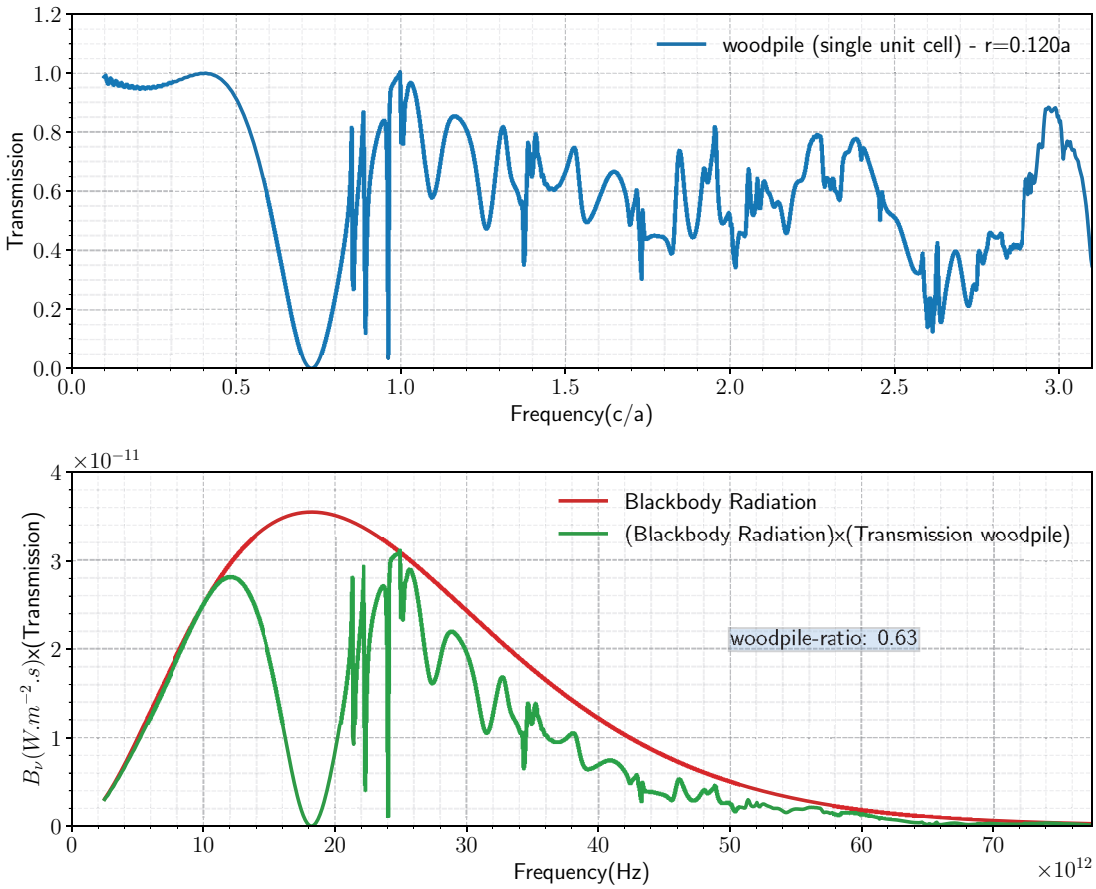


Figure 3.10. Transmission spectrum (top graph), blackbody radiation curve (bottom red curve) and the transmission spectrum multiplied by blackbody radiation curve(bottom green curve).

To find the total amount of power that is transmitted, we simply divide the areas under the curves, which is found to be 63%. It means that 37-percent of total power is reflected by just using a single unit cell of the woodpile photonic crystal structure along $z-$direciton. The structure we used here has finite thickness along $z-$direction (one unit cell) so the results are different from those having infinite extend but still give an idea about how much of energy can be blocked by using a PhC like structure.

To compare the results we have found previously with a homogeneous plate, we calculated transmission spectrum for a homogeneous plate that would occupy the same volume with woodpile structure. So the thickness plate in the $z-$direction for this condition is found to be $d_a = 0.18a$. Dielectric constant and background for in both cases are taken to be the same. With this thickness the transmission spectrum of homogeneous plate using FDTD is calculated and both results are shown in Fig. 3.11. Transmitted power for

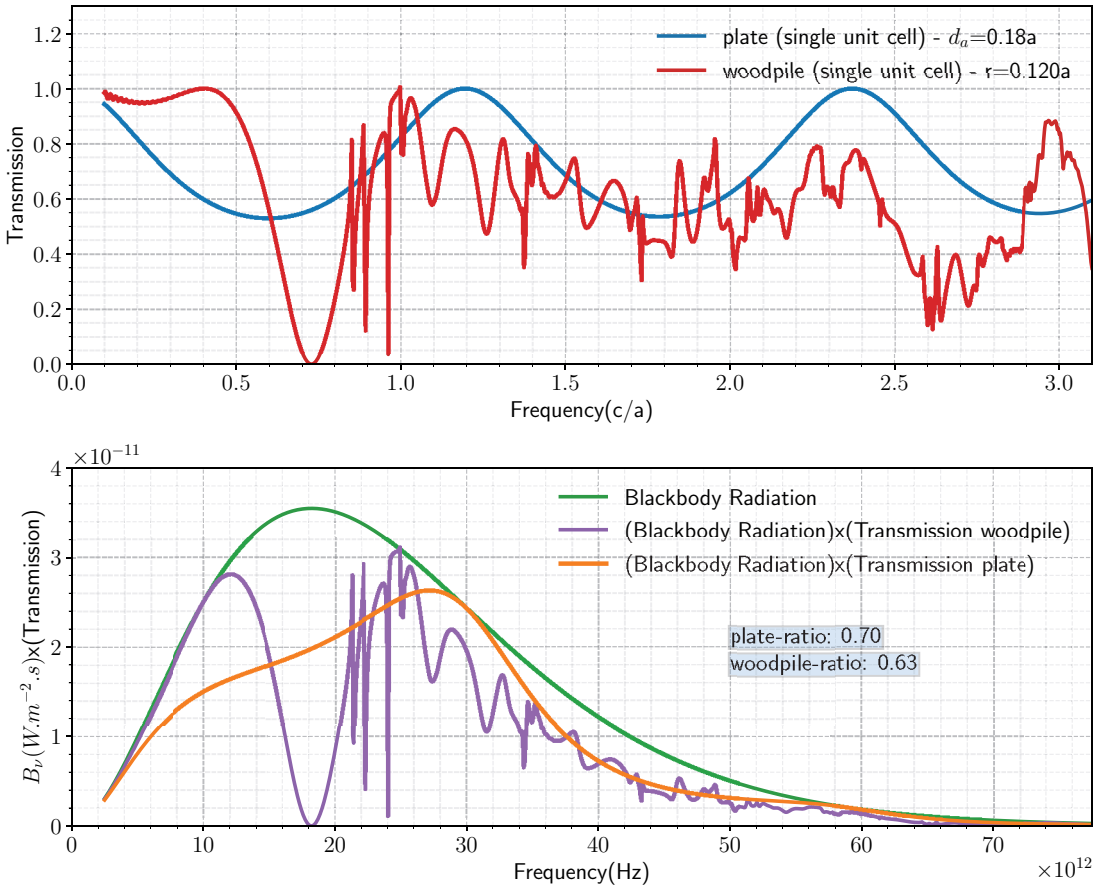


Figure 3.11. Transmission spectrum for single unit cell of woodpile structure (red curve), transmission spectrum of homogeneous plate (blue curve). Blackbody radiation spectrum (green curve) and transmission values multiplied by blackbody radiation (purple and orange curves).

homogeneous plate found to be 70% while for a single unit cell woodpile structure the transmitted power is found to be 63%. As it is seen from the transmission spectrum, even for a single period of woodpile structure, transmitted power is less by 7% so the results are promising and can further be improved.

To see the effect of number of unit cell on transmission values of woodpile structure, we now compute transmission for woodpile that composed of three period in the stacking direction.

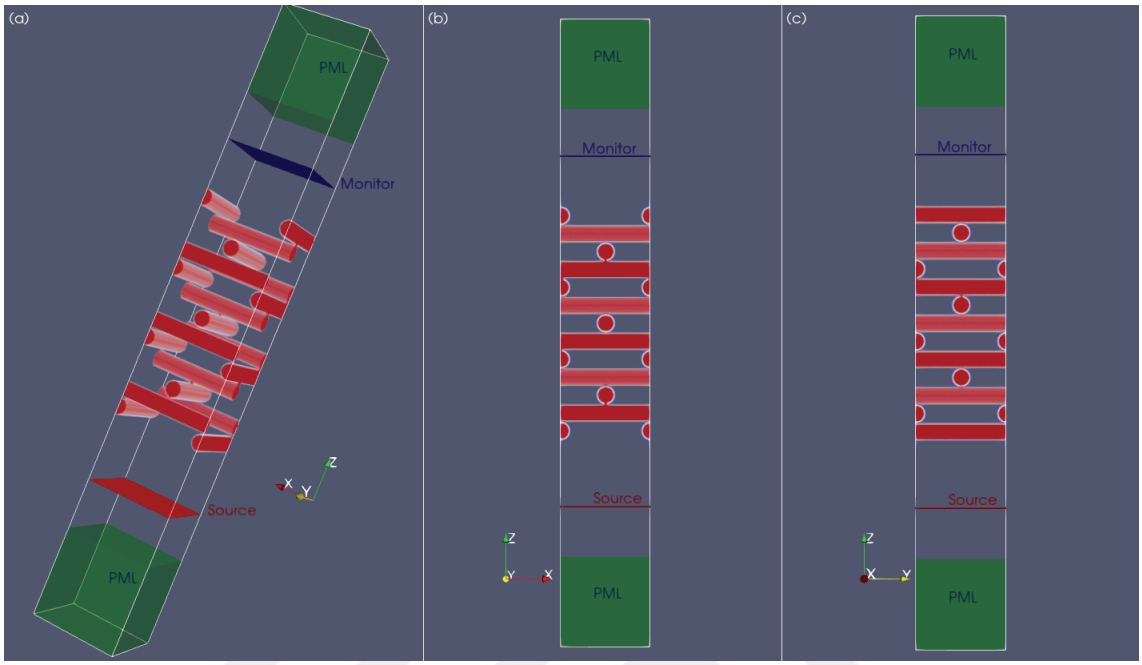


Figure 3.12. The FDTD simulation setup of bare woodpile structure with three unit cell along stacking direction ($z-$direction). (a) 3D view. (b) 2D view from $x-z$ plane. (c) 2D view from $y-z$ plane.

This structure is made adding two more unit cell while keeping other parameters the same, dielectric constant $\epsilon_a = 5.38$ and radius of cylinders $r = 0.120a$. The resulting structure and FDTD simulation setup is shown in Fig. 3.12. Computational volume for this structure is $V_{comp} = S_x S_y S_z$ where $S_x = S_y = a_x = a_y = a$, and $S_z = 2dpml + 2dpad + 26r$.

In the Fig. 3.13 we plotted the transmission spectrum as a function of frequency. The center frequency of the stop band did not change but the gap is bigger compared to the single unit cell as expected.

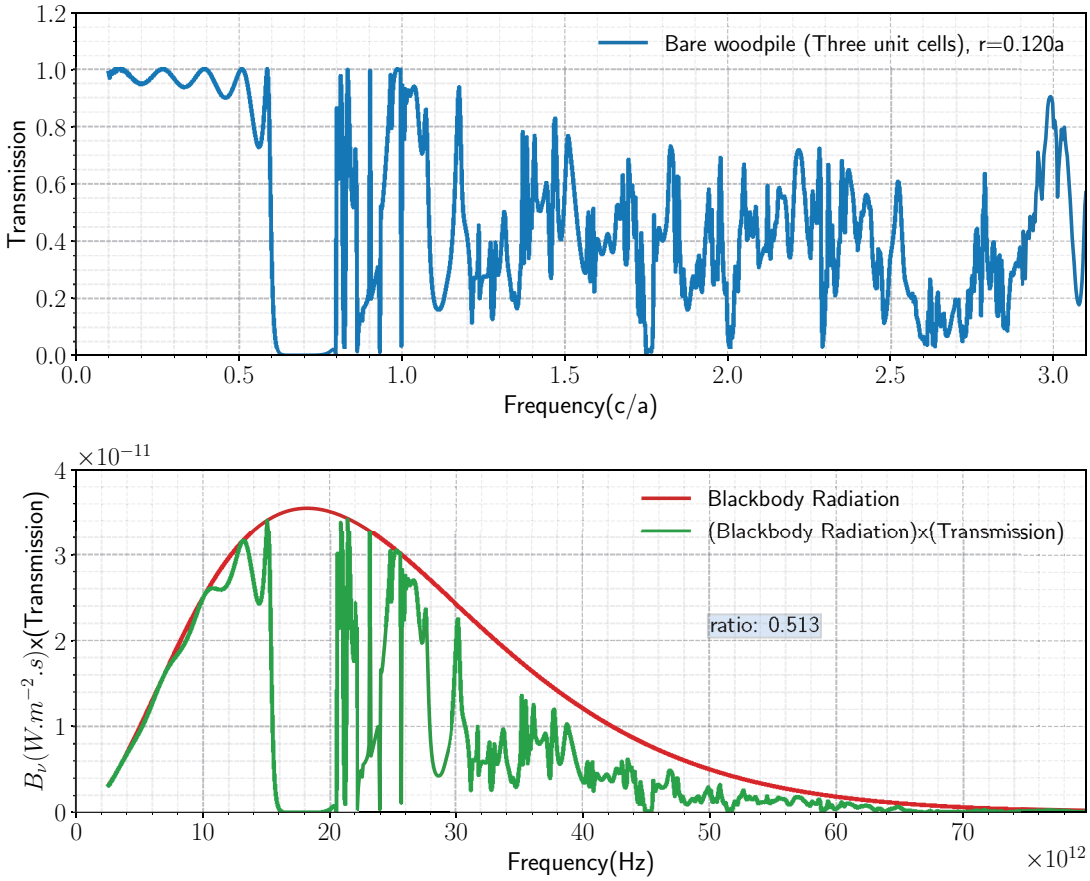


Figure 3.13. Transmission spectrum for connected woodpile structure (blue curve). Blackbody radiation spectrum (red curve) and transmission values multiplied by blackbody radiation (green curve)

The amount of power that is transmitted is 51%, which means around half of total energy is reflected. Compared to the woodpile composed of single unit cell, we obtain a 12% lower value, which was found to be 63%.

We are looking for a structure that can be woven into fabric while preserving the PhC's ability to provide maximum reflection. In practice, woodpile structure built in this manner are unsuitable for use as woven fabrics. As a result, we must link each layer such that it remains firm. One method is to connect each layer to the one next to it using smaller-radius yarns. The thinner yarns are chosen so that they do not affect the structure's photonic band gap (PBG). The resulting structure as well as the FDTD simulation setup are shown in the Fig. 3.14.

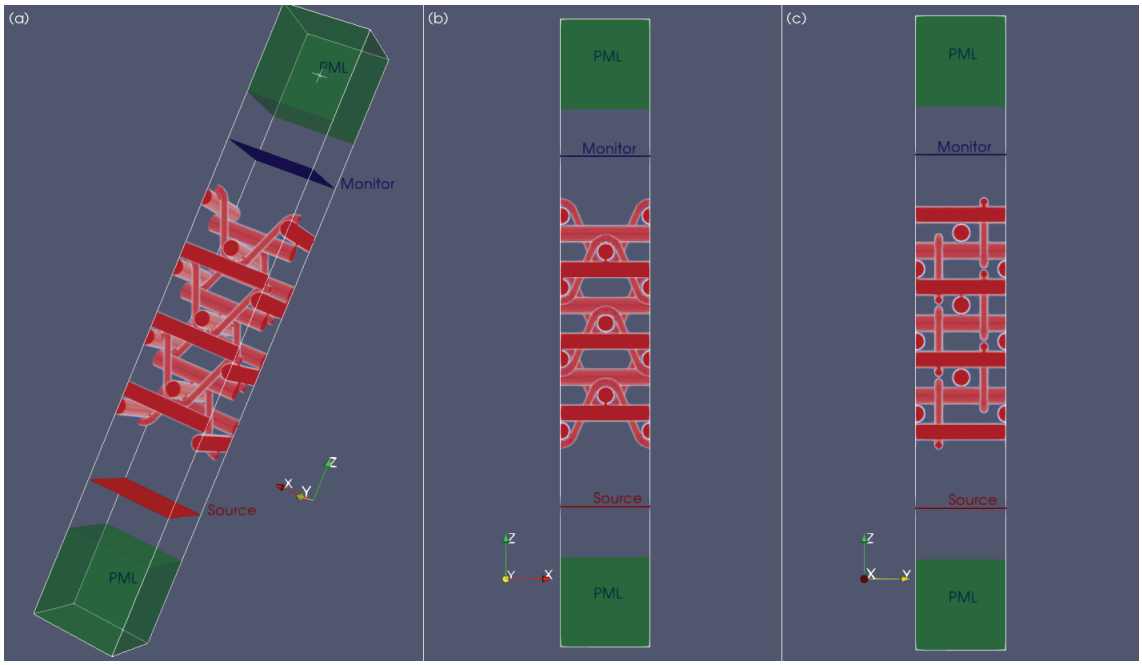


Figure 3.14. The FDTD simulation setup of connected woodpile structure with three unit cell along stacking direction ($z-$direction). (a) 3D view. (b) 2D view from $x-z$ plane. (c) 2D view from $y-z$ plane.

The parameters for this simulation such as yarn radius and dielectric constant, number of unit cells along $z-$direction, background are all the same except the connection lines. The connecting yarn radius are taken to be $r_c = r/4$. There are two degrees of freedom in the problem for optimizing structure. The first one is the radius and the second one is the dielectric constant of the structure. For this structure, keeping the dielectric constant the same, we calculated transmission values by changing the radius of cylinders, from $0.060a$ to $0.180a$ in steps of $0.010a$.

The first result we show here is for yarn radius of $r = 0.120a$. Transmission spectrum for connected woodpile structure (blue curve) is shown in Fig. 3.15. The center frequency of the band gap appears to be around $\tilde{\omega_0} = 0.72$, same as the original woodpile band gap. By shifting the center frequency of the stop band to the peak value of the blackbody radiation (red curve) then multiply the transmission values, which is a dimensionless quantity, by the blackbody spectrum we obtained transmitted power spectrum of the structure (green curve).

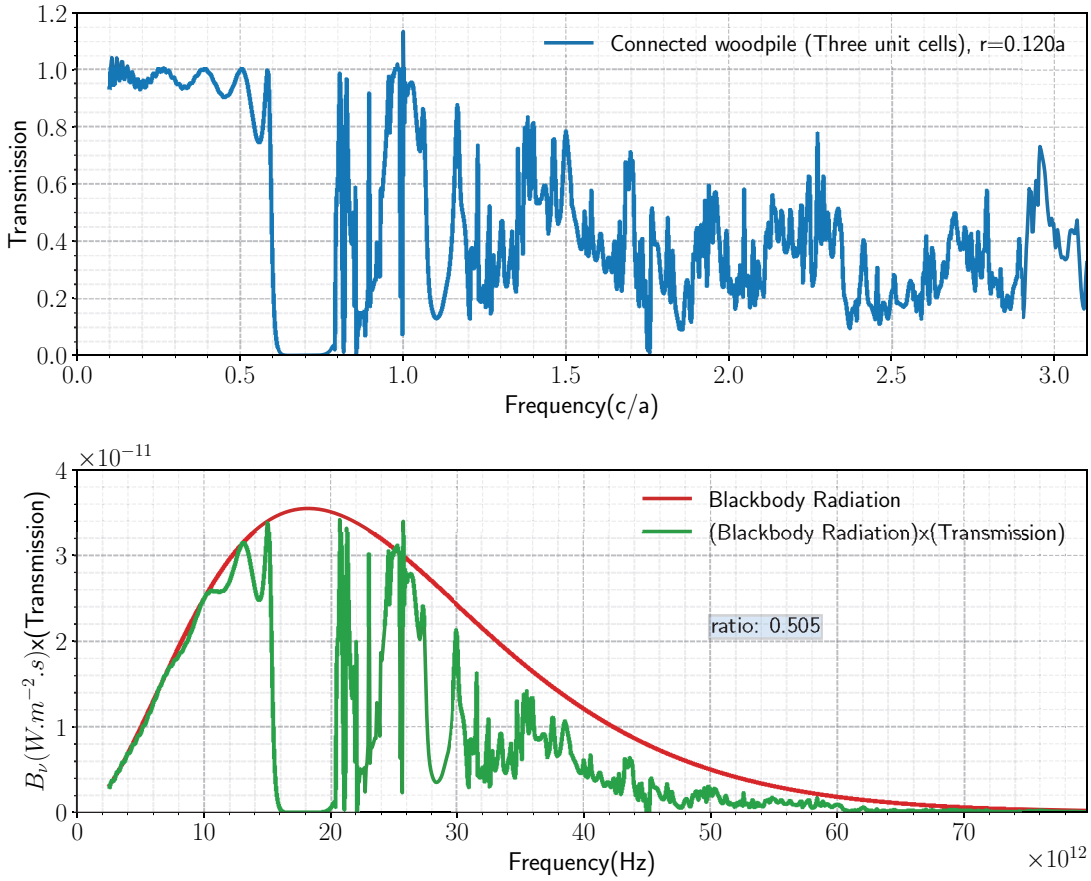


Figure 3.15. Transmission spectrum for connected woodpile structure (blue curve). Blackbody radiation spectrum (red curve) and transmission values multiplied by blackbody radiation (green curve)

As expected, the transmitted power is 50%, which is quite close to the value for the bare woodpile structure that we used in the previous calculation.

One of the best results is found for a yarn radius of $r = 0.140a$ which is shown in Fig. 3.16. Blue curve is the transmission spectrum, red curve is blackbody radiation spectrum and green curve is transmission spectrum multiplied by blackbody radiation. Center frequency of this structure is $\tilde{\omega} = 0.65$. Scaling this frequency so that it coincides

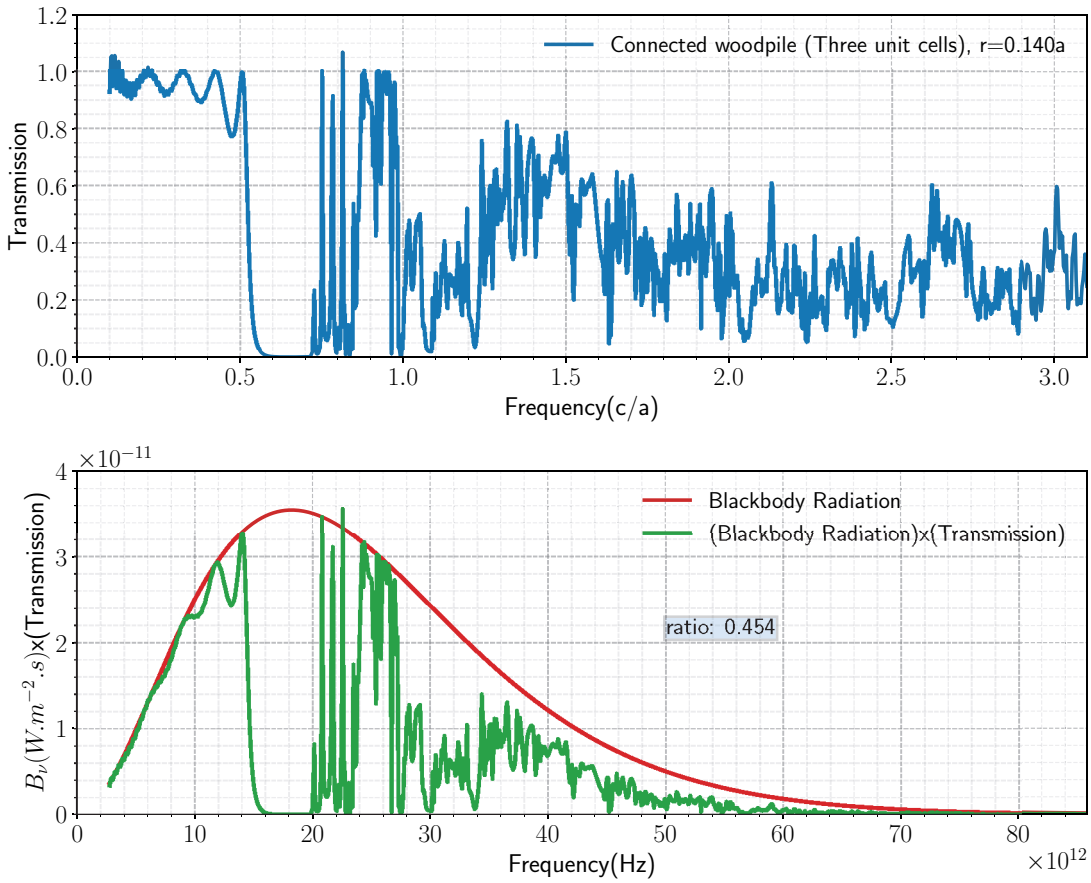


Figure 3.16. Transmission spectrum for connected woodpile structure (blue curve). Blackbody radiation spectrum (red curve) and transmission values multiplied by blackbody radiation (green curve).

with the peak frequency of the blackbody radiation and taking the ratio of the total area under the green curve with red curve we found that the amount of transmitted power for this structure is 45%.

The rest of the transmitted power percentage and yarn radius of $0.060a \leq r \leq 0.180a$ for the bare woodpile structure and the connected woodpile structure is shown in Table. 3.1. The calculations are done using the same dielectric constant $\epsilon_a = 5.38$ and three unit cells along the stacking direction for both the bare and connected woodpile structures. The Fig. 3.17 shows the transmitted power versus yarn radius for bare and

Table 3.1. Transmitted power for woodpile photonic crystal with changing yarn radius.

Radius (r)	Bare woodpile (%)	Connected Woodpile (%)
$0.060a$	58	58
$0.070a$	59	59
$0.080a$	61	61
$0.090a$	63	63
$0.100a$	63	62
$0.110a$	57	56
$0.120a$	51	50
$0.130a$	48	48
$0.140a$	45	45
$0.150a$	44	45
$0.160a$	44	45
$0.170a$	45	46
$0.180a$	48	50

connected woodpile structure. The blue curve is for the bare woodpile while the red-

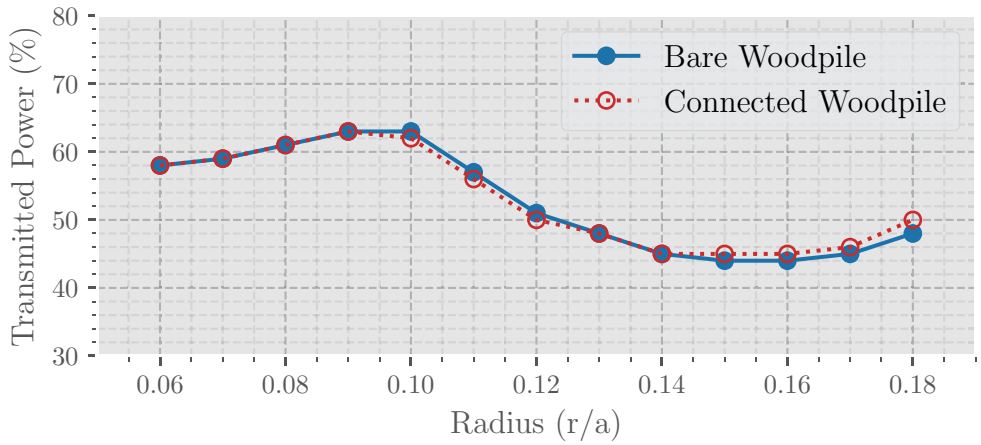


Figure 3.17. Transmitted power versus yarn radius for bare and connected woodpile structure.

dashed curve is for the connected woodpile structure. Clearly, the connecting yarns do not affect the transmitted power percentage by much.

3.3. Three-Dimensional Woven Photonic Crystals

In order to weave a fabric, two sets of yarn must be interlaced so that they cross one another. The weft threads horizontally weave over and under the warp threads while the warp threads move vertically. By repeating this process a periodic structure is constructed which can be considered as 3-dimensional photonic crystal. There are numerous different types of fabric weave patterns. The most common weave patterns used in the textile industry are plain weave, basket weave, twill weave, satin weave, and dutch weave... etc. When choosing the best foundation substrate for shielding electromagnetic radiation emitted by the human body, it's crucial to take into account the thickness, dielectric properties, and weave pattern. In this study we mainly focused on the thickness and weave patterns while keeping the dielectric constant the same for all simulation. In this thesis four different weave patterns, the plain weave, the basket weave, the twill weave, and the dutch weave are considered. are studied.

The patterns modeled by FDTD simulation program (MEEP) is shown in Fig. 3.18. In addition to those four weave patterns, we created five additional unique weave patterns

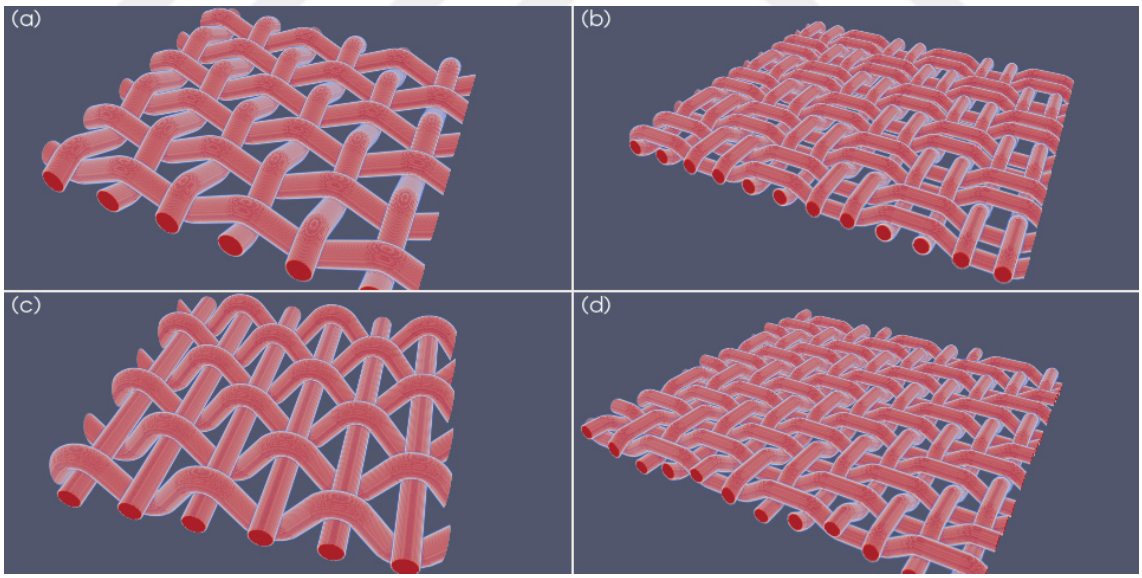


Figure 3.18. The most common weave patterns. (a) Plain Weve. (b) Basket Weave. (c) Dutch Weave. (d) Twill weave.

based on their original designs. The modification strategy was based on the fact that their

structure would be close to the woodpile photonic crystal. All five modified structures are shown in Fig. 3.19. Modified plain weave, modified basket weave and modified twill weave contains two layers of the original weave patterns in a single unit cell in the stacking direction and shifted by a quarter of unit cell along the $x-$ and $y-$directions with respect the one another. However, modification for dutch weave is different. For exam-

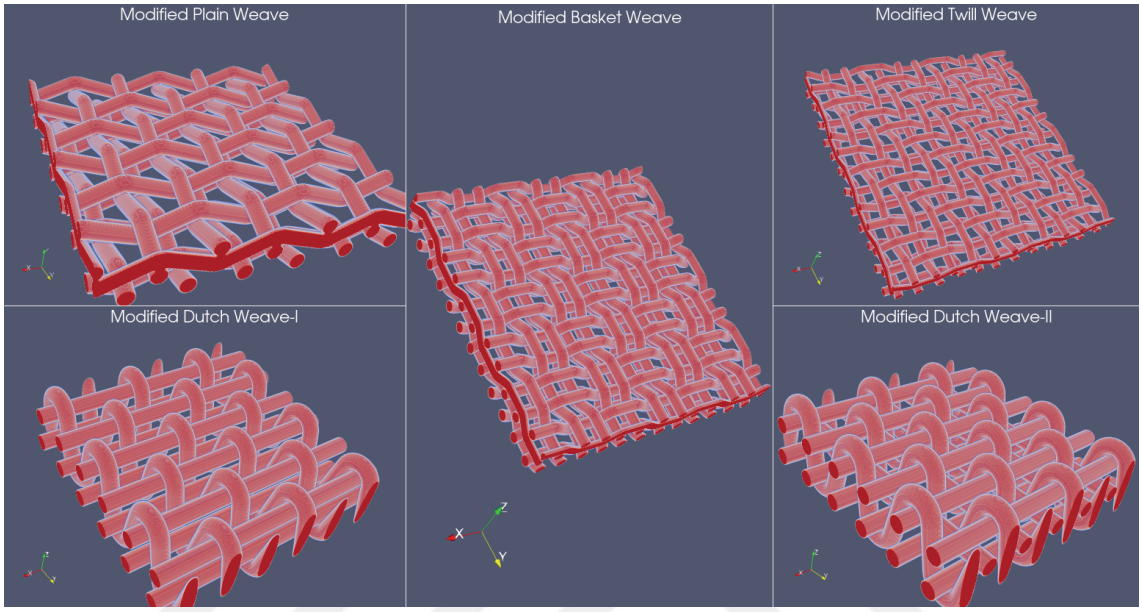


Figure 3.19. Modified weave patterns. Modified plain weave, Modified basket weave. Modified twill weave and two variation for Dutch Weave (Modified dutch weave-I and Modified dutch weave-II).

ple, modified dutch weave-I is made by connecting two straight yarns extending along $x-$direction and separated by a distance. Although this structure is not suitable for weaving because the straight yarns that are parallel to each other are suspended in the air, it can be used as a comparison and gives an idea about the other two dutch weave patterns. The modified dutch weave-II is made by adding an extra straight yarn along $y-$direction which is suitable for weaving.

3.3.1. Plain Weave

Plain weave structure from three different viewing angles is shown in Fig. 3.20. 3D view Fig. 3.20(a), top view Fig. 3.20(b) and side view Fig. 3.20(c). The FDTD simula-

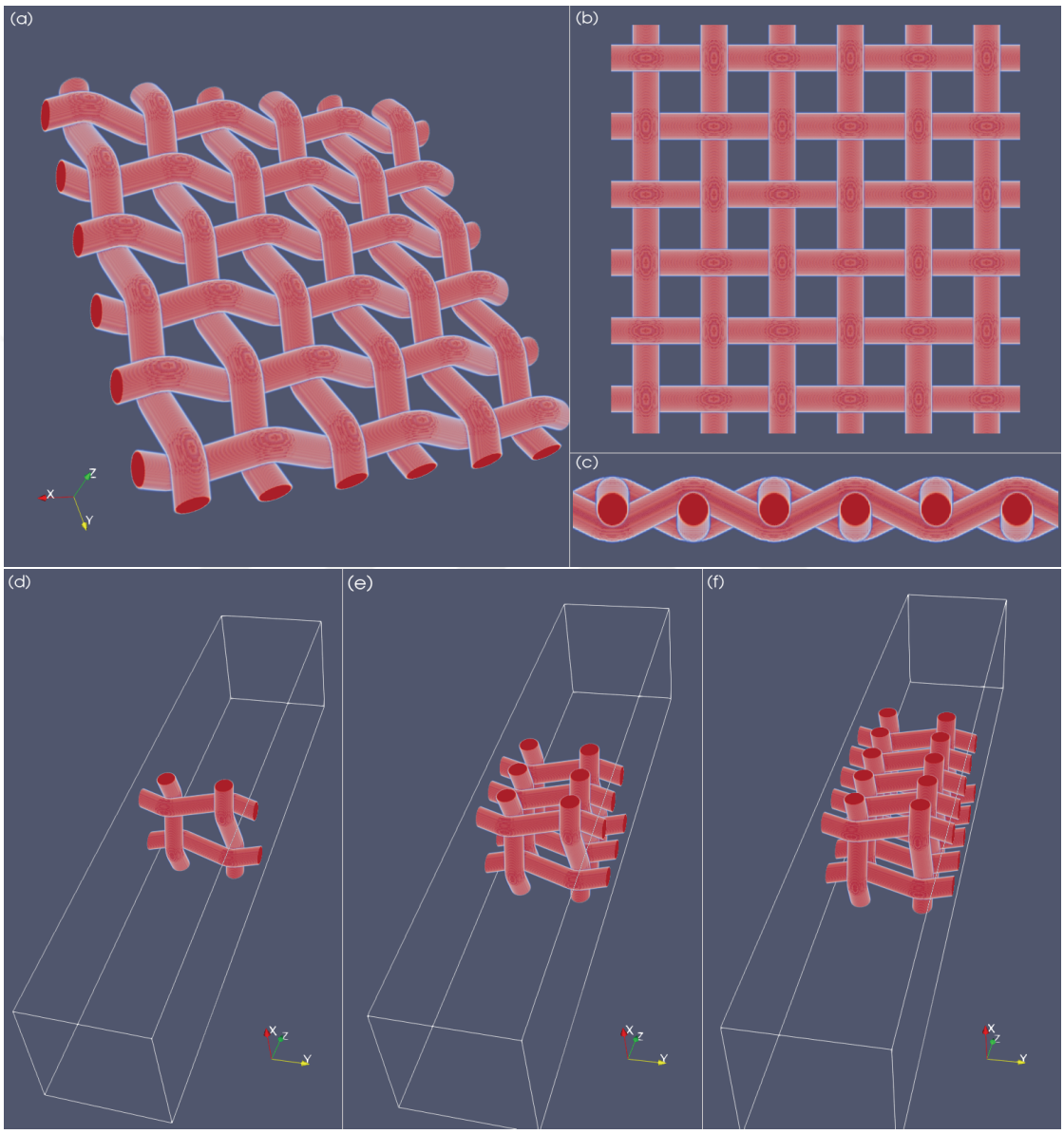


Figure 3.20. Plain weave structure, 3D view (a), top view (b) and side view (c). FDTD simulation setup, single unit cell (d), three unit cells (e), and five unit cells (f) in $z-$direction.

tion setup for calculation of transmission spectrum for one unit cell (d), three (e) and five (f) unit cells is shown in Fig. 3.20. In the $x-$ and $y-$directions periodic boundary condi-

tions (PBC) and in the $z-$direction perfectly matched layer (PML) are used as boundary conditions. The volume of a unit cell is defined as $V_{cell} = a_x a_y a_z$ where $a_x = a_y = a$ and $a_z = 4r$. The volume of FDTD simulation is defined by $V_{comp} = S_x S_y S_z$ where $S_x = S_y = a$ and $S_z = 2dpml + 2dpad + n_z a_z$ where $dpml$ is the thickness of the PML region, $dpad$ is the distance between the PML region and the structure and n_z is the number of unit cell along the $z-$direction.

For FDTD simulation calculations, the structure made of yarns with a dielectric constant $\epsilon_a = 5.38$ immersed in an air background ($\epsilon_b = 1.0$) is used. As a source, a Gaussian-profiled plane wave is used to excite the $x-$component of the electric field from the negative $z-$direction. The source's center frequency is taken to be $\tilde{\omega} = 1.60$ and the frequency bandwidth of the pulse is $\Delta\tilde{\omega} = 3.0$. A monitor is placed in the positive $z-$direction to calculate electromagnetic flux.

The FDTD calculation gives transmission versus frequency, both are dimensionless quantity. So to find the radiation spectrum of a structure, we first scale the blackbody radiation spectrum so that its peak frequency, $\nu_{peak} = 18.22THz$, coincides with the frequency of the stop band of the structure. And then we multiply the transmission spectrum of structure with blackbody radiation.

Minimum transmitted power are found for yarn radius of $0.06a$ and $0.07a$. The first transmission spectrum shown in Fig. 3.21 is for the yarn radius of $r = 0.06a$. In this graph the left column represents the normalized flux for single , three and five unit cells. On the right column, we plotted blackbody radiation for temperature $T = 310K$(red dashed curve) and transmission values multiplied by blackbody radiation spectrum (the blue curves on the right column) for single unit cell, three unit cells, and five unit cells along $z-$direction. The amount of power transmitted for single unit cell is 73%, three and

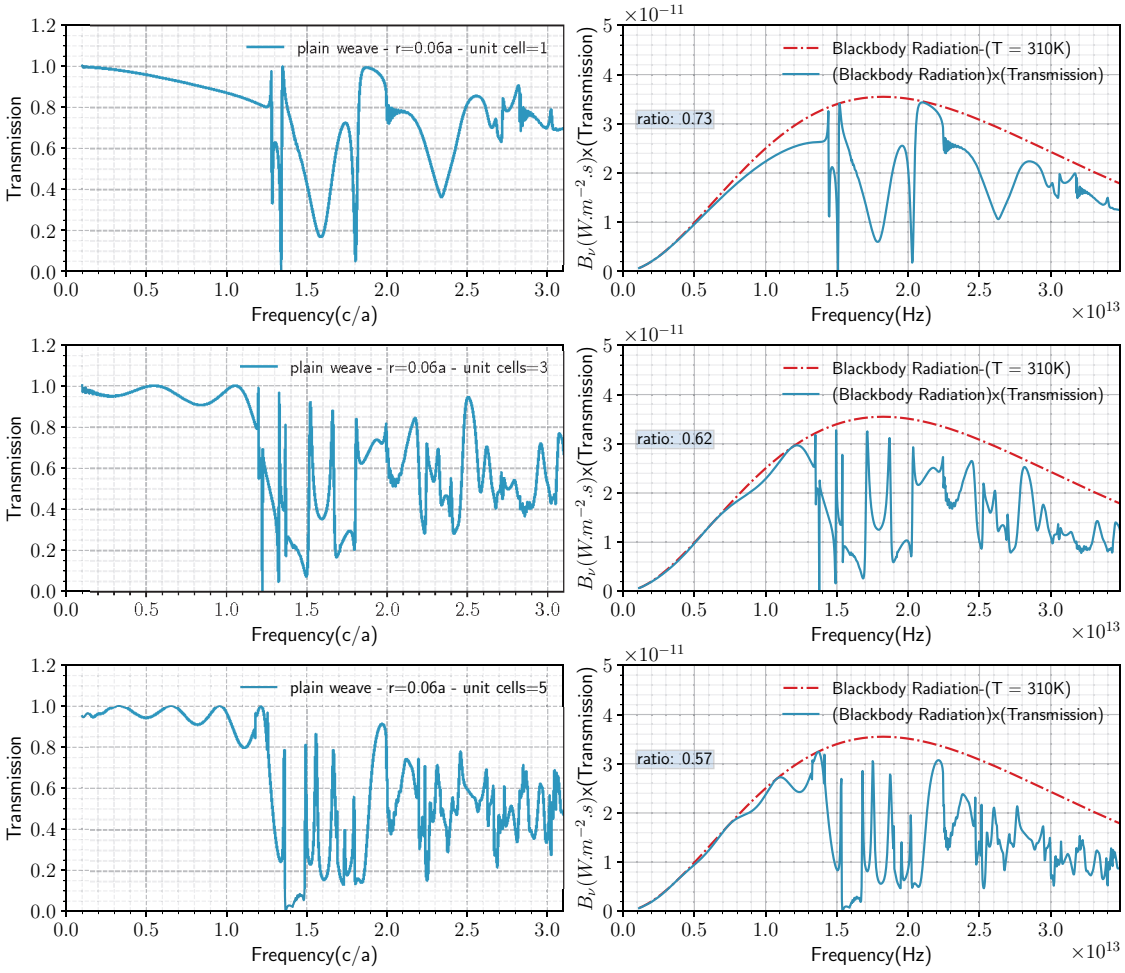


Figure 3.21. Transmission spectrum of plain weave pattern for 1-unit cell, 3-, and 5-unit cells (left column). Blackbody radiation spectrum (red dashed curve on the right column) and blackbody spectrum multiplied by transmission values of plane weave pattern (blue curve on the right column).

five unit cells are 62% and 57% respectively.

Fig.3.22 shows the second transmission spectrum. The transmission spectra for one unit cell, three unit cells, and five unit cells with a radius of $r = 0.07a$ and dielectric constant $\epsilon_a = 5.38$ are shown in the left column, and the transmission spectra multiplied by blackbody radiation are shown in the right columns. The structure is surrounded by an air background, $\epsilon_b = 1.0$. The amount of power transmitted for single unit cell is 69%,

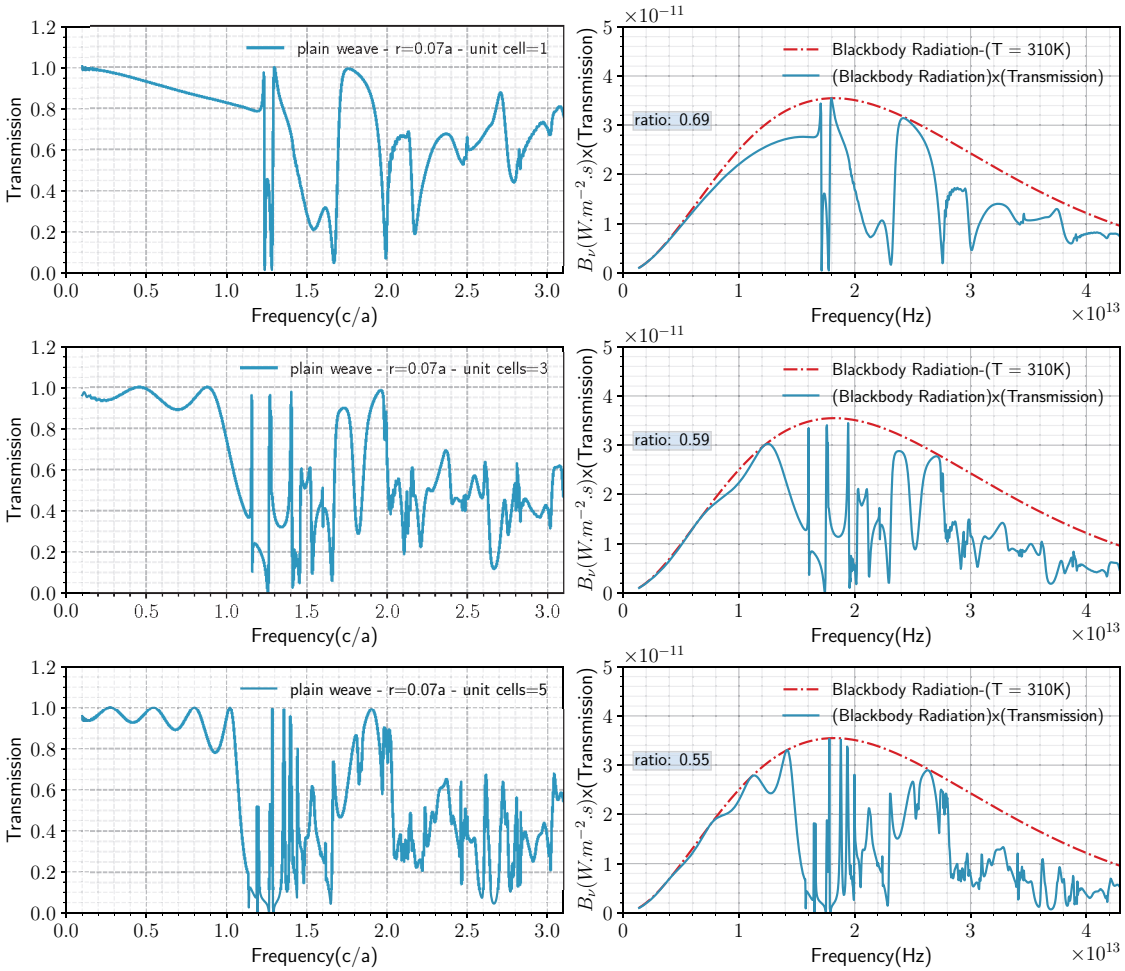


Figure 3.22. Transmission spectrum of plain weave structure for single-, three-, and five-unit cell (left column). Blackbody radiation spectrum (red dashed curve on the right column) and blackbody spectrum multiplied by transmission values of plane weave pattern (blue curve on the right column).

for three and five unit cells are 59% and 55% respectively.

Besides these two results, we also calculated the transmission spectrum for yarn radius $0.06a \leq r \leq 0.12a$ in steps of $0.01a$ and the calculated transmitted power percentage for different yarn radius is shown in Table. 3.2.. In this table, the first column is

Table 3.2. Transmitted power percentage for plain weave pattern.

Radius(r)	Single unit cell (%)	Three unit cell (%)	Five unit cell (%)
$0.06a$	73	62	57
$0.07a$	69	59	55
$0.08a$	73	64	59
$0.09a$	81	68	64
$0.10a$	85	71	66
$0.11a$	84	69	65
$0.12a$	82	69	65

the radius, the second column is the transmitted power percentage for a single unit cell, the third column is for three unit cells, and the fourth column represents the transmitted power percentage of five unit cells along the $z-$direction. For better visualization of data, we have also plotted transmitted power versus yarn radius for the plain weave structure, which is shown in Fig. 3.23.

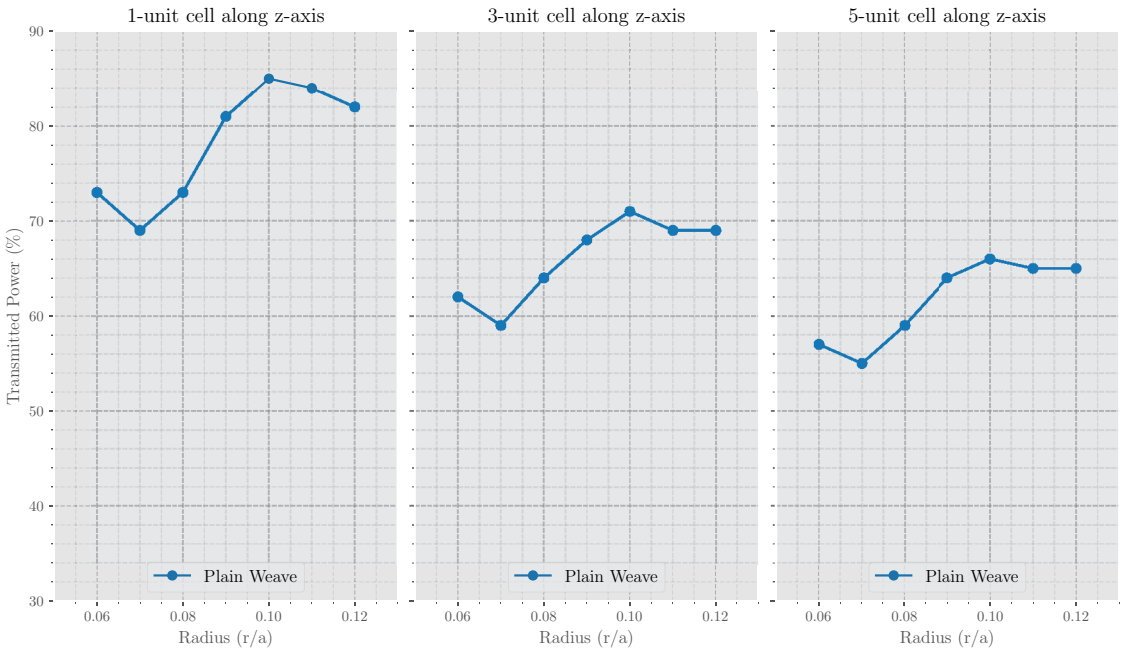


Figure 3.23. Transmitted power percentage versus yarn radius for single unit cell (left graph), three unit cell (middle graph) and five unit cells (right graph).

A variation of the plain weave structure, which is constructed by adding a second layer and shifting the added layer by a quarter of period in both $x-$ and $y-$direction. The resulting structure from 3D view (a), top view (b), and side view (c) is shown in Fig. 3.24. The structure now consists of two layers in a unit cell in the $z-$direction, or stacking direction. The FDTD simulation configuration for a single unit cell (d), three unit cells

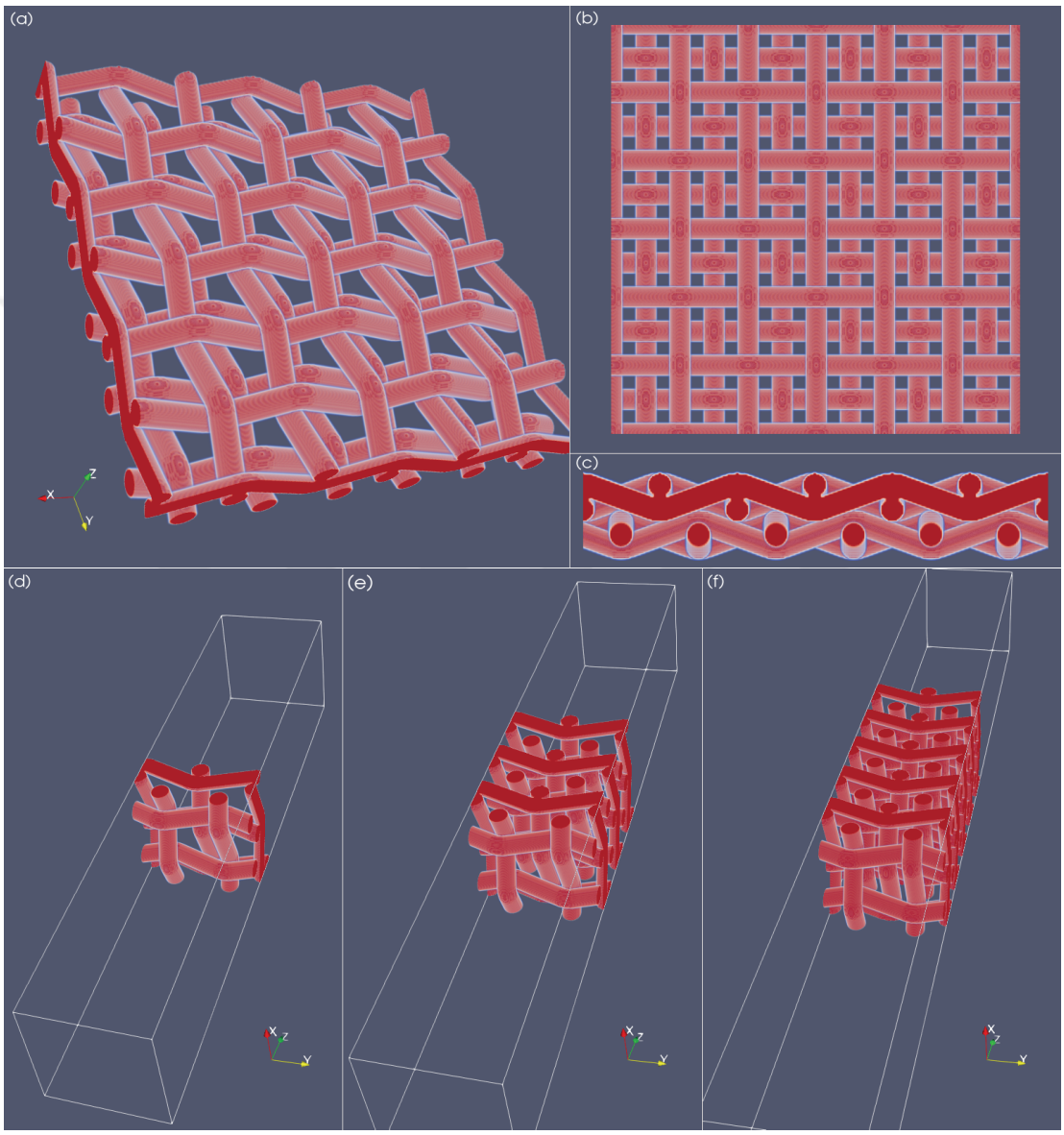


Figure 3.24. (a). 3D view, (b) Top view, (c). Side view of modified plane weave pattern. Simulation setup for modified plane weave pattern. (d). Single unit cell. (e). Three unit cells. (f). Five unit cells.

(e), and five unit cells (f) is shown in Fig. 3.24. With the exception of the lattice constant

along the $z-$direction, all parameters, including the PML thickness, the lattice constant along the $x-$ and $y-$direction, and the distance between the PML and the structure, are the same. The lattice constant along the $z-$direction is $a_z = 8r$ because the structure has two layers. In addition, the same Gaussian profiled plane weave source with center frequency and the same frequency bandwidth is used to excite the electric field. To capture the electromagnetic flux we used the flux monitor that records the electromagnetic fields and take the Fourier transform then calculates the flux.

Transmitted flux are calculated by varying the yarn's radius from $0.05a$ to $0.12a$ in steps of $0.01a$. The best two result are shown in the following figures.

In Fig. 3.25, we plotted transmission spectrum values for modified plain weave structure. The left column of this graph represents the normalized flux for $r = 0.09a$ for single unit cell, three unit cells, and five unit cells, while on the right column we plotted blackbody radiation for temperature $T = 310K$(red dashed lines) and transmission values multiplied by blackbody radiation (blue curve on the right column).

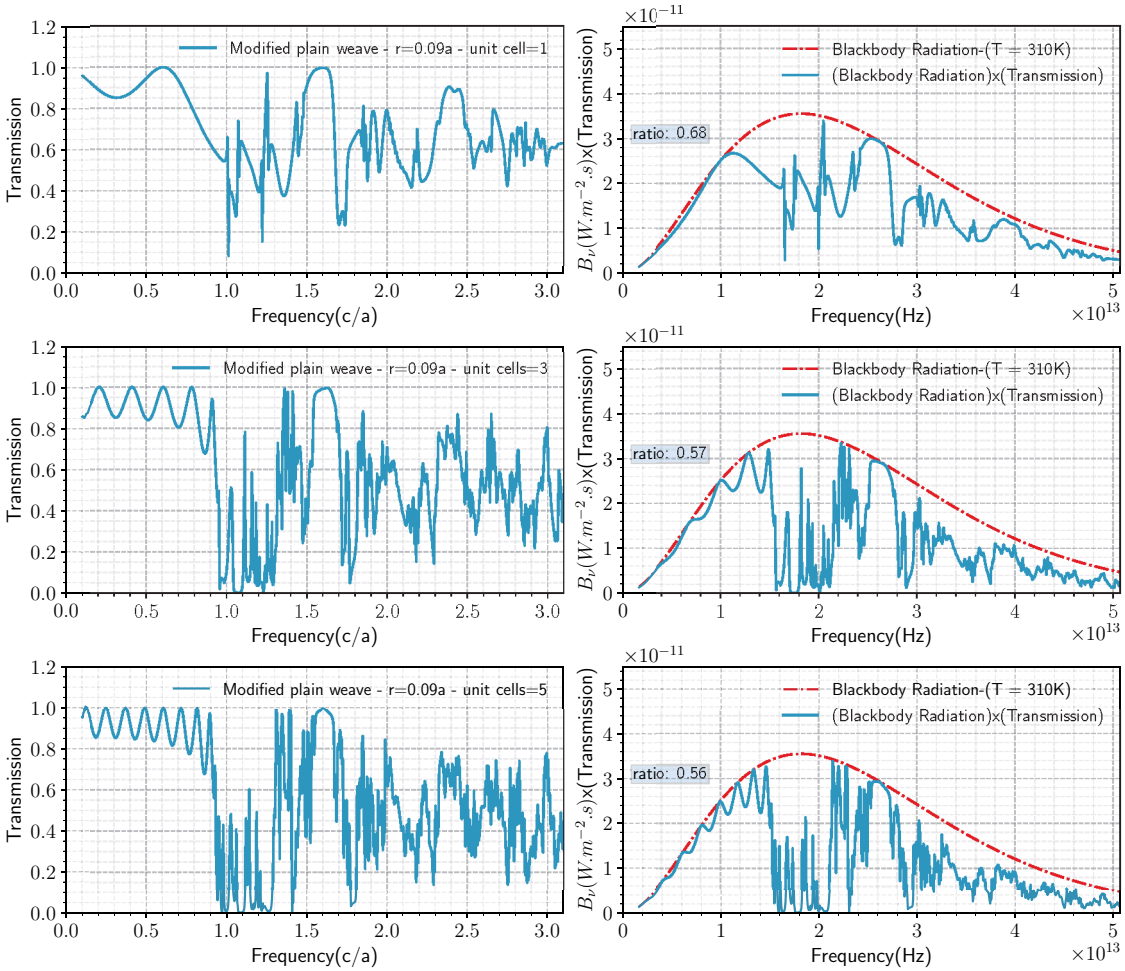


Figure 3.25. Transmission values (blue curve on the left column) and the blackbody radiation (red dashed curve on the right column) multiplied by transmission values of plane weave pattern (blue curve on the right column) for single unit cell, three and five unit cells.

The amount of transmitted power is found to be 68%, 57% and 56% for a single unit cell, three, and five unit cells, respectively.

The transmission spectrum for yarn radius of $r = 0.10a$ and dielectric constant $\epsilon_a = 5.38$ is shown in Fig. 3.26. The blue curves on the left column are the transmission spectrum, the red dashed curve on the right column is the blackbody radiation spectrum, and the blue curves on the right curve are the transmission spectrum for the structure, which is found by multiplying the transmission spectrum with blackbody radiation.

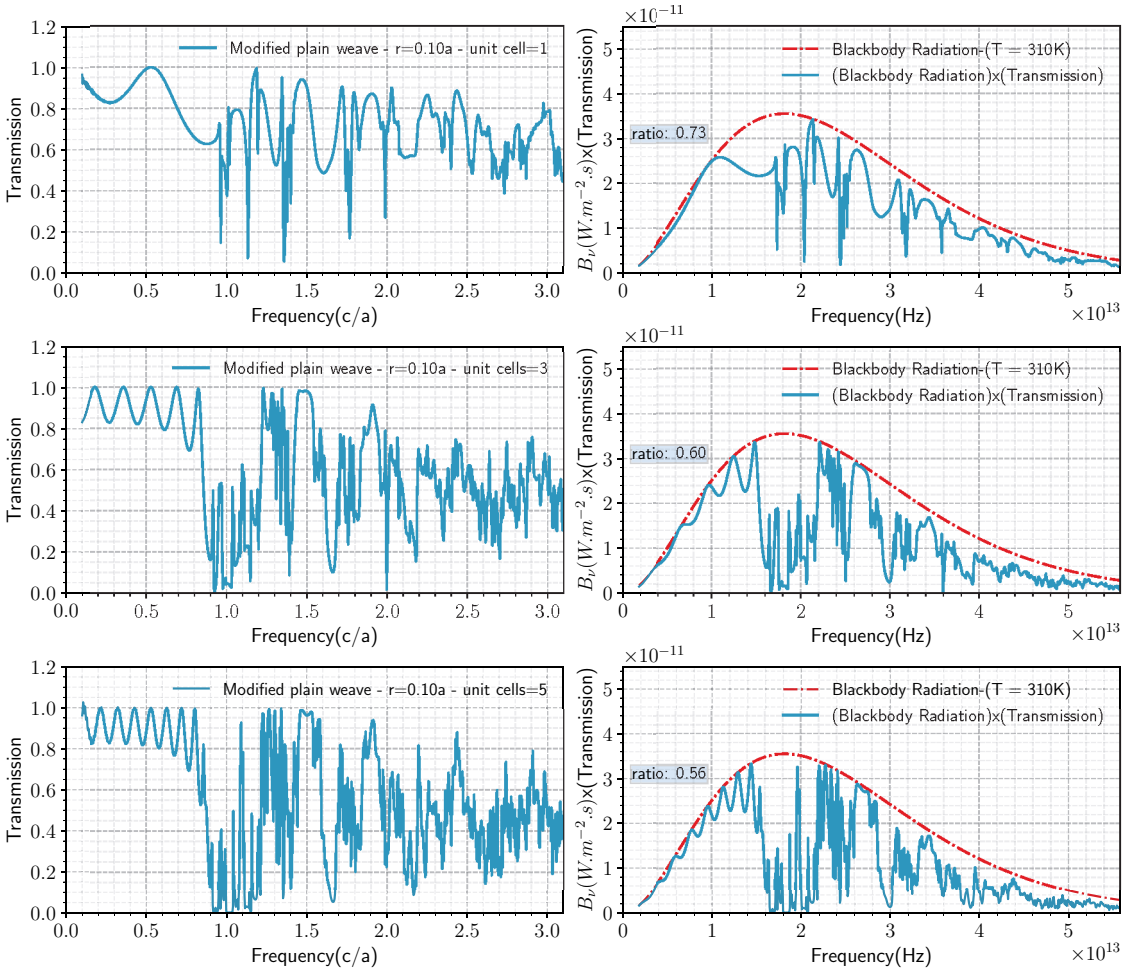


Figure 3.26. Transmission spectrum (blue curve on the left column) and the blackbody radiation (red dashed curve on the right column) multiplied by transmission values (blue curve on the right column) of modified plain weave pattern for single unit cell, three and five unit cells.

The amount of transmitted power is found to be 73% for single unit cell, 60%, and 56% for three and five unit cells.

The remaining calculation results for transmitted power percentage and corresponding yarn radius for modified plain weave for single unit cell, three and five unit cells are shown in Table. 3.3 for yarn radius $0.06 \leq r \leq 0.12a$ in steps of $0.01a$. In this table,

Table 3.3. Percentage of transmitted power for modified plain weave.

Radius(r)	Single unit cell (%)	Three unit cell (%)	Five unit cell (%)
$0.06a$	72	60	57
$0.07a$	67	59	57
$0.08a$	66	59	58
$0.09a$	68	57	56
$0.10a$	73	60	56
$0.11a$	75	65	60
$0.12a$	75	68	66

the first column is the yarn's radius, the second column is the amount of power transmitted for single unit cell, the third column shows the percentage of transmitted power for three unit cells, and the last column shows the transmitted power percentage of five unit cells. The data in Table. 3.3 are also plotted and shown in Fig. 3.27 for better visualization.

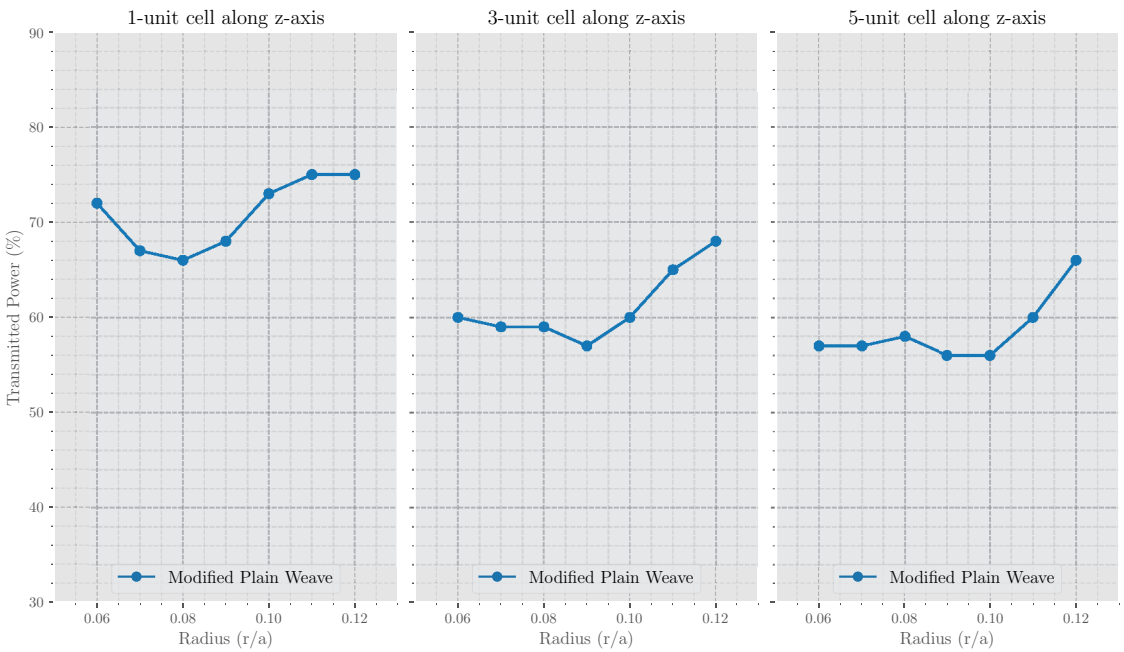


Figure 3.27. Transmitted power percentage versus yarn radius for single unit cell (left graph), three unit cell (middle graph) and five unit cells (right graph).

3.3.2. Basket Weave

The second weave pattern that we will study is basket weave. A 3D view (a), top view (b), and side view (c) of the structure is shown in Fig. 3.28. The FDTD simulation setup is shown in Fig. 3.28 for single unit cell (d), three (e) and five (f) unit cells along $z-$direction.

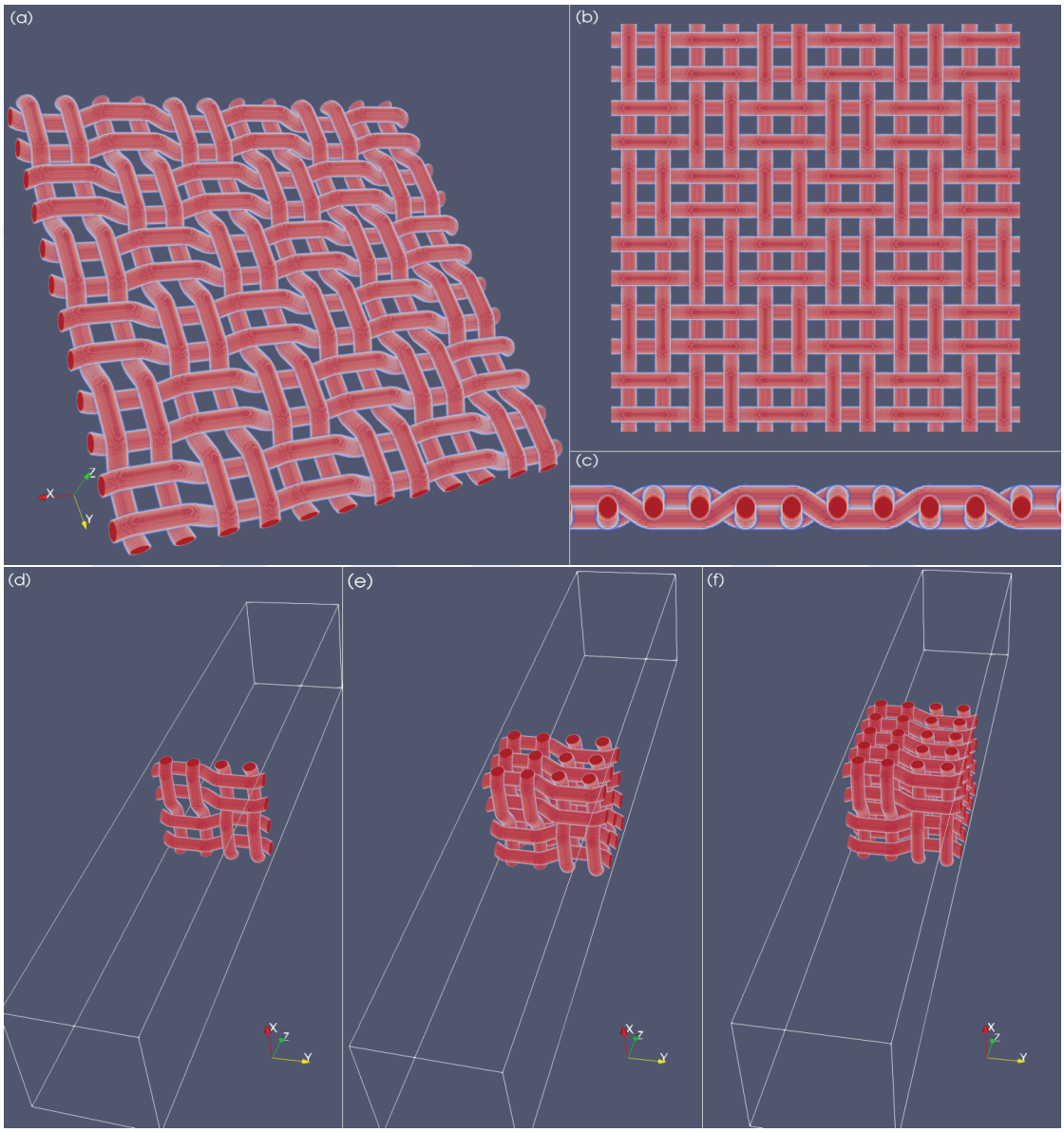


Figure 3.28. Structure of basket weave pattern: (a) 3D view, (b) Top view and (c) Side view. FDTD simulation setup of basket weave pattern for single (d), three (e) and five layers (f).

The pattern's unit cell is defined as $V_{cell} = a_x a_y a_z$, where $a_x = a_y = a$ is the lattice constant along the $x-$and $y-$direction and $a_z = 4r$ is the lattice constant along the $z-$direction. The computational volume is defined as $V_{comp} = S_x S_y S_z$ where $S_x = a_x$, $S_y = a_y$, and $S_z = 2dpml + 2dpad + n_z a_z$ where $dpml$ is the PML thickness, $dpad$ is the distance between the PML and the structure, and n_z is the number of unit cell along the $z-$direction.

Again, a Gaussian source is used to excite the $x-$component of the electric field propagating in the $z-$direction. In the $x - y$ direction PBC is used while PML boundary is used in $z-$direction. As opposed to the plain weave pattern, this structure contains eight yarns in a unit cell, so to be able to put eight yarns in a single unit cell without them overlapping, the radius of the yarn can be $0.06a$ at most. The radius of yarns are taken to be $r = 0.05a$ and $r = 0.06a$ with dielectric constant of $\epsilon_a = 5.38$.

The transmission spectrum for basket weave with radius $r = 0.05a$ is plotted in Fig. 3.29. In the left column, we see the transmission spectrum for one unit cell, three, and five unit cells. In the right column, the blackbody radiation spectrum (red dashed curve) and the blackbody radiation spectrum (red curve) multiplied by transmission values (blue curve) are shown.

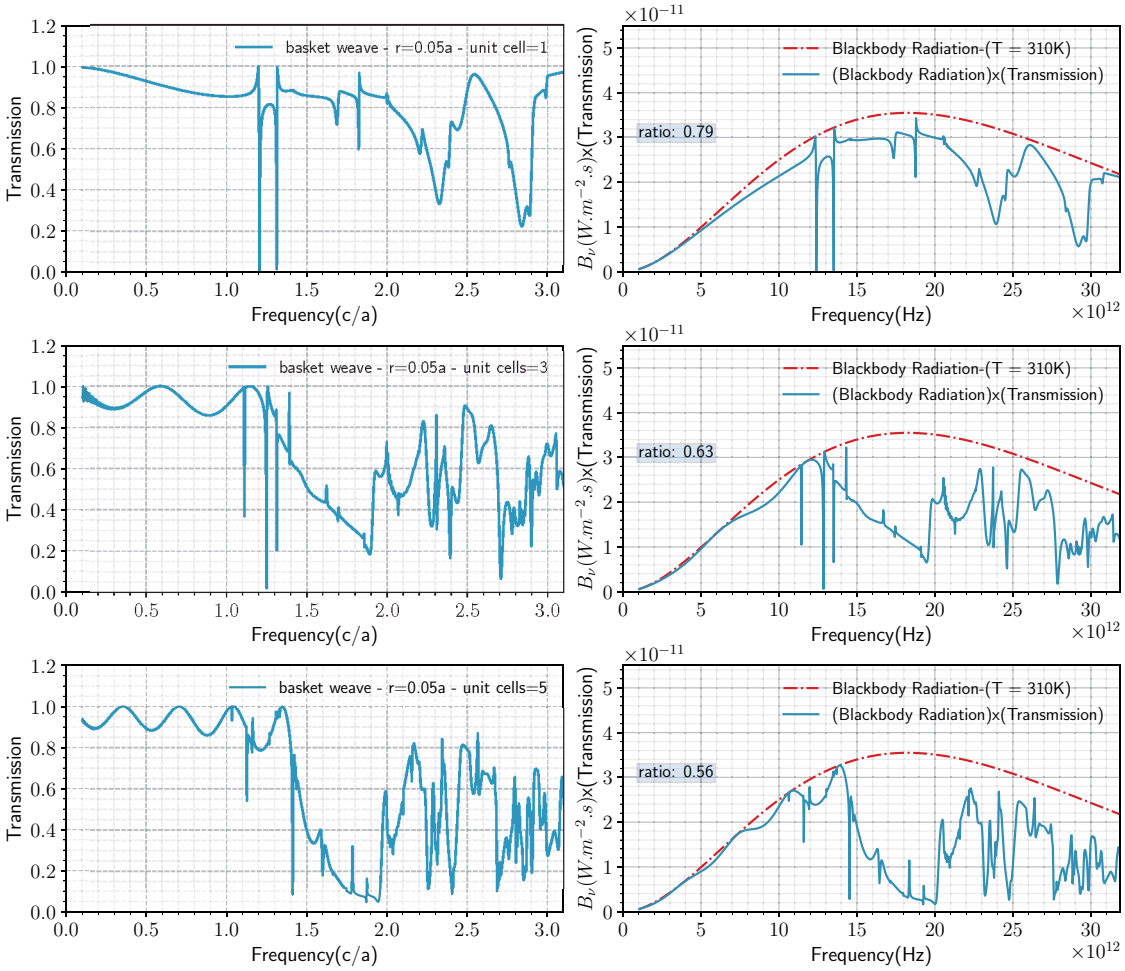


Figure 3.29. The transmission spectrum for the basket weave pattern for single unit cell, three, and five unit cells with dielectric constant of $\epsilon_a = 5.38$ and radius of yarns $r = 0.05a$. (left column). Blackbody radiation spectrum (red dashed curves) and the transmission spectrum of the structure (blue curves on the right column).

The amount of power transmitted for basket weave with radius $r = 0.05a$ are 79%, 63% and 56% for single, three and five unit cell respectively.

For basket weave with radius $r = 0.06a$, the transmission spectrum is plotted in Fig. 3.30. The blue curves on the left column are the transmission spectrum. The blue curves on the right column represent the basked weave pattern transmission spectrum, which is obtained by multiplying the transmission spectrum by blackbody radiation, while the red curves on the right column represent the blackbody radiation spectrum.

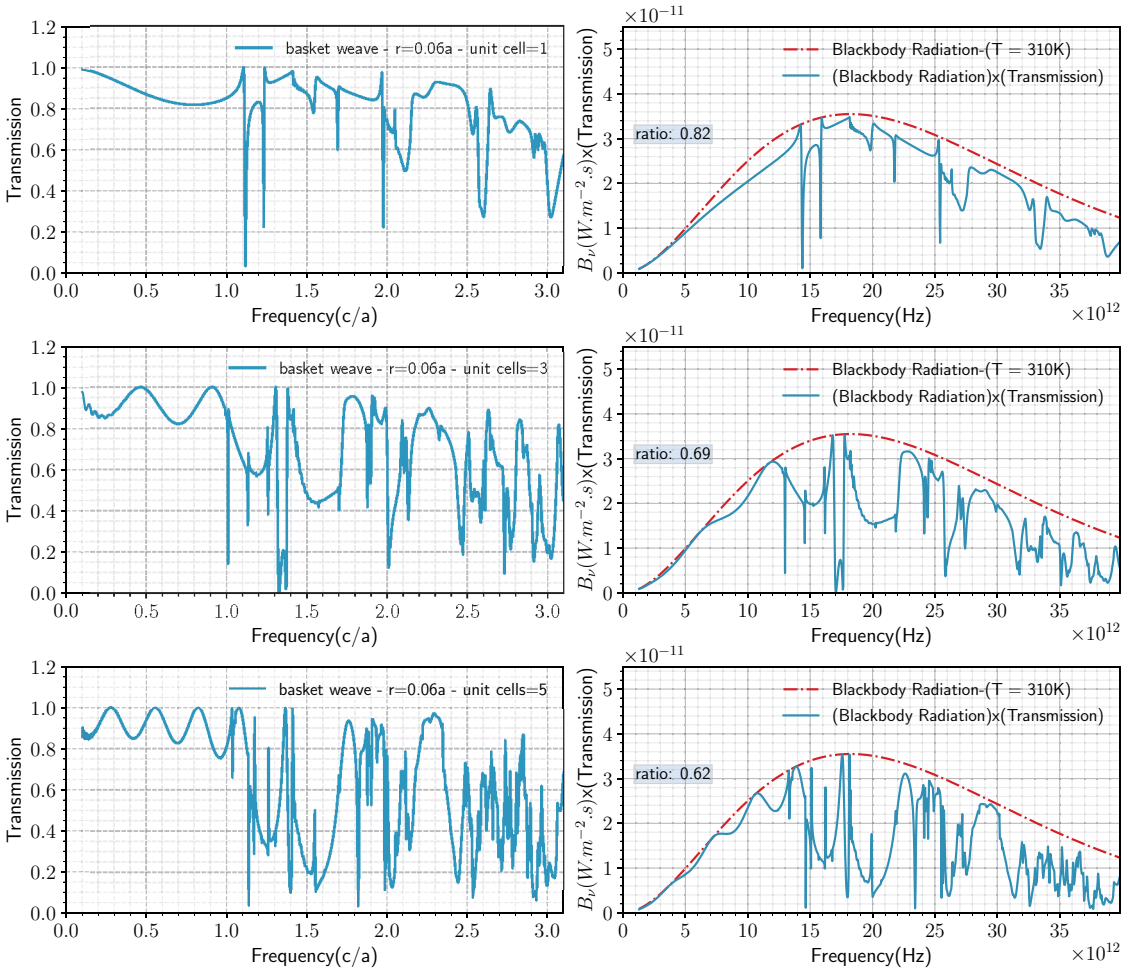


Figure 3.30. The transmission spectrum for the basket weave pattern for single unit cell, three, and five unit cells with dielectric constant of $\epsilon_a = 5.38$ and radius of yarns $r = 0.06a$. (left column). Blackbody radiation spectrum (red dashed curves) and the transmission spectrum of the structure (blue curves on the right column).

The percentage of transmitted power for the structure is calculated as 82%, 69% and 62% for a single unit cell, three, and five unit cells respectively.

A modification for basket weave is also possible. This modified basket weave is constructed by adding an another layer and shifting the added layer by quarter of lattice constant along $x-$ and $y-$direction. The resulting structure is shown in Fig. 3.31, 3D view (a), top view (b) and side view (c). The FDTD simulation setup is shown in Fig. 3.31 for

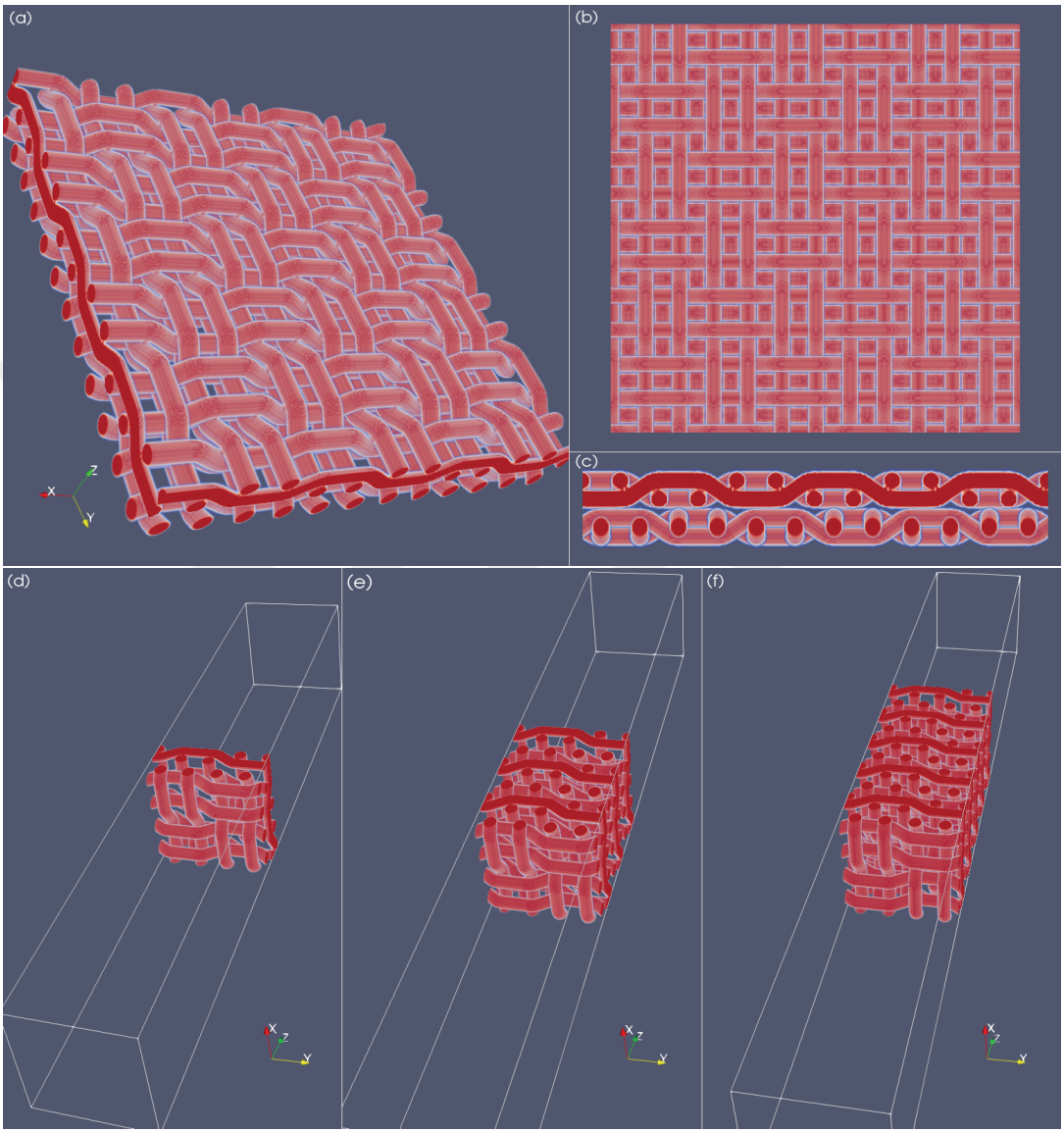


Figure 3.31. Structure of modified basket weave pattern. (a) 3D view, (b) Top view and (c) side view. Simulation setup for basket weave pattern for one unit cell (d), three unit cell (e) and five unit cell (f) in $z-$direction.

single unit cell (d), three (e) and five (f) unit cells along $z-$direction. Again Gaussian source is used to excite $x-$component of the electric field propagating in $z-$direction. In $x-y$ direction PBC is used while PML boundary is used in $z-$direction.

The unit cells of modified basket weave pattern along $x-$ and $y-$direction are the same as the basket weave pattern but the lattice constant in $z-$direction is different, which is $a_z = 8r$. So the volume of a unit cell is defined as $V_{cell} = a_x a_y a_z$. The computational volume is defined as $V_{comp} = S_x S_y S_z$ where $S_x = a_x$, $S_y = a_y$ and $S_z = 2dpml + 2dpad + n_z a_z$ where $dpml$ is the PML thickness and $dpad$ is the distance between the PML and the structure and n_z is the number of unit cell along $z-$direction.

We ran the simulation for two yarn radii, $r = 0.05a$ and $r = 0.06a$, because, as was previously noted, the yarns can only have a maximum radius of $0.06a$ to prevent them from overlapping.

The transmission spectrum for modified basket weave for a single unit cell, three, and five unit cells (left column) with yarn's radius $r = 0.05a$ and dielectric constant $\epsilon_a = 5.38$ is shown in Fig. 3.32. The pattern is immersed in an air background with dielectric constant value of $\epsilon_b = 1.0$. The blackbody radiation spectrum (red dashed curve on the right column), and transmission values multiplied by the blackbody radiation spectrum (blue curve on the right column) are also plotted.

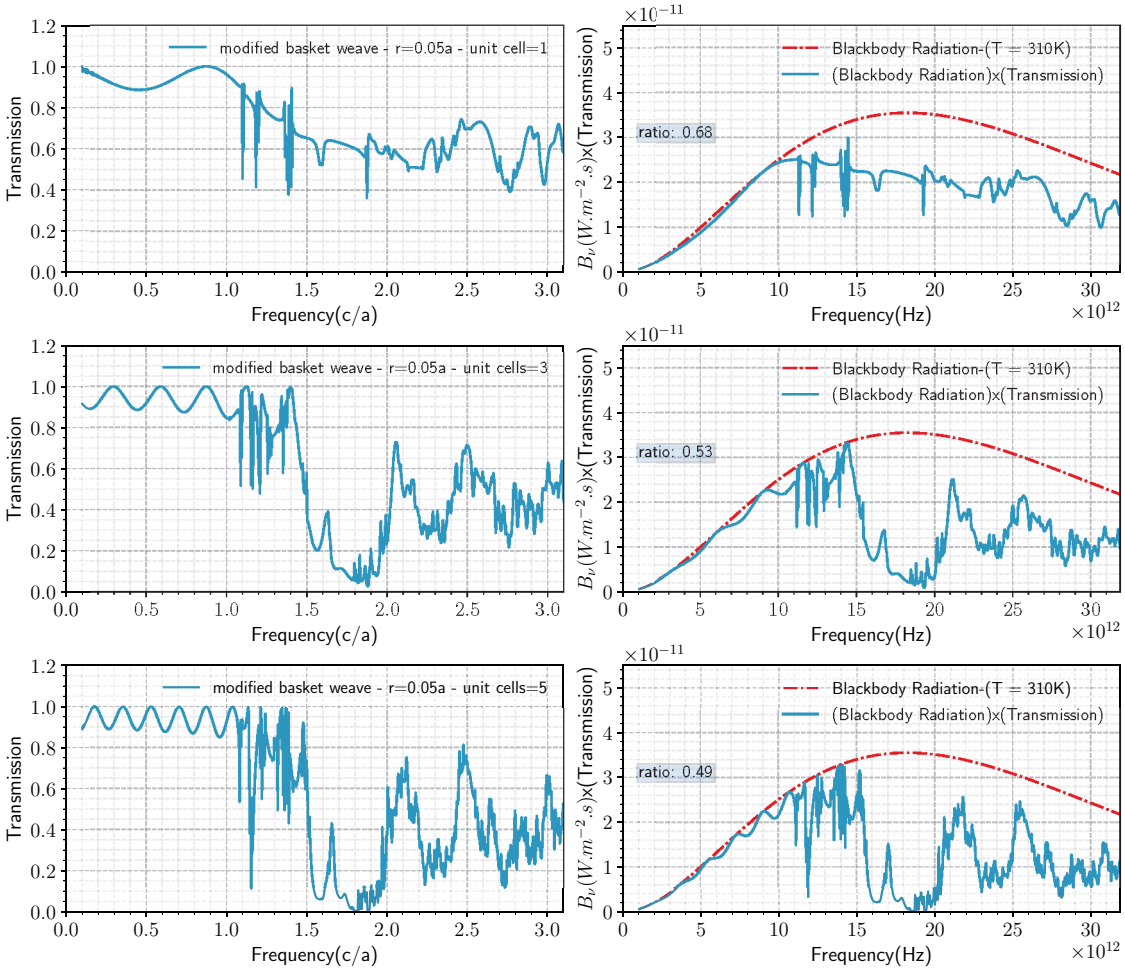


Figure 3.32. The transmission spectrum for modified basket weave with radius $r = 0.05a$(left column). Blackbody radiation spectrum (red dashed curve on the right column), and transmission values multiplied bu blackbody radiation spectrum (blue curve on the right column)

The percentage of power transmitted is 68%, 53% and 49% for single, three and five unit cell respectively.

Fig. 3.33 shows the transmission spectrum (left column) of a modified basket weave for a single unit cell, three unit cells, and five unit cells. This figure also shows the blackbody spectrum (red dashed curve) and the transmission spectrum multiplied by the blackbody spectrum (blue curve in the right column). The yarn's radius is $r = 0.06a$ and its dielectric constant is $\epsilon_a = 5.38$. The pattern is immersed in an air background with dielectric constant value of $\epsilon_b = 1.0$.

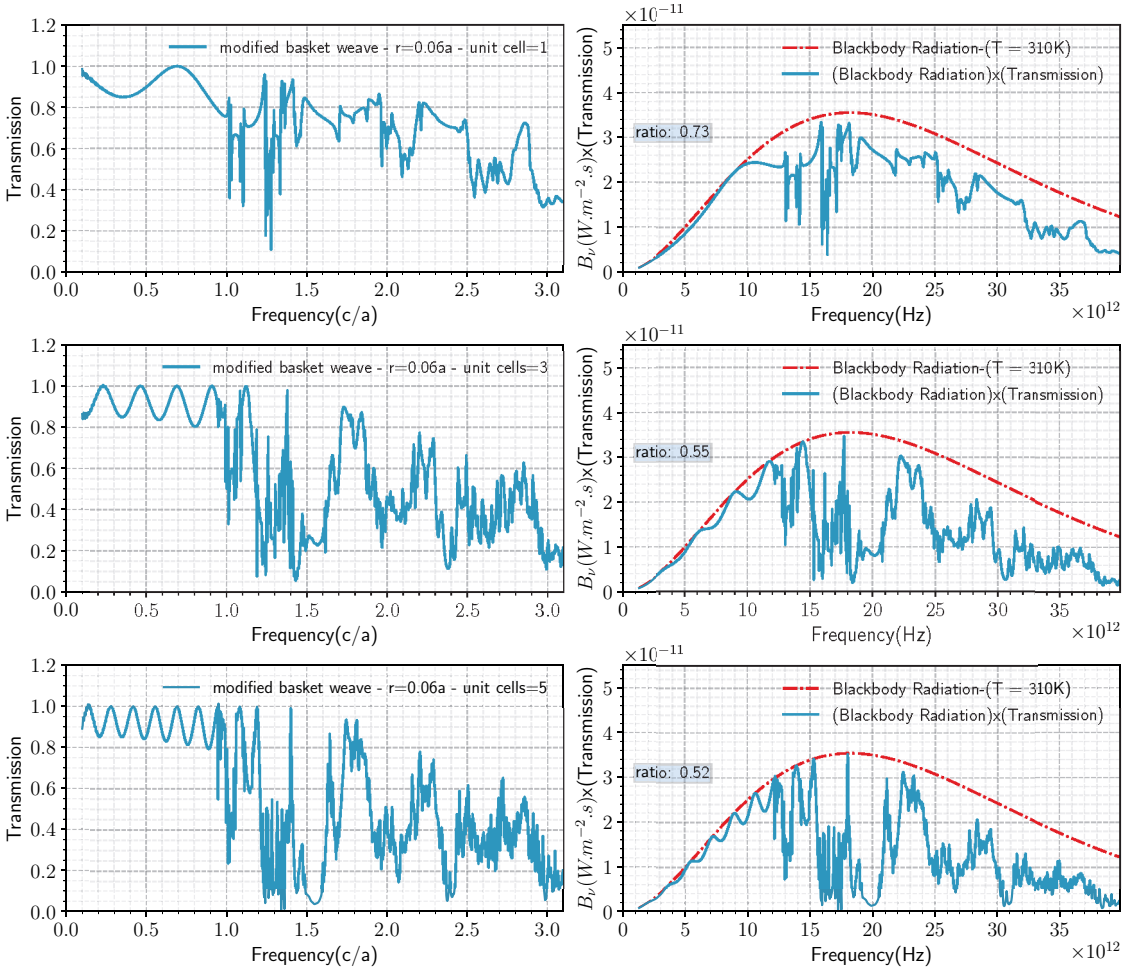


Figure 3.33. The transmission spectrum for modified basket weave with radius $r = 0.06a$ (left column). Blackbody radiation spectrum (red dashed curve on the right column), and transmission values multiplied bu blackbody radiation spectrum (blue curve on the right column)

The amount of power transmitted is found to be 73%, 55% and 52% for single, three and five unit cell.

3.3.3. Twill Weave

Another structure we study in this section is twill weave pattern which is shown in Fig. 3.34. In this figure we have shown the structure from three different viewing angles, (a) 3D view, (b) top view and (c) side view. In the same figure, Fig. 3.34, we have shown

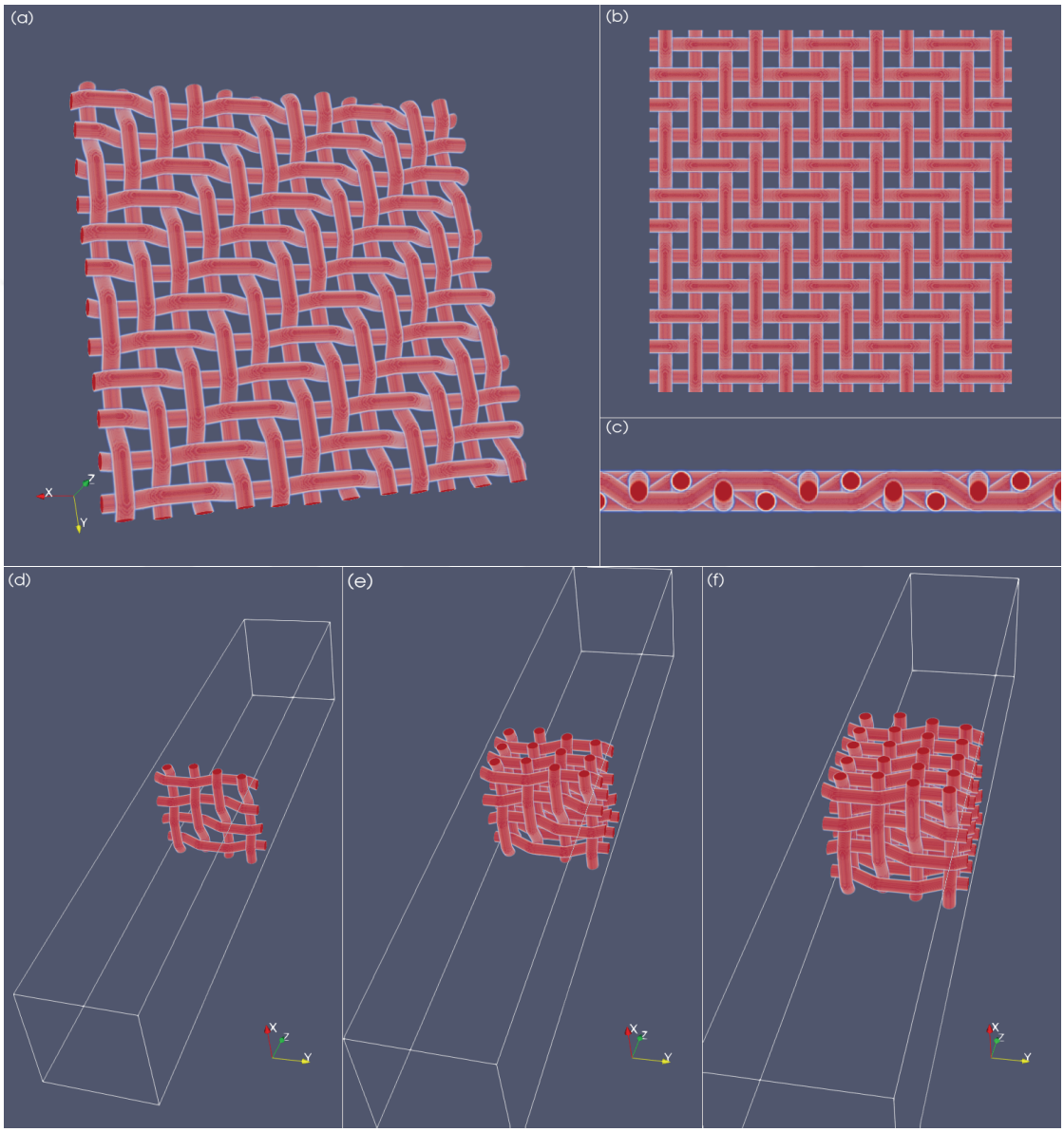


Figure 3.34. Structure of twill weave pattern. (a) 3D view, (b) Top view and (c) Side view. Simulationsetup for twill weave pattern: (d) Single unit cell, (e) Three unit cells and (f) Five unit cells along $z-$direction.

the FDTD computational setup for single unit cell (d), three (e) and five (f) unit cells

along the stacking direction for twill weave pattern. The volume of a unit cell is defined as $V_{cell} = a_x a_y a_z$ where $a_x = a_y = a$ and $a_z = 4r$. The computational volume is defined as $V_{comp} = S_x S_y S_z$ where $S_x = S_y = a_x = a_y = a$ and $S_z = 2dpml + 2dpad + n_z a_z$, where n_z is the number of unit cell in $z-$direction and a_z is the lattice constant along $z-$direction.

To excite the $x-$component of the electric field, we used a Gaussian profiled plane wave source with center frequency $\tilde{\omega} = 1.60$ and bandwidth $\Delta\tilde{\omega} = 3.0$. To calculate the transmission spectrum we used a flux monitor that captures the electric field and take the Fourier transform of electromagnetic fields over time. The boundary conditions used in the simulation is PBC in the $x - y$ plane and PML is used as open boundary condition in the $z-$direction.

The FDTD calculations are done for two different yarn radius, $r = 0.05a$ and $r = 0.06a$ with a fixed dielectric constant of $\epsilon_a = 5.38$ and the whole structure is immersed in air ($\epsilon_b = 1.0$).

Transmission results shown in Fig. 3.35 is for yarn radius $r = 0.05a$. The left column shows transmission values, while the blue curves on the right column, which are obtained by multiplying these transmission values by the spectrum of blackbody radiation (red dashed curves), is the transmission spectrum of the structure. The area under each curve on the right column represents the total energy. When these areas were propor-

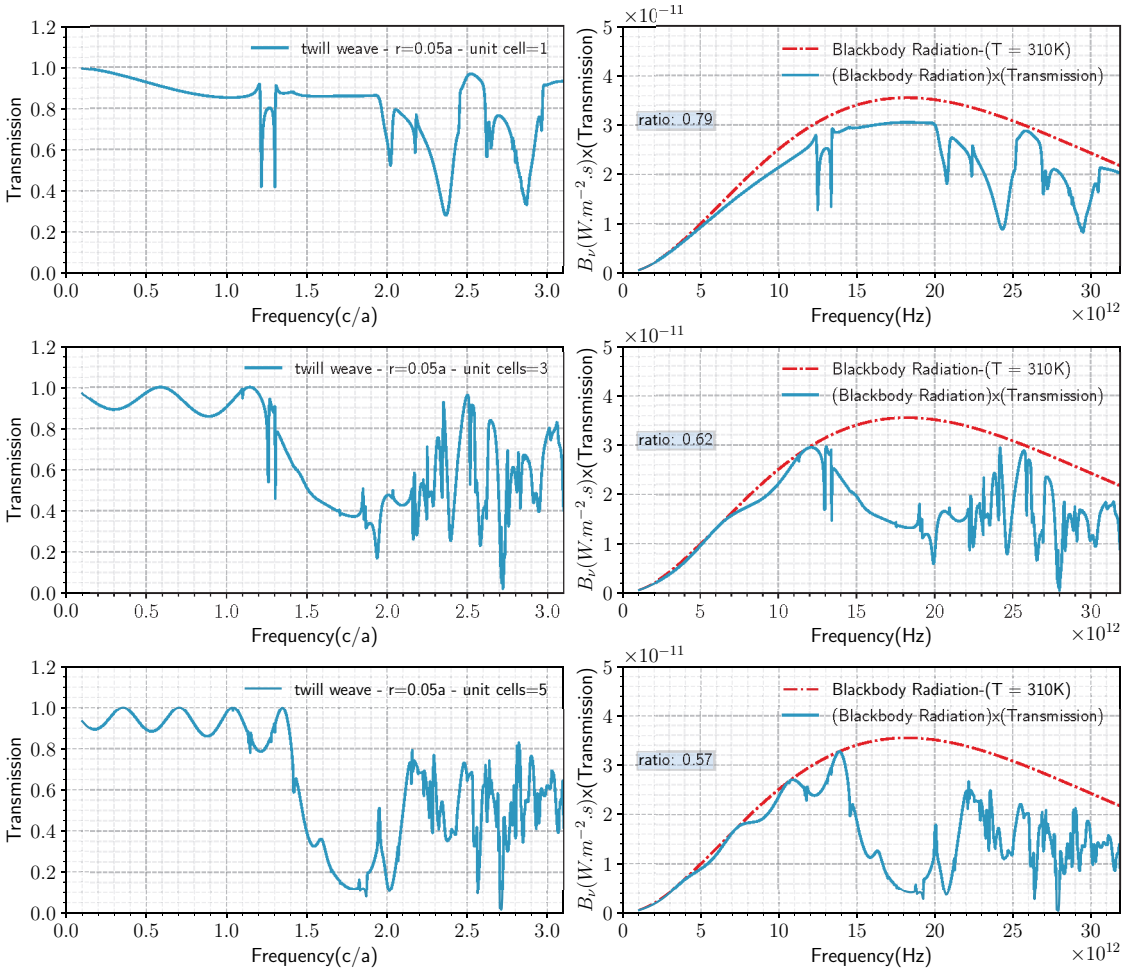


Figure 3.35. The transmission values for twill weave pattern. Single unit cell, three and five unit cell (left column). Blackbody radiation spectrum (red dashed curves on the right column) and transmission values multiplied by blackbody radiation (blue curves on the right column).

tioned, we found that the amount of transmitted power for a twill weave pattern with a radius of $r = 0.05a$ was 79% for a single unit cell, 62% for three unit cells, and 57% for five unit cells.

In Fig. 3.36, we see the transmission spectrum for the same structure with a radius of $r = 0.06a$. The blue curves on the left column are the transmission spectrum of the twill weave pattern. The red-dash curves on the right column are the blackbody radiation spectrum for an object at a temperature of $T = 310K$ with a peak frequency, $\nu = 18.22$THz. The blue curves on the right column are the transmission spectrum for the structure, which is found by multiplying the transmission spectrum with blackbody spectrum. We determined how much power is transmitted by the twill weave by dividing

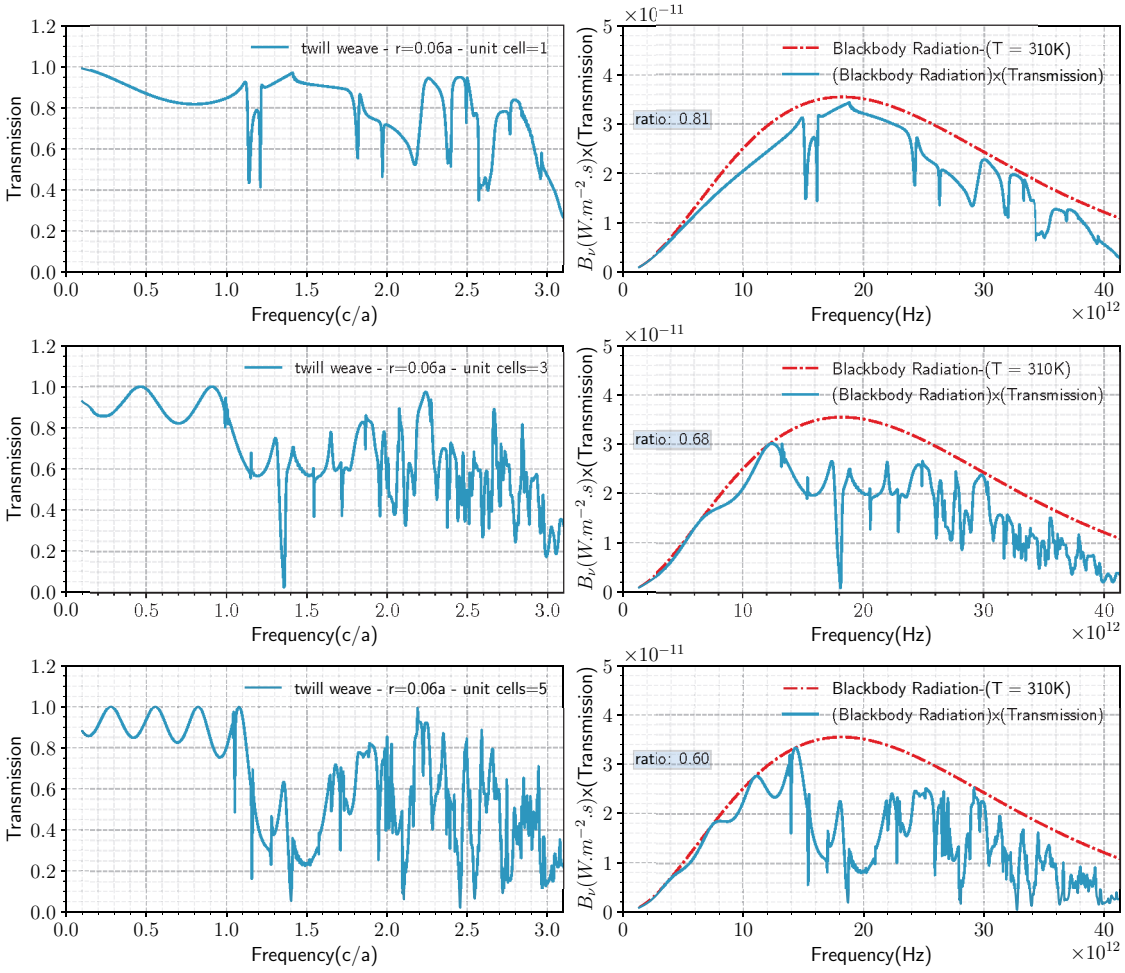


Figure 3.36. The transmission values for twill weave pattern. Single unit cell, three and five unit cell (left column). Blackbody radiation spectrum (red dashed curves) and transmission values multiplied by blackbody radiation (blue curves on the right column).

the area under the blackbody radiation curve and the structure's radiation curve. For this construction, the power that is transmitted is calculated to be 81%, 68%, and 60% for one unit cell, three unit cells, and five unit cells, respectively.

Another variation of twill weave pattern can be constructed by adding a second layer and shifting the added layer by a quarter of a unit cell along $x-$ and $y-$direction, which is called "modified twill weave". So the unit cell along $z-$direction contains two layers. The resulting structure is shown in Fig. 3.37, the 3D view (a), the top view (b), and the side view (c). The FDTD computational setup of the modified twill weave pattern

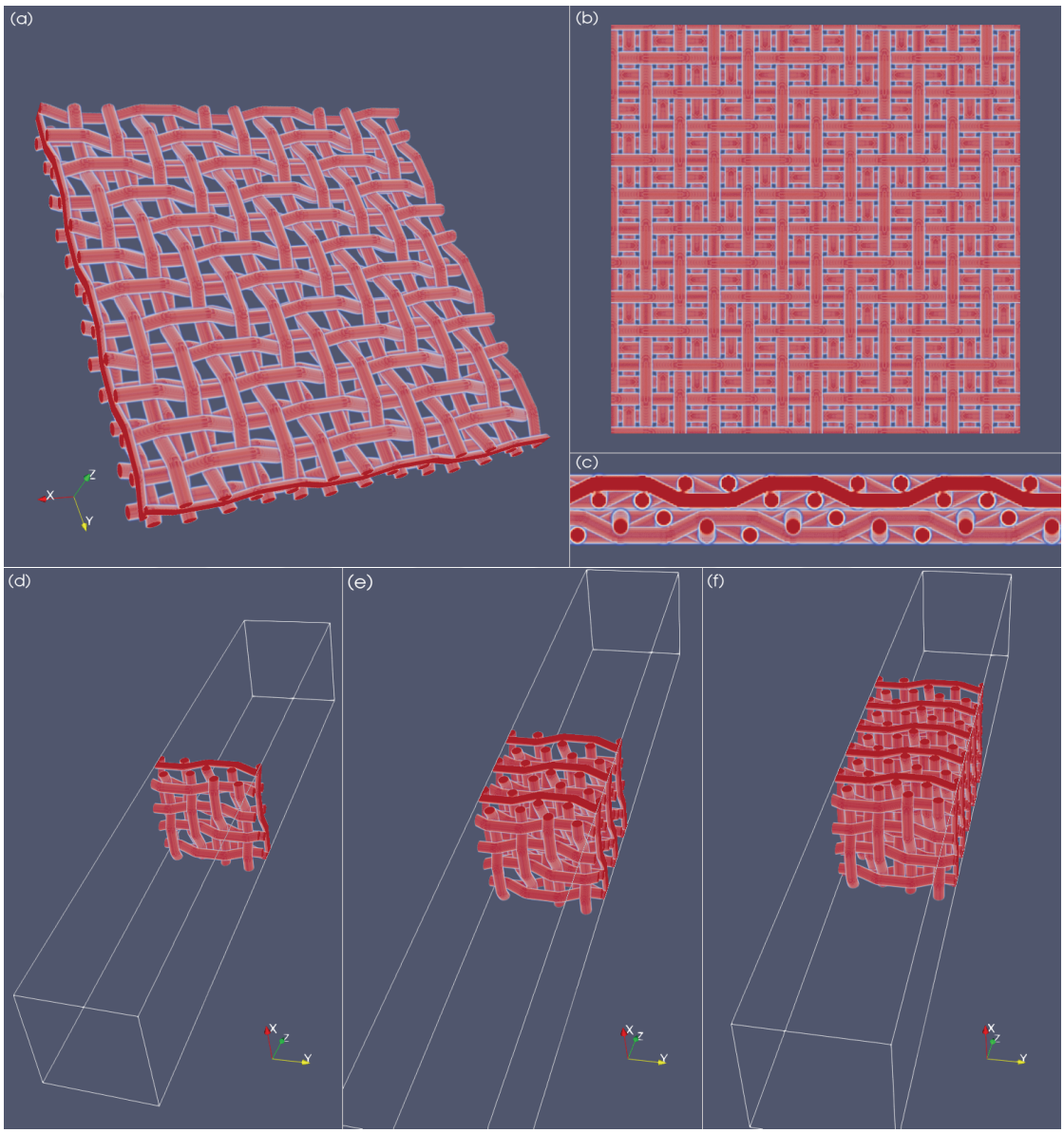


Figure 3.37. Structure of modified twill weave pattern. (a.) 3D view, (b.) Top view and (c.) Side view. Simulation setup: (d) Single unit cell, (e) Three and (f) Five unit cells.

for single unit cell (d), three (e), and five (f) unit cells are shown in Fig. 3.37. The

volume of a unit cell is defined as $V_{cell} = a_x a_y a_z$. The lattice constant in the $z-$direction for this structure is $a_z = 8r$ and the computational volume is $V_{comp} = S_x S_y S_z$ where $S_x = S_y = a_x = a_y = a$ and $S_z = 2dpml + 2dpad + n_z a_z$ and n_z is the number of unit cell along $z-$direction. Again, as in the previous calculations, a Gaussian profiled plane wave source is used to excite $x-$component of the electric field and PBC and PML boundary conditions are used.

For this structure, we calculated the transmission spectrum for two yarn radius, $r = 0.05a$ and $r = 0.06a$, with dielectric dielectric constant of $\epsilon_a = 5.38$. The calculation is only performed for those two values because larger radius values result in the yarns overlapping.

The calculated transmission spectrum of a modified twill weave with a yarn radius of $r = 0.06a$ for single unit cell, three and five unit cells are shown on left column of Fig. 3.38. On the right column the corresponding scaled transmission spectrum (blue curve) and the blackbody radiation is plotted (dashed red curve). The ratio of transmitted

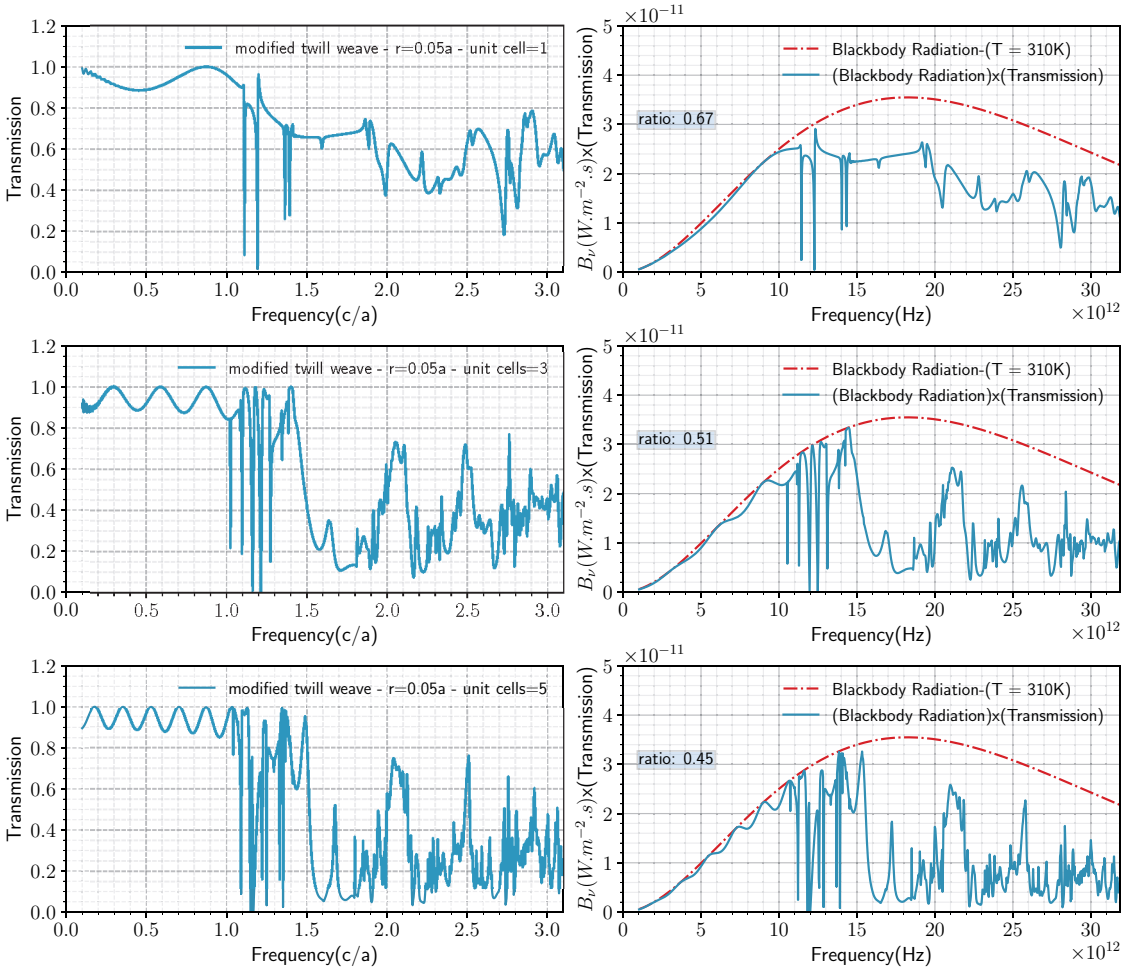


Figure 3.38. The transmission spectrum for modified twill weave pattern with radius of $r = 0.05a$ (blue curves on the left column). Blackbody radiation (red dashed) and transmission spectrum multiplied by blackbody spectrum for single unit cell, three and five unit cells.

power and power radiated by blackbody is a measure of how the structure is capable of blocking electromagnetic radiation. After taking ratio of calculated power under each curve, for a single unit cell, three and five unit cells, the percentage of transmitted power for this structures are found as 67%, 51% and 45% respectively.

The transmission spectrum of a modified twill weave with a yarn radius of $r = 0.06a$ shown in the left column of Fig. 3.39 is for single unit cell, three, and five unit cells. In the right column of Fig. 3.39, blackbody radiation (red dashed curve) with a peak frequency of 18.22THz and transmission spectrum multiplied by blackbody radiation are shown (blue curve on the right column). We first shifted the center frequency of the

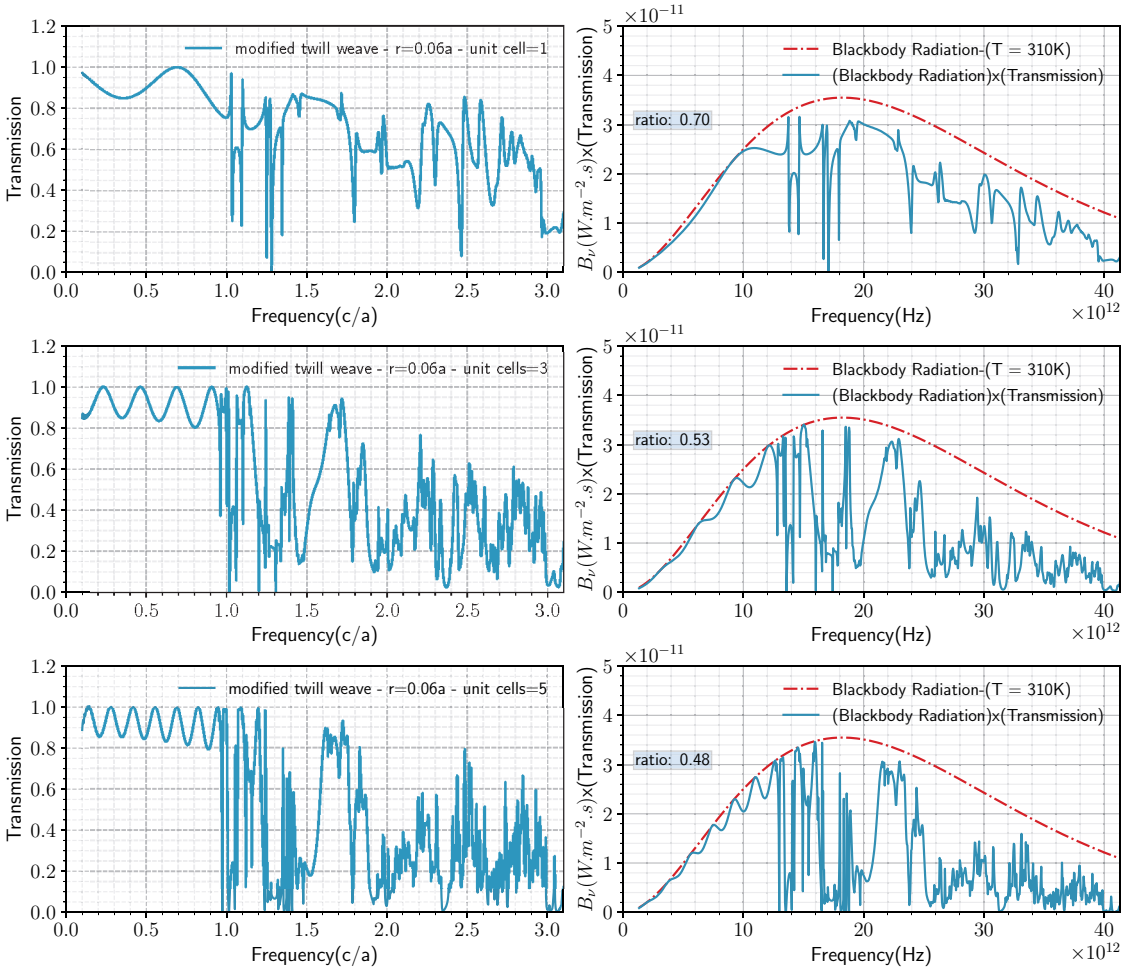


Figure 3.39. The transmission spectrum for the modified twill weave pattern (blue curves on the left column) for a single unit cell, three and five unit cells. Blackbody radiation (red dashed curves on the right column) and transmission spectrum multiplied by blackbody radiation (blue curves on the right column).

band gap to the peak frequency and then multiplied the transmission spectrum with the blackbody radiation curve. Then when we compare the areas under the graphs, we find that the amount of power transmitted is 70%, 53% and 48% for a single unit cell, three, and five unit cells, respectively.

3.3.4. Dutch Weave

The Fig. 3.40 displays the structure of the Dutch weave pattern from three different perspectives; 3D view Fig. 3.40(a), top view Fig. 3.40(b), and side view Fig. 3.40(c). The

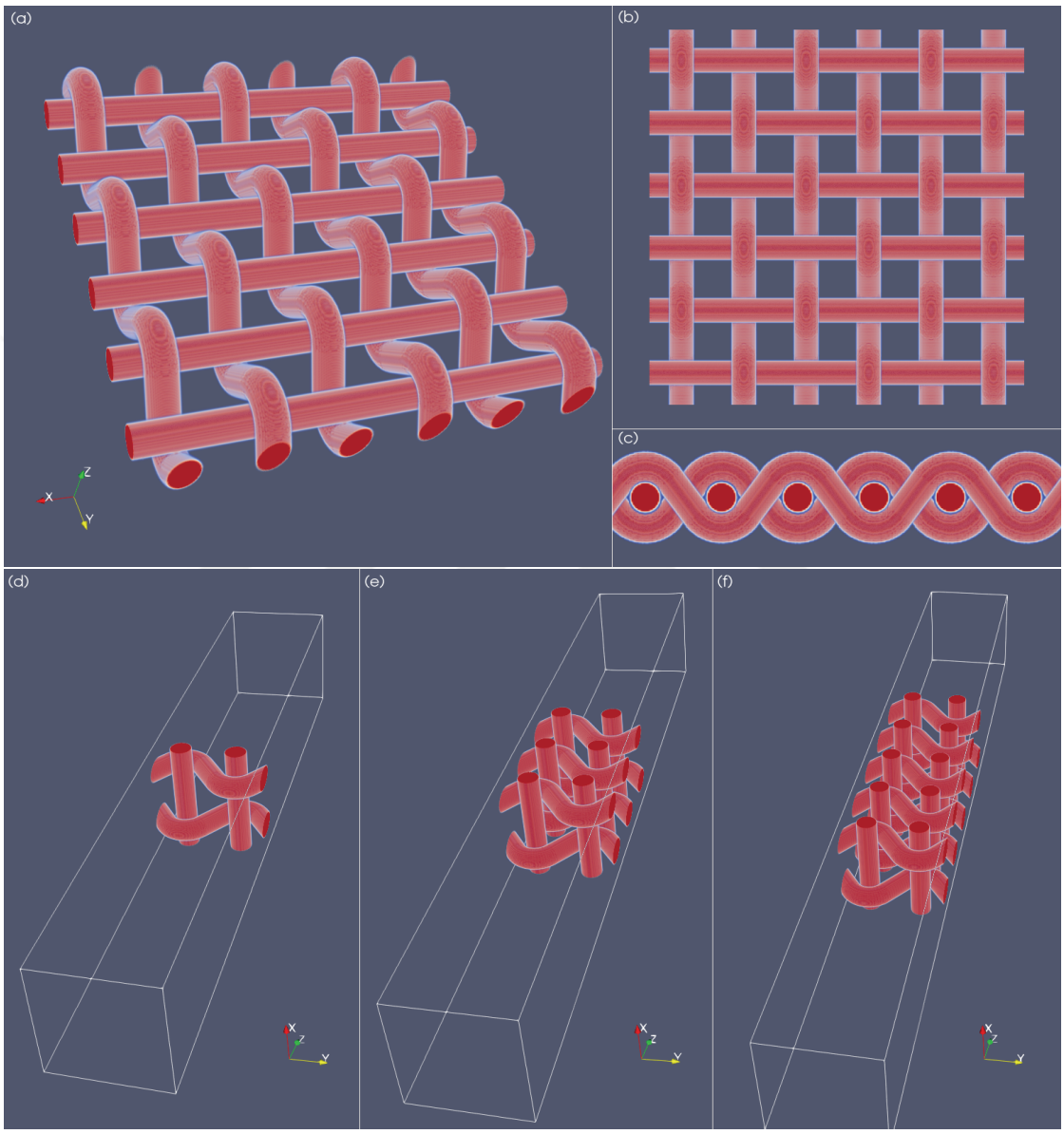


Figure 3.40. Structure of dutch weave pattern. (a) 3D view, (b) Top view and (c) Side view. Simulation setup for single unit cell (d), three (e) and five (f) unit cells.

FDTD simulation setup for dutch weave is also shown in Fig. 3.40; (d) is for a single unit cell, while (e) is for three unit cells, and (f) is for five unit cells in the $z-$direction. In the

$x-$ and $y-$direction we used single unit cell.

As in the previous calculations, PML and PBC are used as boundaries. The volume of a unit cell for this structure is $V_{cell} = a_x a_y a_z$ where $a_x = a_y = a$ and $a_z = 6r$. The computational volume used in FDTD simulation is $V_{comp} = S_x S_y S_z$ where $S_x = S_y = a_x = a_y = a$ and $S_z = 2dpml + 2dpad + n_z a_z$ where $dpml$ is the thickness of PML region, $dpad$ is the distance between PML region and the structure, and n_z is the number of unit cell along $z-$direction. A Gaussian profiled plane wave source is used to excite the $x-$component of the electric field.

For this structure, the calculated transmission spectrum for a single unit cell, three unit cells, and five unit cells is shown in Fig. 3.41. The calculations are done for a yarn radius of $r = 0.06a$ with a dielectric constant of $\epsilon_a = 5.38$. We first shift the peak frequency of the blackbody radiation spectrum to the center frequency and then multiply the transmission spectrum with the blackbody spectrum, which gives us the blue curve in the right column of the Fig. 3.41.

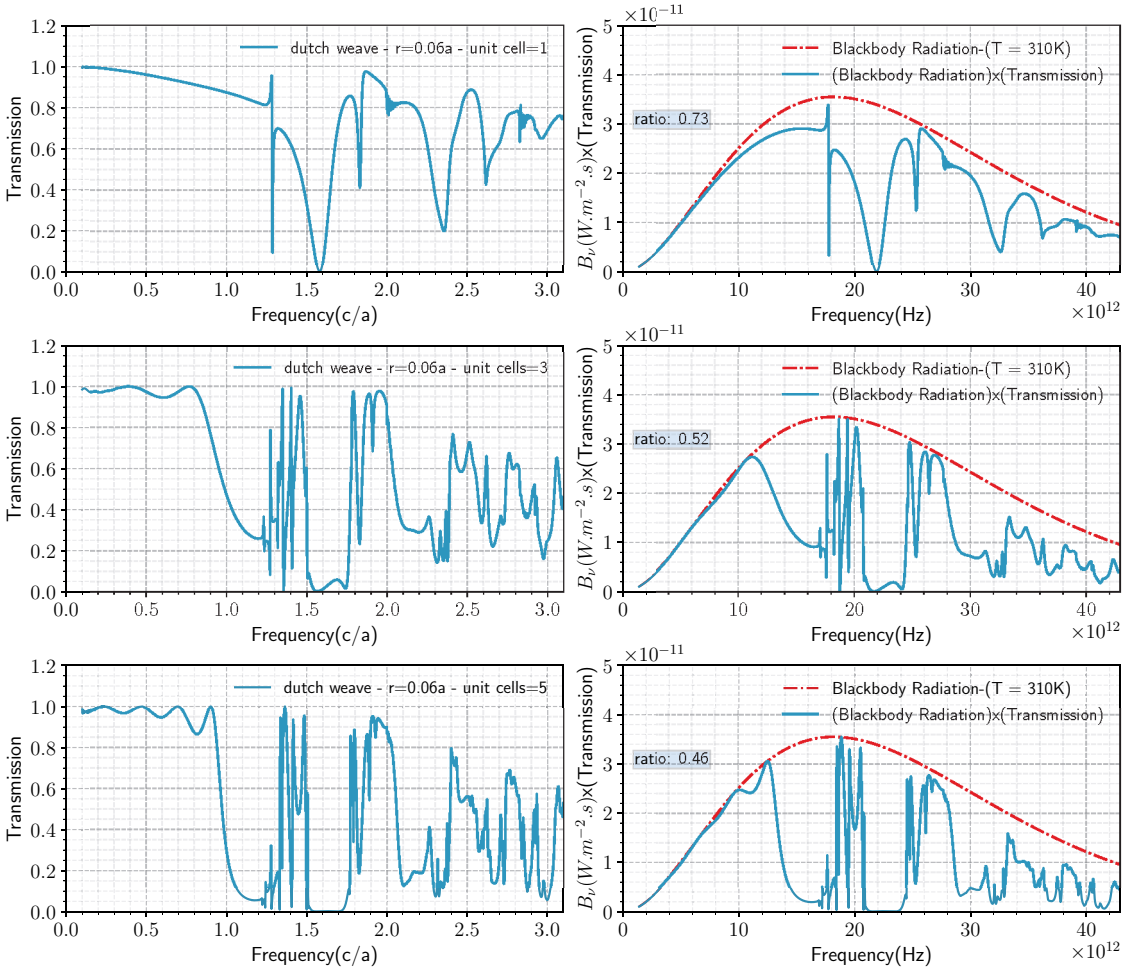


Figure 3.41. Left column: Transmission spectrum for single unit cell, three and five unit cell. Right column: Blackbody radiation spectrum (dashed red curve). Transmission spectrum of the dutch weave pattern multiplied by blackbody radiation (blue curve).

The transmitted percentage power for single, three and five unit cell are calculated as 73%, 52% and 46%.

Transmission values for the same structure with a radius of $r = 0.08a$ are shown in Fig. 3.42. The blue curves on the left column are the transmission spectrum, the red-dash curve on the right column is the blackbody radiation spectrum, and the blue curve on the right column is the transmission spectrum for the structure, which is found by multiplying the transmission spectrum with blackbody radiation.

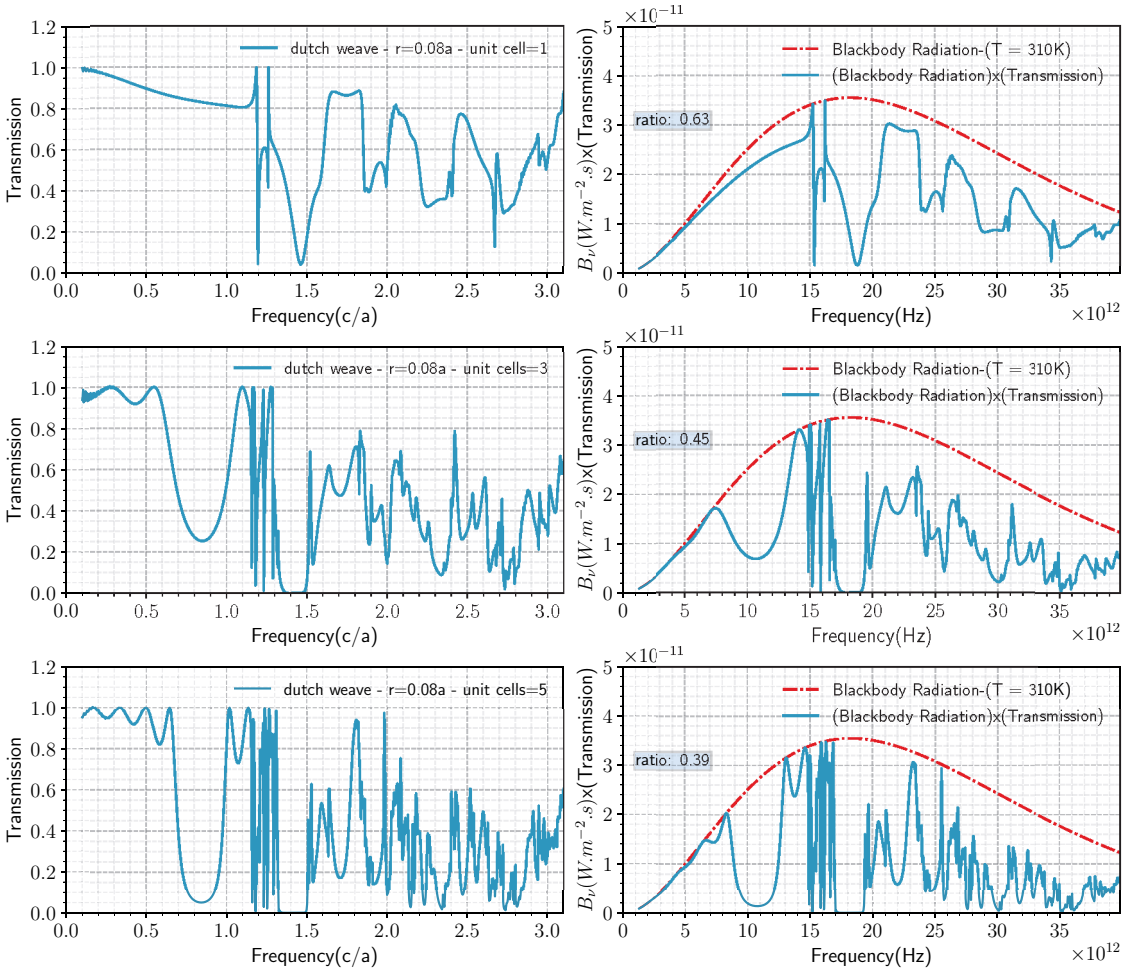


Figure 3.42. Left column: Transmission spectrum for single unit cell, three and five unit cell. Right column: Blackbody radiation spectrum (dashed red curve). Transmission spectrum of the dutch weave pattern multiplied by blackbody radiation (blue curve).

The amount of transmitted power are calculated to be 63%, 45% and 39% for single, three and five unit cell respectively.

We scanned the radius of yarns from 0.06a to 0.12a in steps of 0.01a, and the percentage of the transmitted power for Dutch weave for single unit cell, three and five unit cells calculated and the results are shown in Table. 3.4. The first column shows

Table 3.4. Percentage of transmitted power for dutch weave.

Radius(r)	Single unit cell (%)	Three unit cell (%)	Five unit cell (%)
$0.06a$	73	52	46
$0.07a$	66	46	41
$0.08a$	63	45	39
$0.09a$	62	42	37
$0.10a$	76	59	55
$0.11a$	80	65	61
$0.12a$	83	67	64

the radius of yarns while the second column is for single unit cell, third column is for the three unit cells, and the last column is for the five unit cell along z-direction. The Fig. 3.43

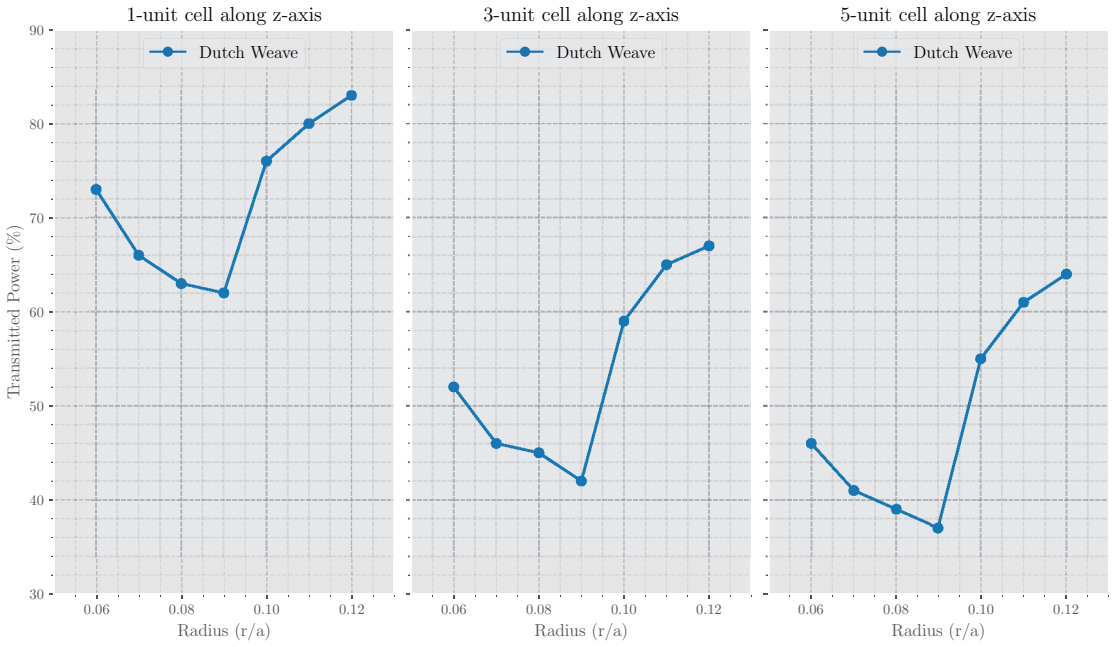


Figure 3.43. Transmitted power percentage versus yarn radius for the dutch weave. Single (left graph) unit cell, three (middle graph) unit cells and five (right graph) unit cells.

shows plot of data tabulated in Table. 3.4 which depicts the percentage of power versus yarn radius for single, three and five unit cell along $z-$direction.

Taking dutch weave pattern as a base, two more patterns can be constructed. The first one is made by connecting two straight yarns that are parallel to each other and separated by a distance. The center-to-center distance of these yarns is taken to be $4r$, where r is the radius of the yarn. Then these neighboring yarns are connected to each other by yarns running in a perpendicular direction. This structure is shown in Fig.3.44, where (a) is 3D view, (b) is view from top, and (c) is view from side.

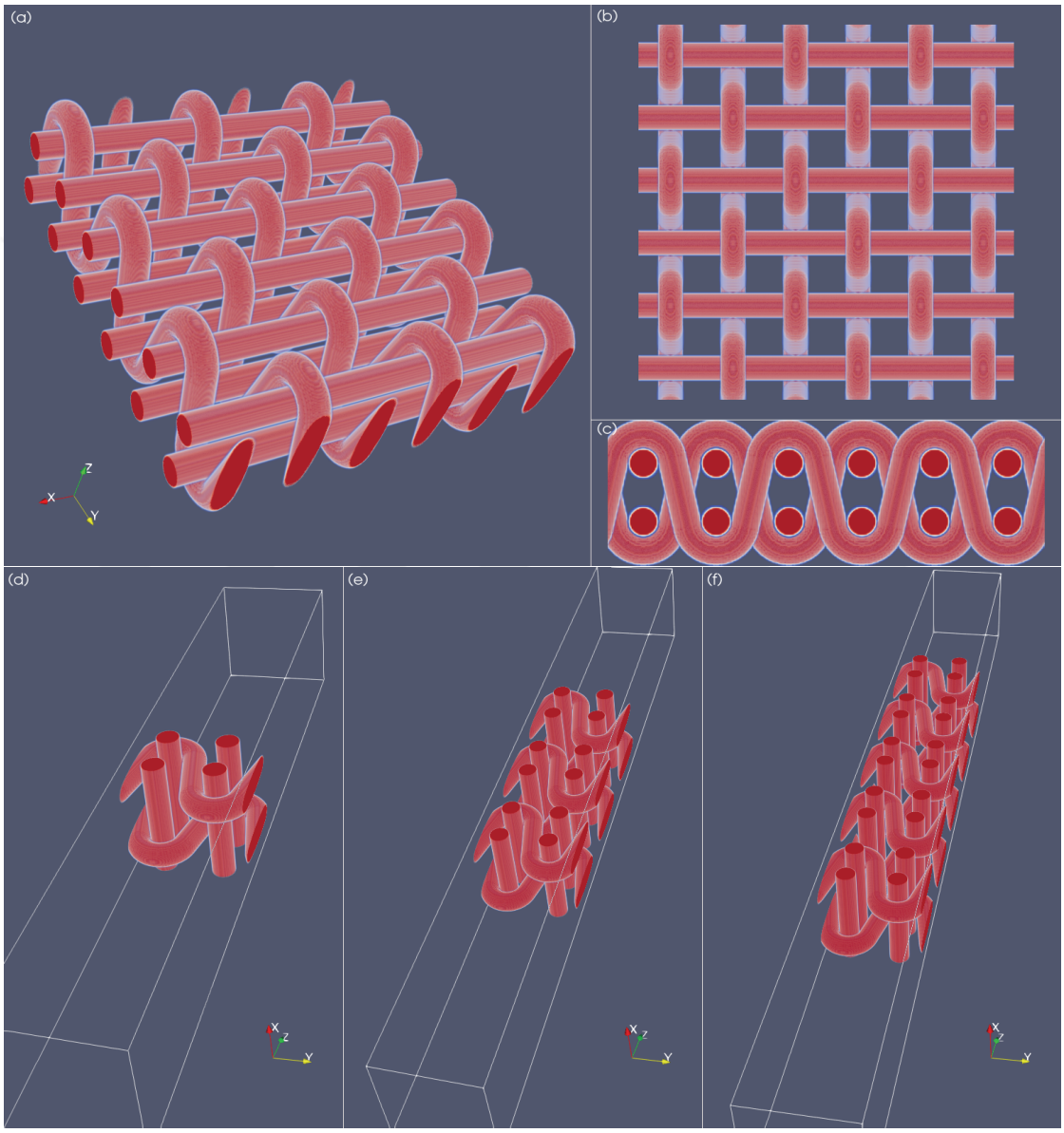


Figure 3.44. The structure of the modified dutch weave-I pattern. (a) 3D view, (b) Top view and (c) Side view. Simulation setup of the modified dutch weave-I pattern for single unit cell (d), three (e) and five (f) unit cells.

In Fig. 3.44, we have shown the FDTD simulation setup for single unit cell (d), three unit cells (e), and for five unit cells (f). In the $x - y$ direction, a single unit cell is used as usual, while three and five unit cells along $z-$direction are used for simulation. The volume of a unit cell is $V_{cell} = a_x a_y a_z$ and the volume of computational region is $V_{comp} = S_x S_y S_z$ where $S_x = S_y = a_x = a_y = a$ and $a_z = 10r$.

The transmission spectrum of this structure is shown in Fig. 3.45 for yarn radius $r = 0.06a$ and dielectric constant $\epsilon_a = 5.38$. Blue curves on the left column is the transmission spectrum, red dashed curve on the right column is the blackbody radiation spectrum and the blue curve on the right curve is the transmission spectrum for the structure which is found by multiplying transmission spectrum with blackbody radiation.

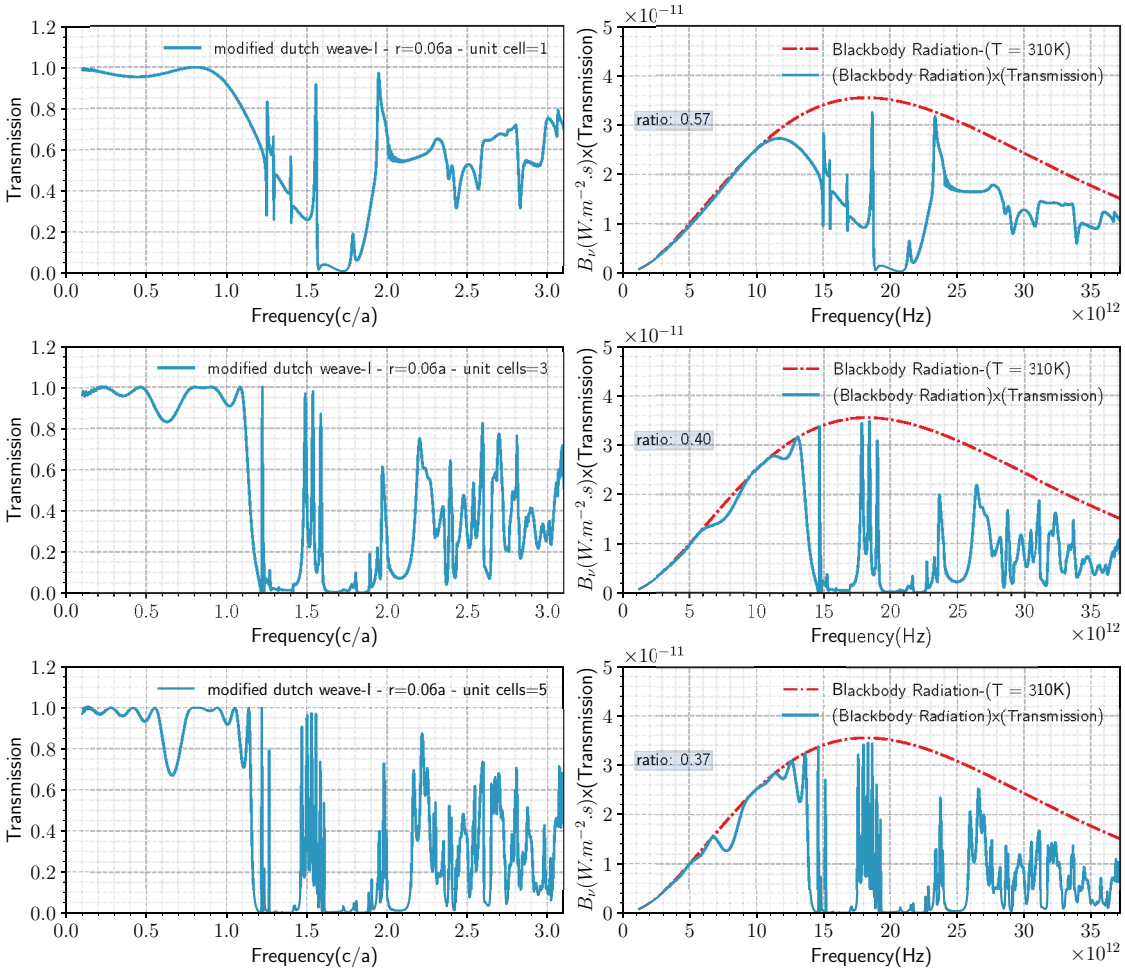


Figure 3.45. Transmission spectrum for single, three and five unit cell for modified dutch weave (left column). Blackbody radiation spectrum (right column red dashed curve). Transmission values multiplied by blackbody radiation spectrum (blue curve on the right column).

The amount of power transmitted for this structure is found to be, for single unit cell 57%, for three unit cells 40% and five unit cells 0.37%.

For the same structure with yarn radius $r = 0.08a$ calculated transmission values are shown in Fig. 3.46. Blue curves on the left column is the transmission spectrum, red dashed curve on the right column is the blackbody radiation spectrum and the blue curve on the right curve is the transmission spectrum for the structure which is found by multiplying transmission spectrum with blackbody radiation.

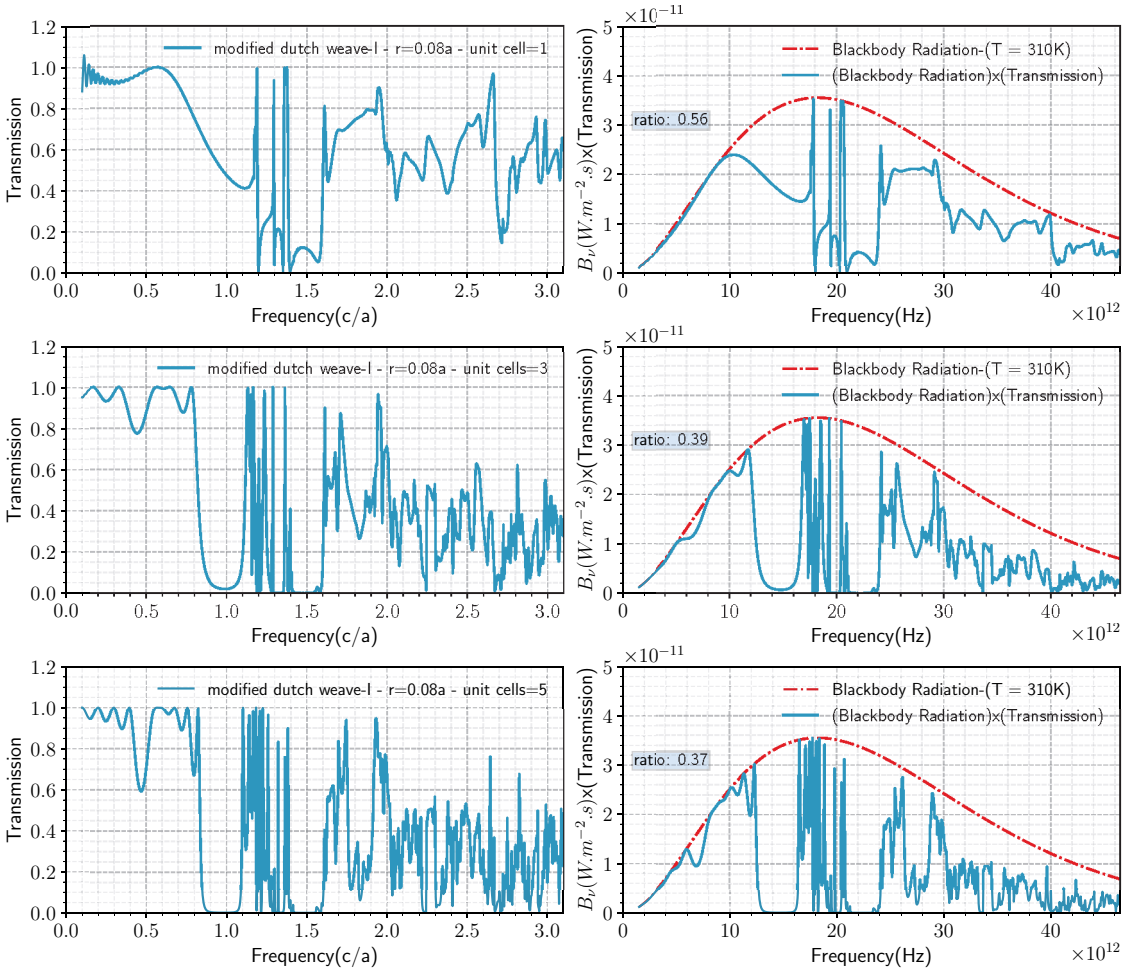


Figure 3.46. Transmission spectrum for single, three and five unit cell for modified dutch weave (left column). Blackbody radiation spectrum (right column red dashed curve). Transmission values multiplied by blackbody radiation spectrum (blue curve on the right column).

The amount of power transmitted are 56%, 39% and 37% for single, three and five unit cell.

Transmitted power percentage and corresponding yarn radius for dutch weave-I for single unit cell, three and five unit cells is shown in Table. 3.5. In this table, the first

Table 3.5. Percentage of transmitted power for modified dutch weave-I.

Radius (r)	Single unit cell (%)	Three unit cell (%)	Five unit cell (%)
$0.06a$	57	40	37
$0.07a$	56	41	38
$0.08a$	56	39	47
$0.09a$	53	37	36
$0.10a$	57	44	40
$0.11a$	61	47	45
$0.12a$	67	50	49

column is the yarn's radius, the second, third and fourth column are for single, three and five unit cell. The data shown in the Table. 3.5 are plotted for a better visualization in the

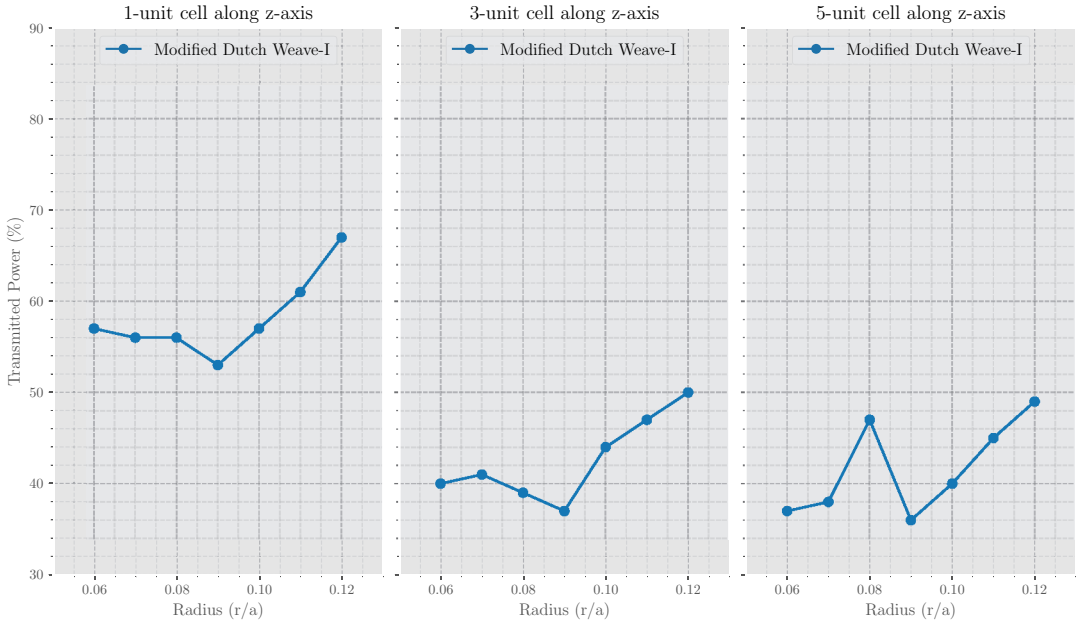


Figure 3.47. Transmitted power percentage versus yarn radius for the dutch weave-I. Single (left graph) unit cell, three (middle graph) unit cells and five (right graph) unit cells.

Fig. 3.47. The left graph is for single unit cell, the middle graph is for three unit cells and the right graph is for five unit cells along $z-$direction.

As an alternative to the previous structure, straight yarns are inserted along the $y-$direction and the resulting weave pattern is shown in Fig. 3.48 from three different viewing angles, 3D view (a), top view (b), and side view (c).

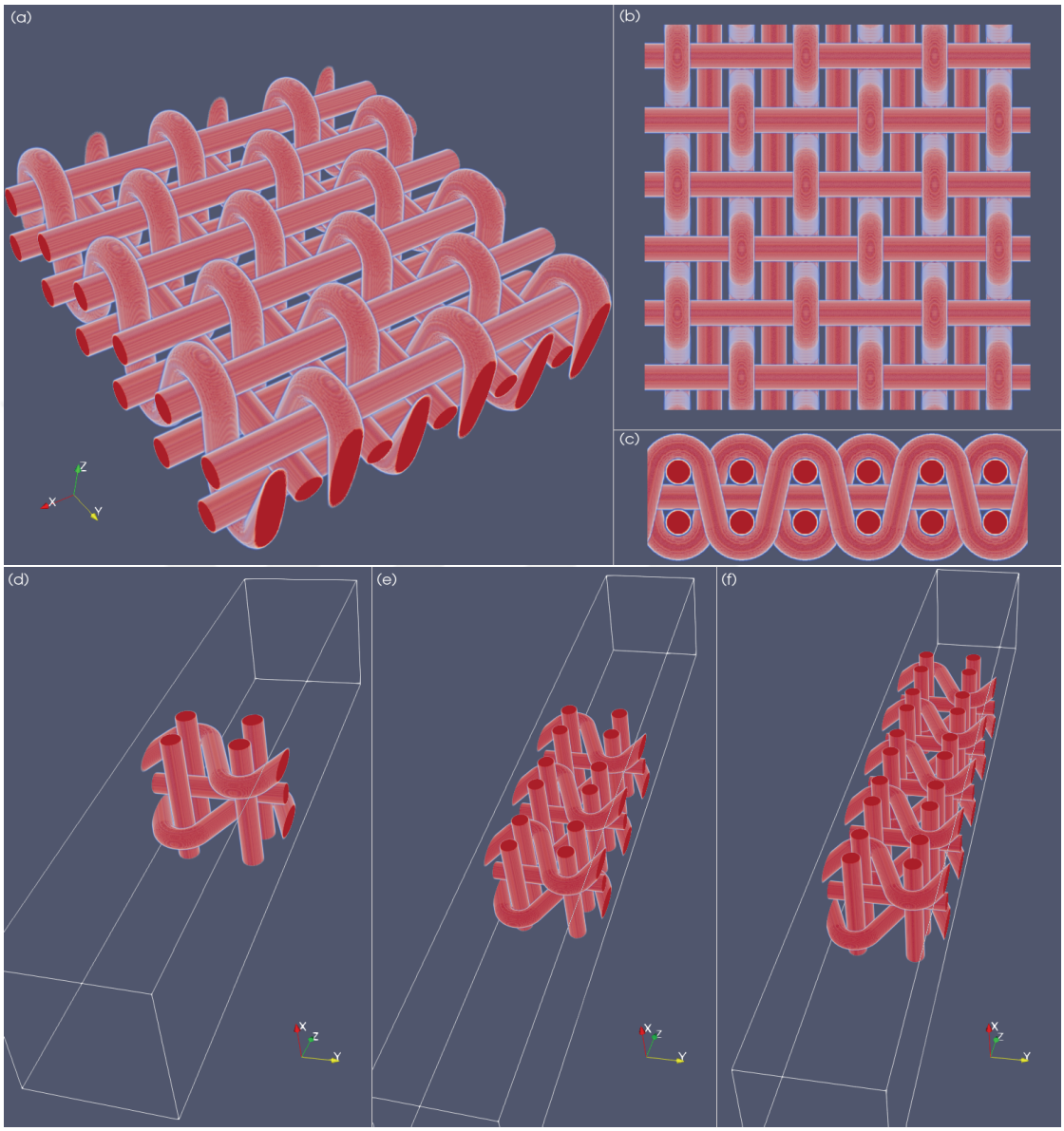


Figure 3.48. 3D view (a), top view (b) and side view (c) of modified dutch weave-II pattern. Simulation setup for modified dutch weave-II pattern for single (d), three (e) and five (f) unit cell.

The simulation setup for single (d), three (e) and five (f) unit cell along $z-$direction is shown in Fig. 3.48. PML is used in the propagation direction while in the $x-$ and $y-$directions we imposed PBC. A Gaussian profiled plane wave source with center fre-

quency $\tilde{\omega} = 1.60$ and frequency bandwidth of $\Delta\tilde{\omega} = 3.0$ is used to excite $x-$component of electric field. The volume of a unit cell is defined to be $V_{cell} = a_x a_y a_z$ where $a_x = a_y = a$ and $a_z = 10r$. The computational volume for this structure is $V_{comp} = S_x S_y S_z$ where $S_x = S_y = a_z = a_y = a$, $S_z = 2dpml + 2dpad + n_z a_z$ and n_z is the number of unit cells in along the $z-$direction. Transmission values are calculated in steps of $0.01a$ for yarn radius ranging from $r = 0.06a$ to $r = 0.12a$ with a fixed value of dielectric constant $\epsilon_a = 5.38$. The whole structure is immersed in air background.

The transmission values shown in Fig. 3.49 are for yarn radius of $r = 0.06a$. The blue curves on the left column are the transmission spectrum, the red dashed curves on the right column are the blackbody radiation spectrum, and the blue curves on the right column are the transmission spectrum for the structure, which are found by multiplying the transmission spectrum with blackbody radiation.

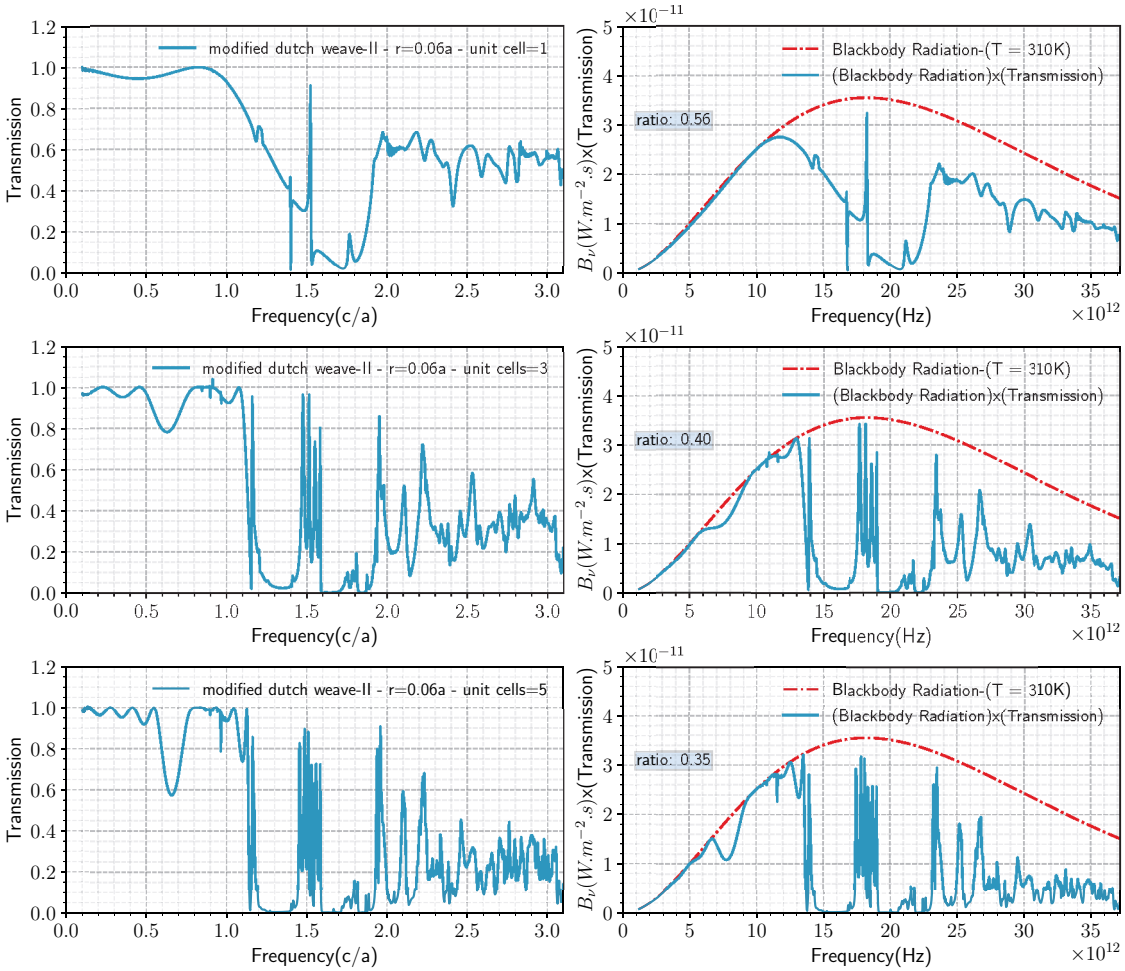


Figure 3.49. The transmission spectrum of the modified dutch weave-II for one, three, and five unit cells (left column). Blackbody radiation spectrum (red dashed curves) and transmission spectrum of the structure multiplied by blackbody radiation for one unit cell, three, and five unit cells (blue curves on the right column).

The transmitted power percentage for a single unit cell, three unit cells, and five unit cells is 56%, 40%, and 35%, respectively.

For the modified dutch weave-II structure with radius of $0.07a$, the transmission spectrum (blue curves on the left column), blackbody radiation spectrum (red dashed curve on the right column) and the transmission spectrum for the structure which is found by multiplying transmission spectrum with blackbody radiation (blue curve on the right column) is shown in Fig. 3.50.

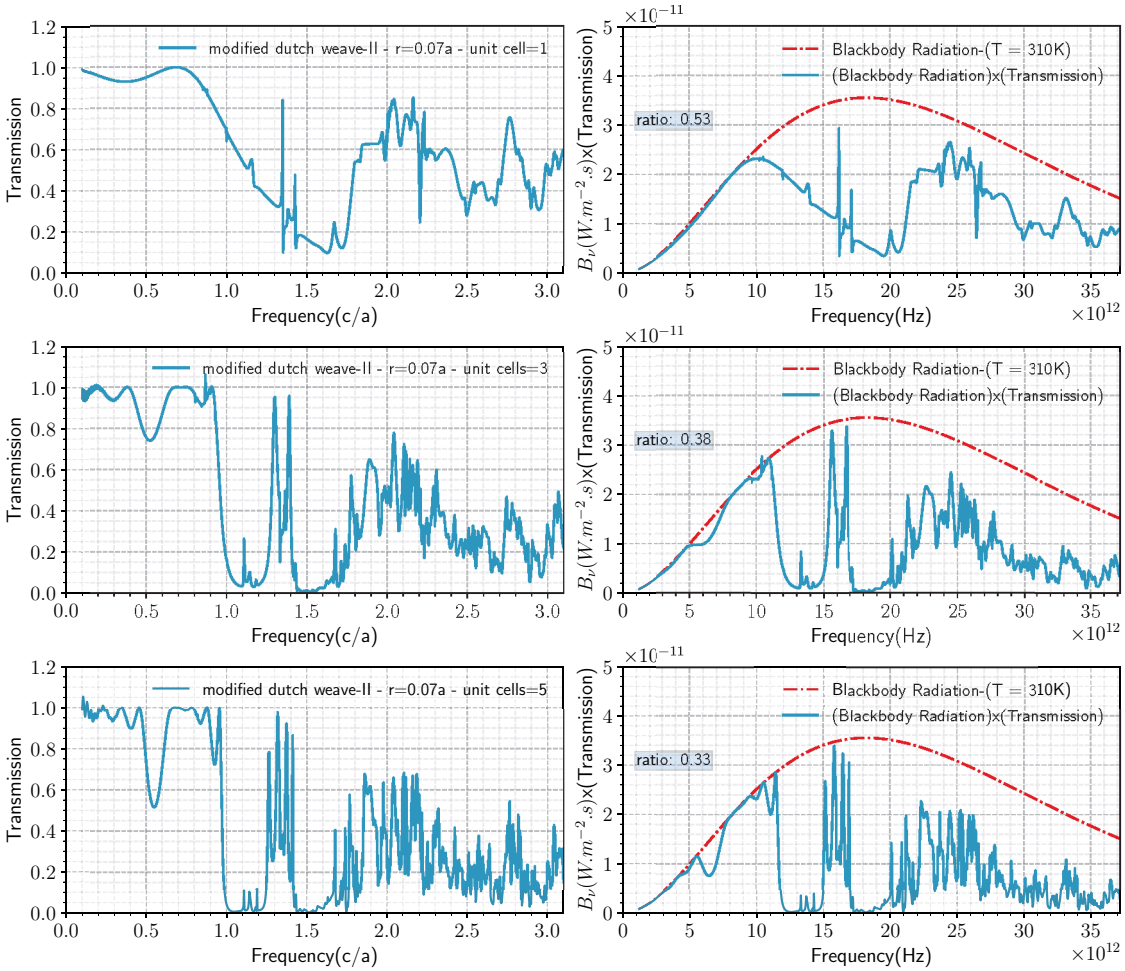


Figure 3.50. The transmission spectrum of the modified dutch weave pattern for one unit cell, three, and five unit cells (left column). Blackbody radiation spectrum (red dashed curve) and transmission spectrum of the structure multiplied by blackbody radiation for one unit cell, three, and five unit cells (blue curves on the right column).

For this structure, the percentage of transmitted power are 53%, 38% and 33% for single, three and five unit cell.

Transmission results for modified dutch weave-II with yarn radius of $r = 0.08a$ is shown in Fig. 3.51. The blue curves on the left column are the transmission spectrum, the red dashed curve on the right column is the blackbody radiation spectrum, and the blue curves on the right column are the transmission spectrum for the structure, which is found by multiplying the transmission spectrum with blackbody radiation.

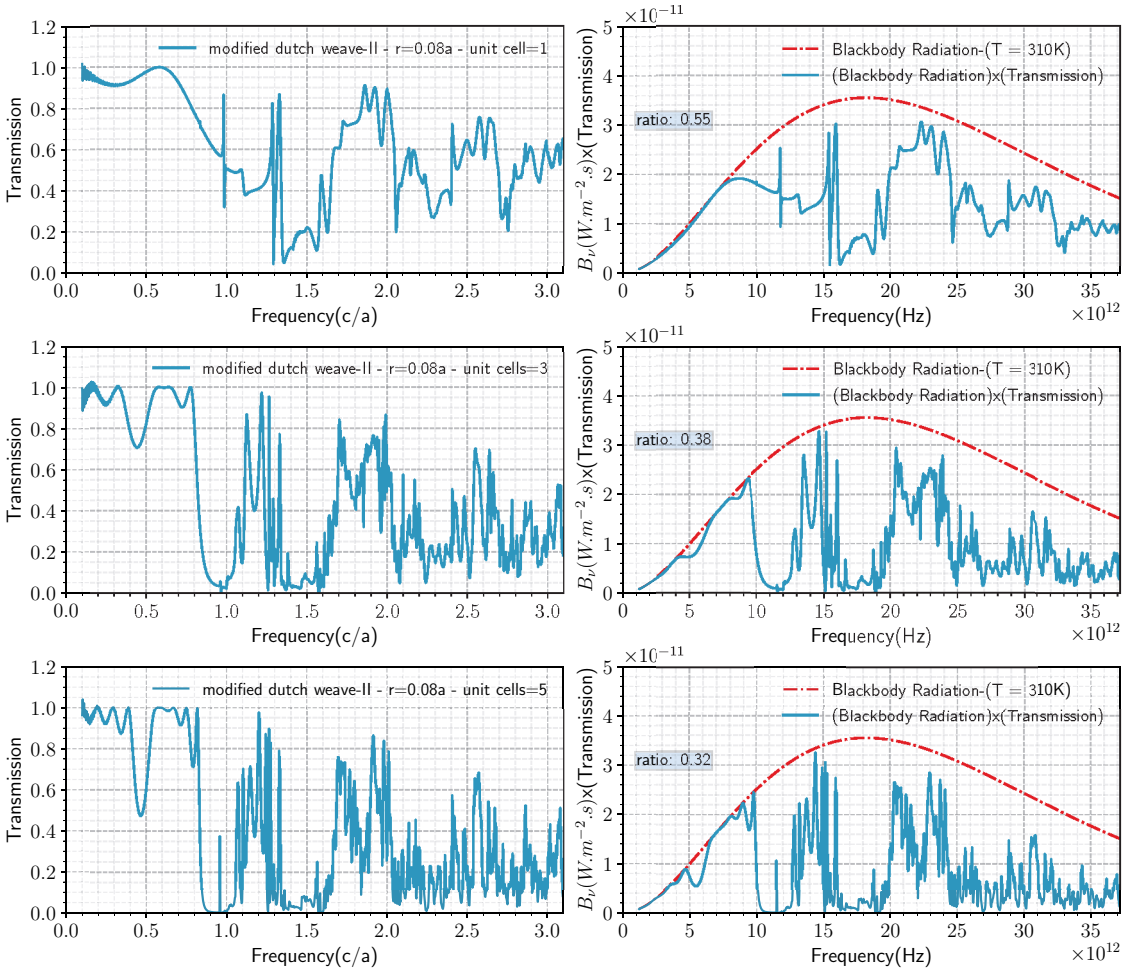


Figure 3.51. The transmission spectrum of modified dutch weave-II for one unit cell, three, and five unit cells (left column). Blackbody radiation spectrum (red dashed curve) and the transmission spectrum of the structure multiplied by blackbody radiation for one unit cell, three, and five unit cells (blue curves on the right column).

The amount of power transmitted by this structure is found to be 55% for a single unit cell, 38% for three unit cells, and 32% for five unit cells.

Table. 3.6 shows the transmitted power percentage and corresponding yarn radius for dutch weave-II for a single unit cell, three and five unit cells are shown. As the num-

Table 3.6. Percentage of transmitted power for modified dutch weave-II.

Radius (r)	Single unit cell (%)	Three unit cell (%)	Five unit cell (%)
$0.06a$	56	40	35
$0.07a$	53	38	33
$0.08a$	55	38	32
$0.09a$	58	40	36
$0.10a$	64	47	43
$0.11a$	68	51	46
$0.12a$	71	55	50

ber of the unit cell along the stacking direction increases the transmitted power percentage decreases as expected. But the dependence on the number of a unit cell is weak. Minimum transmission obtained for yarn radius of $0.06a$, $0.07a$ and $0.08a$. The Fig. 3.52 are

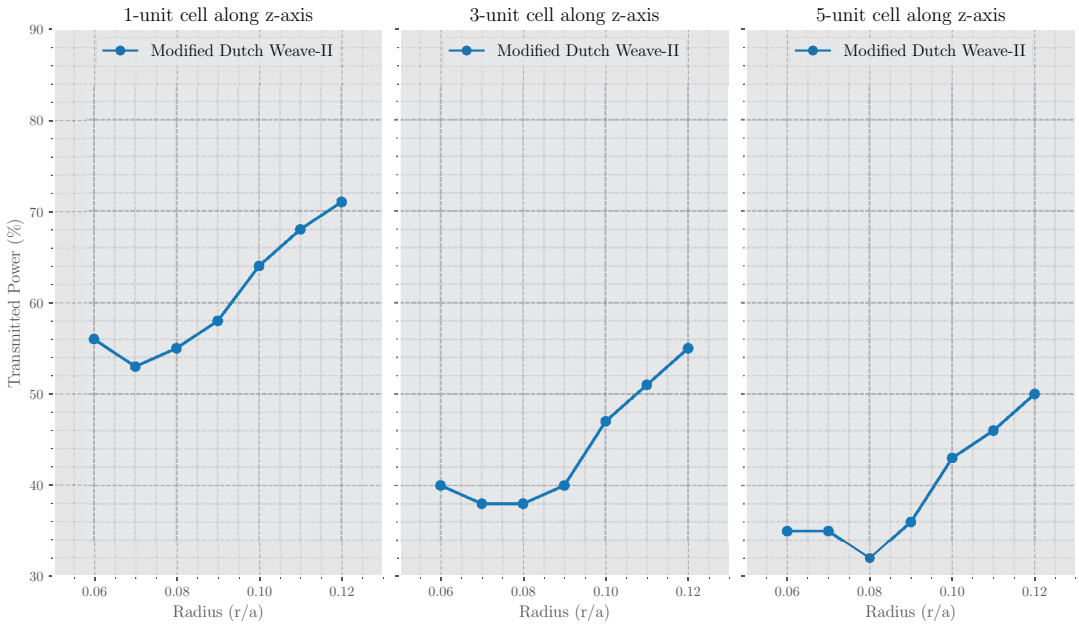


Figure 3.52. Transmitted power percentage versus yarn radius for the modified dutch weave-II. Single (left graph) unit cell, three (middle graph) unit cells, and five (right graph) unit cells.

plotted using data given in the Table. 3.6. The left graph represents the transmitted power percentage for a single unit cell, while the middle is for three unit cells and the right graph is for five unit cells.

To see the dependence of transmitted power percentage on weaving pattern and yarn radius, we plotted all results on the same graph. The amount of transmitted power relationship between weave patterns (plain weave, modified plain weave, dutch weave, modified dutch weave-I, and modified dutch weave-II) and yarn radius for single unit cell, three unit cells, and five unit cells is shown in Fig. 3.53. Among all the weave patterns we

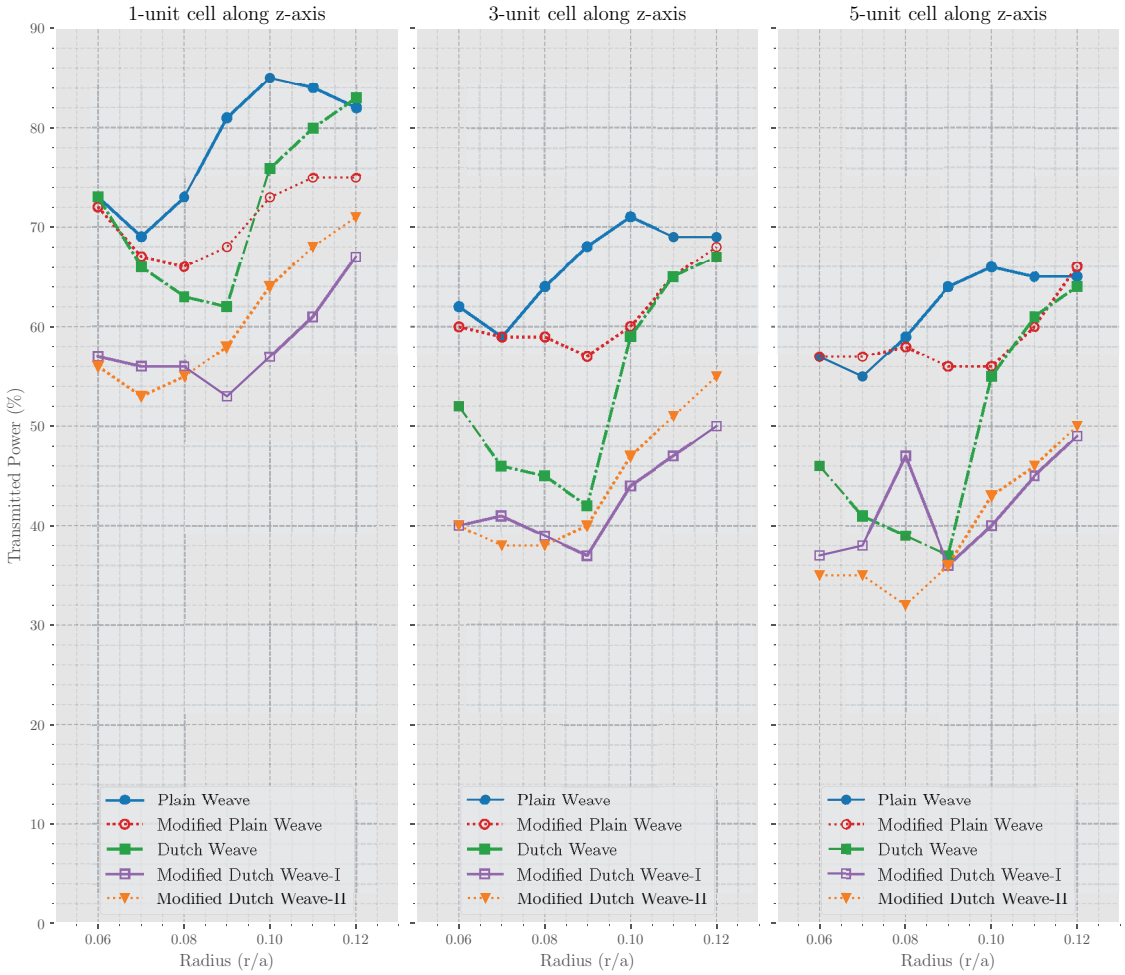


Figure 3.53. Percentage of transmitted power versus yarn radius for five different weave patterns. Plain weave, modified plain weave, dutch weave, modified dutch weave-I, and modified dutch weave-II for single unit cell (left graph), three unit cells (middle graph), and five unit cells (right graph).

have studied, calculations have shown that the modified dutch pattern gives the minimum transmission.

CHAPTER 4

CONCLUSION AND FUTURE WORK

4.1. Conclusion

In this thesis, we addressed the problem of heat loss from the human body. Under normal conditions, the amount of heat lost through electromagnetic radiation from the human body skin accounts for about two-thirds of the total energy produced by the human body. So suppressing this energy can save a substantial amount of power used to heat the human body's environment. The main contribution of our work is to use photonic crystals' (PhCs) ability to confine electromagnetic radiation to produce woven textiles which can be considered as a thin layer of electromagnetic shield.

Starting from 1D-PhCs, we have shown that even with these simple structures, it is possible to reduce heat loss. To improve the structure's performance, we used a more complicated 3D-PhCs structure known as a woodpile with a complete photonic band gap (PBG). Since the full PBG is only possible for crystals that have an infinite extent, the calculated transmission results, of course, would be different than the expected ones.

Showing that electromagnetic radiation can be suppressed using those structures, we then worked with the most common weave pattern used in the textile industry: the plain weave, the basket weave, the dutch weave, and the twill weave patterns. The degrees of freedom of the problem are those that would affect the PBG. Those are the dielectric constant, the thickness of the yarn, and the weaving pattern. In our work, we used real-symmetric and frequency-independent dielectric constants. Which leaves out the dependence on the polarization of the electromagnetic field of the material. Then we used a moderate frequency independent dielectric constant so that we could create a contrast between the material and the background. Leaving those aside, we are left with two degrees of freedom, namely the radius of the yarns and the weave pattern.

To find the best weave pattern and optimum yarn radius, we used the finite-difference time-domain method (FDTD) by brute force calculations and sweeping over

the radius of yarn for all those weaving patterns we defined. Throughout our work, we also modified each weave pattern so that its structure would be close to the woodpile PhC, which is known for having full PBG. Among all those four weaving patterns, five more patterns that are created by modification, we have found that the modified dutch weave gave the optimum results.

Even though we mainly aimed to find the optimum woven structure that maximizes the reflection of radiation from an object at $37°$C, the same approach, in principle, can be used to find structures that reflect radiation emitted by objects at higher temperatures, such as those that firefighters might be exposed to. In principle, this method can be scaled to any regime of the electromagnetic spectrum, except for the regimes that have very high energy and might destroy the molecular structure of material.

4.2. Future Work

Since the structures are 3-dimensional, the numerical method we used demands a huge amount of computational power, storing capacity, and time. The FDTD method divides space and time into grids and then lets Maxwell's equation evolve over time in a finite volume. So, even for low resolution calculations, it requires a huge amount of time and computational power as well as storage capacity. So, using a different algorithm such as the Finite element method (FEM), which requires less memory since FEM discretizes the computational space non-uniformly, would be more effective. The following properties are left as future work due to time limitations.

The dielectric material used in calculations is assumed to be isotropic, which means that the material threat electromagnetic radiation is the same in all directions. But most of the materials used in the textile industry are anisotropic. It would give more information about optimizing the best material.

Again, as a material property, we used real dielectric constant, which means no gain or loss occurs. Introducing a complex dielectric constant would give more accurate results.

The source we used in our calculation is a Gaussian-profiled plane wave spanning $2-$dimension. To get more realistic results, we need to represent the blackbody radiation spectrum by using randomly oriented dipoles that would radiate in all directions.

We also disregarded the absorption due to radiation from the environment. Thus our results are valid for extremely cold environments. Taking the absorption from environment into account would enable optimal design for different environmental conditions, such as out in the sun, or at home or at moderate cold temperature around $0°C$.

Furthermore, the bandgap can be fine tuned so that the absorption from the environment can be made less than the radiation to the environment for a cooling effect.

REFERENCES

Assaf, S., M. Boutghatin, Y. Pennec, V. Thomy, A. Korovin, A. Treizebre, M. Carette, A. Akjouj, et al. (2020). Polymer photonic crystal membrane for thermo-regulating textile. *Scientific reports 10*(1), 1–9.

Cai, L., Y. Peng, J. Xu, C. Zhou, C. Zhou, P. Wu, D. Lin, S. Fan, and Y. Cui (2019). Temperature regulation in colored infrared-transparent polyethylene textiles. *Joule 3*(6), 1478–1486.

Cai, L., A. Y. Song, P. Wu, P.-C. Hsu, Y. Peng, J. Chen, C. Liu, P. B. Catrysse, Y. Liu, A. Yang, et al. (2017). Warming up human body by nanoporous metallized polyethylene textile. *Nature communications 8*(1), 1–8.

Catrysse, P. B., A. Y. Song, and S. Fan (2016). Photonic structure textile design for localized thermal cooling based on a fiber blending scheme. *ACS Photonics 3*(12), 2420–2426.

Chen, M., D. Pang, J. Mandal, X. Chen, H. Yan, Y. He, N. Yu, and Y. Yang (2021). Designing mesoporous photonic structures for high-performance passive daytime radiative cooling. *Nano Letters 21*(3), 1412–1418.

Cornelius, C. M. and J. P. Dowling (1999). Modification of planck blackbody radiation by photonic band-gap structures. *Physical Review A 59*(6), 4736.

Furukawa, M., H. Sato, and Y. Watanabe (2012). Fabrication of tio2 coated cotton-yarn as high-dielectric-constant fiber for 3-d photonic crystal application. *Transactions of the Materials Research Society of Japan 37*(1), 35–38.

Gao, T., Z. Yang, C. Chen, Y. Li, K. Fu, J. Dai, E. M. Hitz, H. Xie, B. Liu, J. Song, et al. (2017). Three-dimensional printed thermal regulation textiles. *ACS nano 11*(11), 11513–11520.

Gu, B., H. Zhou, Z. Zhang, T. Zhang, M. Chen, F. Qiu, and D. Yang (2021). Cellulose-based hybrid membrane with functional integration for personal thermal management applications. *Applied Surface Science 535*, 147670.

Guo, Z., C. Sun, J. Wang, Z. Cai, and F. Ge (2021). High-performance laminated fabric

with enhanced photothermal conversion and joule heating effect for personal thermal management. *ACS Applied Materials & Interfaces 13*(7), 8851–8862.

Hardy, J. D. et al. (1934a). The radiation of heat from the human body: I. an instrument for measuring the radiation and surface temperature of the skin. *The Journal of clinical investigation 13*(4), 593–604.

Hardy, J. D. et al. (1934b). The radiation of heat from the human body: Ii. a comparison of some methods of measurement. *The Journal of Clinical Investigation 13*(4), 605–614.

Hardy, J. D. et al. (1934c). The radiation of heat from the human body: Iii. the human skin as a black-body radiator. *The Journal of clinical investigation 13*(4), 615–620.

Hardy, J. D. and E. F. DuBois (1937). Regulation of heat loss from the human body. *Proceedings of the National Academy of Sciences of the United States of America 23*(12), 624.

Hardy, J. D., C. Muschenheim, et al. (1934). The radiation of heat from the human body. iv. the emission, reflection, and transmission of infra-red radiation by the human skin. *The Journal of clinical investigation 13*(5), 817–831.

Ho, K., C. T. Chan, and C. M. Soukoulis (1990). Existence of a photonic gap in periodic dielectric structures. *Physical Review Letters 65*(25), 3152.

Ho, K. M., C. T. Chan, C. M. Soukoulis, R. Biswas, and M. Sigalas (1994). Photonic band gaps in three dimensions: New layer-by-layer periodic structures. *Solid state communications 89*(5), 413–416.

Hsu, P.-C., C. Liu, A. Y. Song, Z. Zhang, Y. Peng, J. Xie, K. Liu, C.-L. Wu, P. B. Catrysse, L. Cai, et al. (2017). A dual-mode textile for human body radiative heating and cooling. *Science advances 3*(11), e1700895.

Hsu, P.-C., X. Liu, C. Liu, X. Xie, H. R. Lee, A. J. Welch, T. Zhao, and Y. Cui (2015). Personal thermal management by metallic nanowire-coated textile. *Nano Letters 15*(1), 365–371. PMID: 25434959.

Hsu, P.-C., A. Y. Song, P. B. Catrysse, C. Liu, Y. Peng, J. Xie, S. Fan, and Y. Cui (2016). Radiative human body cooling by nanoporous polyethylene textile.

Science 353(6303), 1019–1023.

Jafar-Zanjani, S., M. M. Salary, and H. Mosallaei (2017). Metafabrics for thermoregulation and energy-harvesting applications. *ACS Photonics 4*(4), 915–927.

Jeong, S.-M., J. Ahn, Y. K. Choi, T. Lim, K. Seo, T. Hong, G. H. Choi, H. Kim, B. W. Lee, S. Y. Park, et al. (2020). Development of a wearable infrared shield based on a polyurethane–antimony tin oxide composite fiber. *NPG Asia Materials 12*(1), 1–13.

Joannopoulos, J. D., S. G. Johnson, J. N. Winn, and R. D. Meade (2008). Molding the flow of light. *Princeton Univ. Press, Princeton, NJ [ua]*.

John, S. (1987). Strong localization of photons in certain disordered dielectric superlattices. *Physical review letters 58*(23), 2486.

Johnson, S. G. and J. Joannopoulos (2000). Three-dimensionally periodic dielectric layered structure with omnidirectional photonic band gap. *Applied Physics Letters 77*(22), 3490–3492.

L. Chern, R., C. Chung Chang, C. C. Chang, and R. R. Hwang (2004). Numerical study of three-dimensional photonic crystals with large band gaps. *Journal of the Physical Society of Japan 73*(3), 727–737.

Leung, E. M., M. Colorado Escobar, G. T. Stiubianu, S. R. Jim, A. L. Vyatskikh, Z. Feng, N. Garner, P. Patel, K. L. Naughton, M. Follador, et al. (2019). A dynamic thermoregulatory material inspired by squid skin. *Nature communications 10*(1), 1–10.

Li, D., X. Liu, W. Li, Z. Lin, B. Zhu, Z. Li, J. Li, B. Li, S. Fan, J. Xie, et al. (2021). Scalable and hierarchically designed polymer film as a selective thermal emitter for high-performance all-day radiative cooling. *Nature Nanotechnology 16*(2), 153–158.

Lin, S.-y., J. Fleming, D. Hetherington, B. Smith, R. Biswas, K. Ho, M. Sigalas, W. Zubrzycki, S. Kurtz, and J. Bur (1998). A three-dimensional photonic crystal operating at infrared wavelengths. *Nature 394*(6690), 251–253.

Luo, H., Y. Zhu, Z. Xu, Y. Hong, P. Ghosh, S. Kaur, M. Wu, C. Yang, M. Qiu, and Q. Li (2021). Outdoor personal thermal management with simultaneous electricity generation. *Nano letters 21*(9), 3879–3886.

Oskooi, A. F., D. Roundy, M. Ibanescu, P. Bermel, J. D. Joannopoulos, and S. G. Johnson (2010). Meep: A flexible free-software package for electromagnetic simulations by the fdtd method. *Computer Physics Communications 181*(3), 687–702.

Özbay, E. (1996). Layer-by-layer photonic crystals from microwave to far-infrared frequencies. *JOSA B 13*(9), 1945–1955.

Özbay, E., A. Abeyta, G. Tuttle, M. Tringides, R. Biswas, C. T. Chan, C. M. Soukoulis, and K. Ho (1994). Measurement of a three-dimensional photonic band gap in a crystal structure made of dielectric rods. *Physical Review B 50*(3), 1945.

Planck, M. (2013). *The Theory of Heat Radiation*. CreateSpace Independent Publishing Platform.

Sanchez-Marin, F. J., S. Calixto-Carrera, and C. Villaseñor-Mora (2009). Novel approach to assess the emissivity of the human skin. *Journal of Biomedical Optics 14*(2), 024006.

Shi, M., M. Shen, X. Guo, X. Jin, Y. Cao, Y. Yang, W. Wang, and J. Wang (2021). Ti3c2tx mxene-decorated nanoporous polyethylene textile for passive and active personal precision heating. *ACS nano 15*(7), 11396–11405.

Shklover, V., L. Braginsky, M. Mishrikey, and C. Hafner (2009). High-temperature fiber matrix composites for reduction of radiation heat transfer. *MRS Online Proceedings Library 1162*(1), 1–6.

Song, Y.-N., Y. Li, D.-X. Yan, J. Lei, and Z.-M. Li (2020). Novel passive cooling composite textile for both outdoor and indoor personal thermal management. *Composites Part A: Applied Science and Manufacturing 130*, 105738.

Sözüer, H. and J. P. Dowling (1994). Photonic band calculations for woodpile structures. *Journal of Modern Optics 41*(2), 231–239.

Sözüer, H. S., J. Haus, and R. Inguva (1992). Photonic bands: Convergence problems with the plane-wave method. *Physical Review B 45*(24), 13962.

Steketee, J. (1973). Spectral emissivity of skin and pericardium. *Physics in Medicine & Biology 18*(5), 686.

Taflove, A., S. C. Hagness, and M. Piket-May (2005). Computational electromagnetics: the finite-difference time-domain method. *The Electrical Engineering Handbook 3*, 629–670.

Tao, Y., T. Li, C. Yang, N. Wang, F. Yan, and L. Li (2018). The influence of fiber cross-section on fabric far-infrared properties. *Polymers 10*(10), 1147.

Toader, O. and S. John (2001). Proposed square spiral microfabrication architecture for large three-dimensional photonic band gap crystals. *Science 292*(5519), 1133–1135.

Tong, J. K., X. Huang, S. V. Boriskina, J. Loomis, Y. Xu, and G. Chen (2015). Infrared-transparent visible-opaque fabrics for wearable personal thermal management. *ACS Photonics 2*(6), 769–778.

Tsai, Y.-C., J. B. Pendry, and K. W.-K. Shung (1999). Absolute three-dimensional photonic band gap in the infrared regime in woven structures. *Physical Review B 59*(16), R10401.

Tsai, Y.-C., K. W. Shung, and J. B. Pendry (1998). Three-dimensional photonic band gaps in woven structures. *Journal of Physics: Condensed Matter 10*(4), 753.

Vlasov, Y. A., X.-Z. Bo, J. C. Sturm, and D. J. Norris (2001). On-chip natural assembly of silicon photonic bandgap crystals. *Nature 414*(6861), 289–293.

Wang, Z., H. Yang, Y. Li, and X. Zheng (2020). Robust silk fibroin/graphene oxide aerogel fiber for radiative heating textiles. *ACS Applied Materials & Interfaces 12*(13), 15726–15736.

Watanabe, Y., T. Hotta, and H. Sato (2010). Fabrication of flexible photonic crystal using alumina ball inserted teflon tube. *Applied Physics A 100*(4), 981–985.

Watanabe, Y., T. Kobayashi, S. Kirihara, Y. Miyamoto, and K. Sakoda (2004). Cotton-yarn/tio2 dispersed resin photonic crystals with straight and wavy structures. *The European Physical Journal B-Condensed Matter and Complex Systems 39*(3), 295–300.

Winslow, C.-E., A. Gagge, and L. Herrington (1939). The influence of air movement upon heat losses from the clothed human body. *American Journal of Physiology-Legacy Content 127*(3), 505–518.

Xiang, B., R. Zhang, X. Zeng, Y. Luo, and Z. Luo (2022). An easy-to-prepare flexible dual-mode fiber membrane for daytime outdoor thermal management. *Advanced Fiber Materials*, 1–11.

Xiao, R., C. Hou, W. Yang, Y. Su, Y. Li, Q. Zhang, P. Gao, and H. Wang (2019). Infrared-radiation-enhanced nanofiber membrane for sky radiative cooling of the human body. *ACS Applied Materials & Interfaces 11*(47), 44673–44681.

Yablonovitch, E. (1987). Inhibited spontaneous emission in solid-state physics and electronics. *Physical review letters 58*(20), 2059.

Yablonovitch, E. and T. Gmitter (1989). Photonic band structure: The face-centered-cubic case. *Physical Review Letters 63*(18), 1950.

Yablonovitch, E., T. Gmitter, and K.-M. Leung (1991). Photonic band structure: The face-centered-cubic case employing nonspherical atoms. *Physical review letters 67*(17), 2295.

Yang, Z. and J. Zhang (2021). Bioinspired radiative cooling structure with randomly stacked fibers for efficient all-day passive cooling. *ACS Applied Materials & Interfaces 13*(36), 43387–43395.

Yee, K. (1966). Numerical solution of initial boundary value problems involving maxwell's equations in isotropic media. *IEEE Transactions on antennas and propagation 14*(3), 302–307.

Yu, H., X. Yang, Y. Lian, M. Wang, Y. Liu, Z. Li, Y. Jiang, and J. Gou (2021). An integrated flexible multifunctional wearable electronic device for personal health monitoring and thermal management. *Sensors and Actuators A: Physical 318*, 112514.

Zhou, K., W. Li, B. B. Patel, R. Tao, Y. Chang, S. Fan, Y. Diao, and L. Cai (2021). Three-dimensional printable nanoporous polymer matrix composites for daytime radiative cooling. *Nano letters 21*(3), 1493–1499.

VITA

EDUCATION

2022 Doctor of Philosophy (Ph.D.) in Physics

Graduate School of Engineering and Sciences, İzmir Institute of Technology,
İzmir -Turkey
Thesis Title: Photonic Crystal Textiles
Supervisor: Assoc. Prof. Dr. H. Sami SÖZÜER

2013 Master of Science (M.Sc.) in Physics

Graduate School of Engineering and Sciences, İzmir Institute of Technology
İzmir -Turkey
Thesis Title: Improving Coupling Efficiency by Using Adiabatic Transition in Photonic Crystal Waveguides
Supervisor: Assoc. Prof. Dr. H. Sami SÖZÜER

2008 Bachelor of Science (B.Sc.) in Physics

Department of Physics, Faculty of Science, İzmir Institute of Technology
İzmir - Turkey

PUBLICATIONS

Ates, B., A. Kustepeli, and Z. Cetin (2021). Analytical improvement on the electromagnetic scattering from deformed spherical conducting objects. *IEEE Transactions on Antennas and Propagation 69*(12), 8630–8640.

Eti, N., Z. Çetin, and H. S. Sözüer (2018). Fully three-dimensional analysis of a photonic crystal assisted silicon on insulator waveguide bend. *International Journal of Modern Physics B 32*(31), 1850344.

SCHOLARSHIPS

2018-2022 YÖK 100/2000 Ph.D. Scholarship.